RICE UNIVERSITY

Modeling the Earth's Magnetosphere using Magnetohydrodynamics

by

Bei Hu

A THESIS SUBMITTED
IN PARTIAL FULFILLMENT OF THE
REQUIREMENTS FOR THE DEGREE

Doctor of Philosophy

APPROVED, THESIS COMMITTEE:

F. Toffoletto

Frank R. Toffoletto, Professor
Physics and Astronomy Department
Chair of Thesis Committee

Richard A. Wolf

Richard A. Wolf, Professor Emeritus
Physics and Astronomy Department

A. J. Meade

Andrew J. Meade, Professor
Department Chair of Mechanical
Engineering and Materials Science

HOUSTON, TEXAS
December, 2011

ABSTRACT

Modeling the Earth's Magnetosphere using Magnetohydrodynamics

by

Bei Hu

This thesis describes work on building numerical models of the Earth's magnetosphere using magnetohydrodynamics (MHD) and other related modeling methods. For many years, models that solve the MHD equations have been the main tool for improving our theoretical understanding of the large-scale dynamics of the Earth's magnetosphere. While the MHD models have been very successful in capturing many large-scale features, they fail to adequately represent the important drift physics in the inner magnetosphere. Consequently, the ring current, which contains most of the particle energy in the inner magnetosphere, is not realistically represented in MHD models. In this thesis, Chapter 2 and 3 will describe in detail our effort to couple the OpenGGCM (Open Geospace General Circulation Model), one of the major MHD models, to the Rice Convection Model (RCM), an inner magnetosphere ring current model, with the goal of including energy dependent drift physics into the MHD model. In Chapter 4, we will describe an initial attempt to use a direct-integration method to calculate Birkeland currents in the MHD code. Another focus of the thesis work, presented in Chapter 5, addresses a longstanding problem on how a geomagnetic substorm can occur within the closed field line region of the tail. We find a scenario of a bubble-blob pair formation in an OpenGGCM simulation just before the expansion phase of the substorm begins and the subsequent separation of the bubble and the blob decreases the normal component of the magnetic field until finally an X-line occurs. Thus the formation of the bubble-blob pair may play an important role in changing the magnetospheric configuration from a stretched field to the X-line formation that is believed to be the major signature of a substorm.

Acknowledgements

During my past five and a half years at Rice, I have become forever indebted to my advisor Dr. Frank Toffoletto and I want to express my deepest and heartfelt thanks to him for his guidance in research and being a life mentor as an example of a disciplined and respectful gentleman. He never blamed me for not knowing a specific knowledge but would rather point me to the right resource to help me learn. He never became angry when my codes didn't do what they supposed to do but always expressed encouragement and positive interests to ease my frustration. He always shows understanding and patience when I had problems or made mistakes. Without his invaluable advices and experiences, along with his encouragement and unlimited tolerance, I wouldn't have enjoyed so much for being a computational modeler and a student at Rice.

I owe much gratitude to Dr. Richard Wolf for his advice and help on my thesis work, which benefits a lot from his creative ideas and unbelievable vast knowledge in space physics. This thesis also could not be accomplished without the support and guidance from Dr. Jimmy Raeder and I am particularly grateful to him. I am also grateful to Dr. Stan Sazykin, Dr. Tom Hill, Dr. Anthony Chan and Dr. Bob Spiro for their help and suggestions. My appreciation also goes to Doug Larson, Kai Germaschewski and Bonnie Hausman for their help in research. I'd like to thank Dr. Andrew Meade and Dr. Wolf again for serving in my thesis committee.

I received a lot of help from my colleagues/classmates and gained happiness for being with them. Liang Wu, Jian Yang, Liheng Zheng, Asher Pembroke, Yi Chen, Xin Liu, Xuhui Chen, Yaxue Dong, Yifei Wan and Chunmin Zhu at Rice, and Alex Vapirev, Wenhui Li, Hyun Ju and Yasong Ge at University of New Hampshire, thank you all. I also thank all others who helped me during my study at Rice and I apologize if I missed your name.

Finally, I would like to thank my wife Hong Liang as I honestly cannot think of me going through the past years without her love, encouragement and unconditional support. I also thank my parents for being so supportive while I am so far away from home.

Table of Contents

List of Figures

Chapter 1

Introduction

1.1 Introduction to the Earth's magnetosphere

Looking up at night, we can see stars in the sky that are several to hundreds of light years away. Between the stars and us, the space surrounding our planet Earth seems to be an empty vacuum and seemingly contains nothing interesting. In fact, the vacuum in space has fewer particles (number density ~10^5 to 10^7 particles per m^3) than some of the best laboratory vacuums on Earth [*Kivelson*, 1995] but the physics of the dynamic processes happening in this region is quite important and interesting.

The Earth is in fact surrounded by charged particles and a magnetic structure that is shaped by the Earth's internal magnetic field (produced by dynamo currents flowing inside) and its interaction with the solar wind and the interplanetary magnetic field (IMF). The solar wind consists of charged particles that escape from the upper atmosphere of the Sun and is supersonic [*Parker*, 1958] and superalfvenic when it reaches the Earth. The plasma in the solar wind is considered a perfect conductor and the particles are frozen (tied) into the interplanetary magnetic field. Since the Earth is and its internal field serves as an obstacle against the supersonic solar wind, a shock (Bow shock) is formed between the Earth's dipole-like magnetic field and the solar wind. The supersonic solar wind slows down and flows around a cavity called the Magnetosphere, which is dominated by the Earth's internal field.

The internal structure of the magnetosphere is complicated and heavily dependent on the solar wind and IMF conditions since essentially nearly all the energy in the system is from the Sun; in fact, the magnetosphere is strongly coupled to the solar wind/IMF and the goal of the solar-terrestrial research is to understand how events that happen on the Sun ultimately impact the Earth's magnetosphere. Our particular emphasis will be on understanding how the magnetosphere responds to different solar wind and IMF conditions.

Figure 1.1 is an illustration showing the basic structure of the Earth's magnetosphere. This is only in an average sense as these structures are quite different in reality. On the dayside, the solar wind and IMF confine the Earth's field into a relatively small region called the dayside magnetosphere. On the nightside, the Earth's field extends to distant region downstream of the solar wind, forming the magnetotail (or tail). There are several important regions related to my thesis work that I would like to introduce in this chapter, including the magnetosheath, the magnetotail lobes (or in short: tail lobes), the plasmasheet, the plasmasphere and the inner magnetosphere.

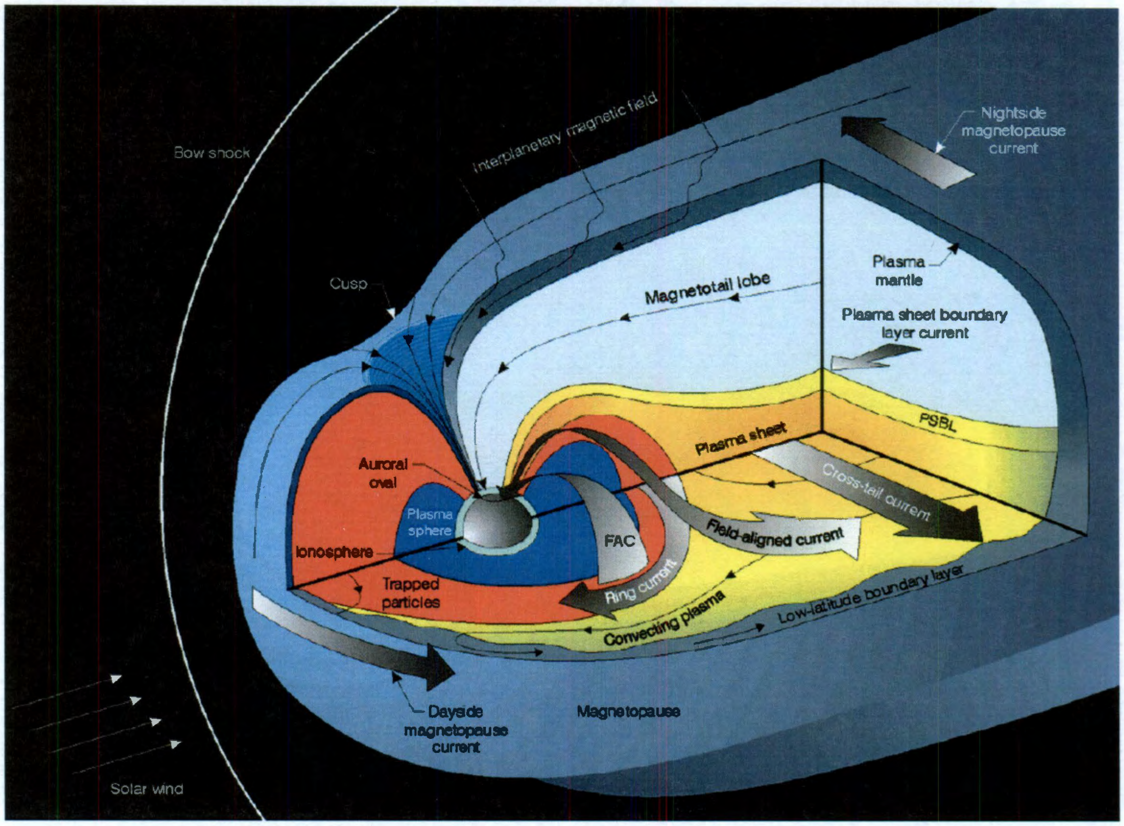

Figure 1.1 Cut-away drawing of the Earth's magnetosphere. The thick solid arrows represent currents in different regions. The thin solid lines linked to the high latitude region of the ionosphere are the magnetic field lines.

Between the bow shock and the blue colored magnetosphere boundary (magnetopause) is the magnetosheath where the decelerated plasma flows anti-sunward and the physics there is mainly dominated by gas dynamics, i.e. the solar wind's magnetic field does not play an important role because its energy density is much smaller than the flow energy. Only in the region near the magnetosphere nose, known as the subsolar point, where the flow speed is slow, the magnetic field becomes large, leading to the squeezing of plasma along field lines in a process known as the Zwan-Wolf effect [*Zwan and Wolf*, 1976].

The magnetotail lobe, shown in Figure 1.1, is dominated by magnetic energy since the magnetic field in the lobe is strong but the plasma is tenuous (low density). The field lines in the lobe have one end connecting to the ionosphere and the other end to the solar wind, when the IMF is southward. It is where most of the energy convected (see magnetosphere convection in section 1.2) from the dayside is stored. During geomagnetic active times, it is believed that the magnetic energy stored in the tail lobes is released and converted into particle kinetic energy and thermal energy. Figure 1.1 shows only the northern lobe, there is a southern lobe under the plasmasheet.

The plasmasheet, perhaps the most important region in the tail, is in the central part of the tail region in the night side, which divides the tail lobes into two. The plasma in the plasmasheet consists of very hot particles (*k*eVs) with typical average density ~0.1 - 2 cm^{-3}. The plasma energy in the plasmasheet is comparable or sometimes larger than the magnetic energy ($\beta = 2\mu_0 p / B^2$ is larger than 1, p is the plasma pressure, B is the magnetic field strength and μ_0 is the vacuum permeability). Since the magnetic field is stretched in the plasmasheet and in opposite directions above and below the center sheet, a current layer flows dawn to dusk and it is called the cross-tail current. The plasmasheet is quite dynamic during geomagnetic active times and it provides the source of plasma that is injected into the near Earth inner magnetosphere.

The innermost part in the magnetosphere is called the plasmasphere, which contains cold and dense plasma co-rotating with the Earth (the other parts of the magnetosphere do not co-rotate with the Earth). The typical density range of the plasmasphere is around two to several hundred particles per cm^3 [*Gallagher et al.*, 2000] from the plasmapause (sharp boundary of the plasmasphere) to the near Earth region. The temperature of the plasmasphere particles is around 1eV.

The inner magnetosphere, which is shown in red in Figure 1.1, usually extends from the dayside magnetopause to the nightside 7-9 R_E (Earth radii). It contains the low energy plasmasphere, the high energy ring current and a very high energy population called the radiation belts. James A. Van Allen discovered the radiation belt (also called the Van Allen belts) in the 1950s.

Particles from the plasmasheet can get into the inner magnetosphere and the electrons and ions follow different flow paths (gradient/curvature drifts, also see 1.5). The westward drifting ions form the ring current and partial ring current. The partial ring current closes at the ionosphere through Field-Aligned Currents (FAC or Birkeland currents). Figure 1.2 shows a statistical example of Birkeland current pattern on the ionosphere adapted from observations [*Iijima and Potemra*, 1976]. The downward currents on the dusk side and the upward currents on the dawn side (the equatorward set) are usually called the region-2 currents. The poleward set is called the region-1 currents.

The electrodynamic coupling between the inner magnetosphere and the ionosphere is very important.

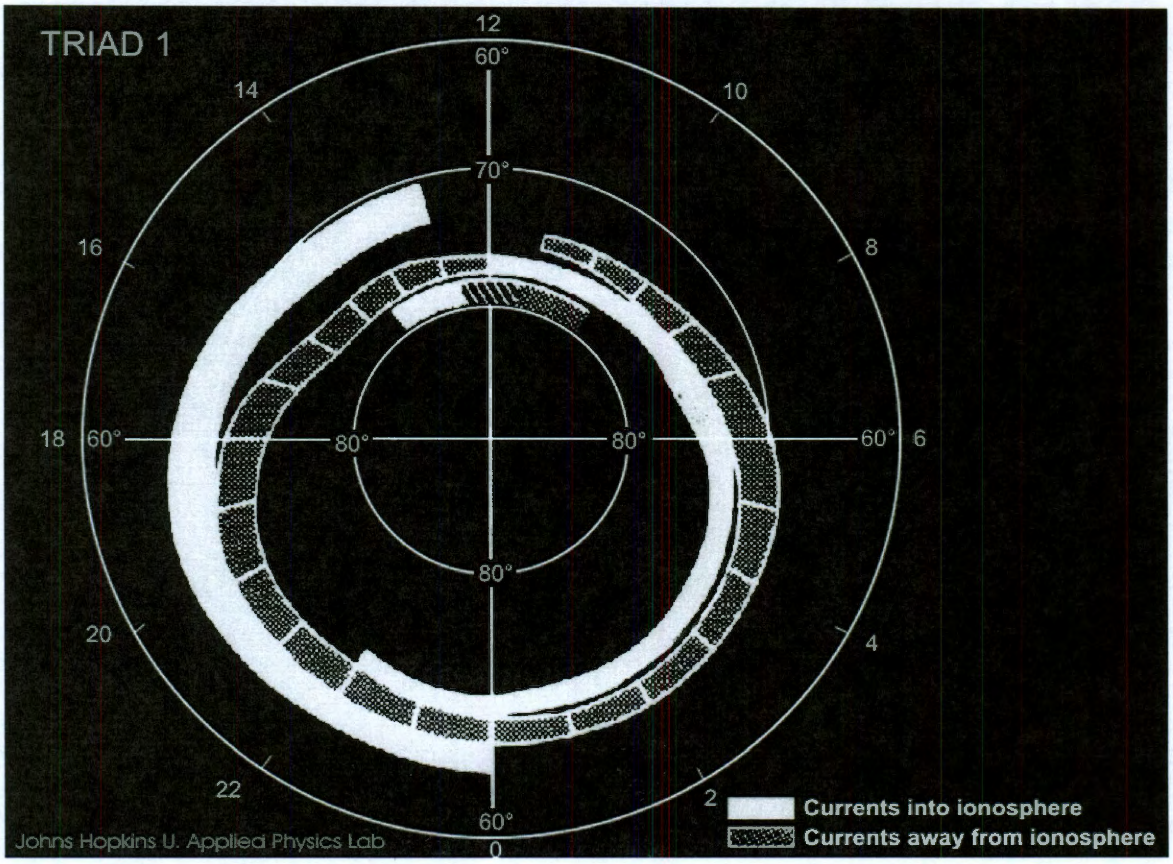

Figure 1.2 Birkeland current patterns on the ionosphere. Adapted from Johns Hopkins U. Applied Physics lab website.

1.2 Magnetospheric convection

The magnetosphere is a dynamic system and the plasma/magnetic field properties vary with time and depend on the driving of the solar wind and IMF. However, on average, the overall flow in the magnetosphere is directed sunward and the flow in magnetosheath and the cusp is anti-sunward. If we assume zero parallel potential drop along the field line and the frozen-in-flux condition, there is a similar view in the ionosphere (mapping). Figure 1.3 shows the overall flow pattern in the magnetosphere and in the ionosphere. Over the polar cap, the flow is anti-sunward but in the lower latitude regions the flow is directed sunward. This overall flow shown in panel C of Figure 1.3 is called magnetosphere convection.

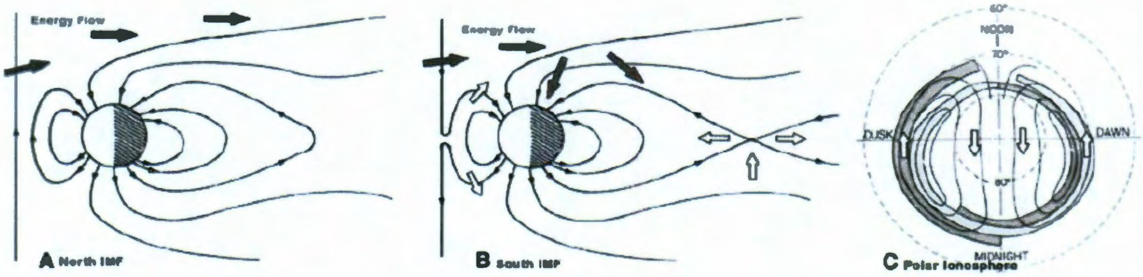

Figure 1.3 Plots of dayside reconnection and typical flow pattern showing the magnetosphere convection. (A) Flow and field line configuration when the IMF is northward. (B) Flow and field line configuration when the IMF is southward. (C) Flow mapped into the ionosphere when the IMF is southward. The Sun is to the left for A, B and is up for C. Figure adapted from *Lyon*, [2000].

The most important mode for magnetosphere convection is described by the Dungey's open model [*Dungey*, 1961] (also shown in Figure 1.3). On the dayside, the solar wind particles compress the dayside magnetic field. When the IMF is southward, it can reconnect with the northward directed Earth dipole-like field, which leads to connection of the Earth's internal field to the IMF. These field lines are called open field lines and are dragged anti-sunward by the solar wind. Magnetic flux is then added into the magnetotail lobes as well as energy. As the tail field lines become stretched, magnetic reconnection occurs which reconnects two open field lines back to a closed field line (two ends of the field line each connects to one of the hemispheres). These newly reconnected closed field lines are convected sunward to the dayside where they are reconnected with the IMF again. This model was proposed by Dungey in 1961 and is now regarded as the most important process during geomagnetically active times. Processes other than the Dungey's open model such as viscous interaction also play important roles in the convection [*Axford and Hines*, 1961].

1.3 Geomagnetic substorms and storms

During geomagnetic active times, the most dynamic responses of the magnetosphere are geomagnetic substorms and storms. There is another common mode which is called Steady Magnetosphere Convection (SMC) during which the convection is enhanced but without substorm expansions [*Sergeev et al.*, 1996a], but substorms and storms are more dynamic and have larger impact on the Earth.

1.3.1 Substorms

The geomagnetic substorm is a relatively rapid process where the magnetic energy stored in the tail is converted into kinetic and thermal energy [*Akasofu*, 1964]. It has a growth phase, an expansion phase and a recovery phase. During a substorm (~minutes to an hour), a number of phenomena are observed in space and on the ground. During the growth phase, the tail magnetic field becomes highly stretched and the current sheet in the tail thins. At the onset of the expansion phase, the expansion/brightening of aurora is often observed at high latitudes. Perturbations of magnetic field are often detected by ground-based magnetometer at the onset of substorm. Geosynchronous satellites often detect the injection of higher energy particles near the onset of the substorm (substorm injection) as well as channels of earthward flow. The trigger mechanism of the substorm onset is unfortunately still not known and has been the subject of ongoing debate in the magnetospheric community. A commonly accepted view that is yet to be identified is internal plasma instabilities in the tail lead to the onset of the substorm. The external driver also seems to play a role as many substorm expansions are found to be after a northward IMF turning [*Wild et al.* 2009]. We will return to substorms in Chapter 2 and 5.

1.3.2 Storms

Compared to substorms, storms are longer-term processes that can last several days and they usually have a larger impact on the Earth. Storms are often results of abrupt ejection of mass from the Sun called Corona Mass Ejection (CME) but some storms are driven by

Corotation Interaction Regions (CIR).

There are usually 3 distinct phases for a typical storm: the sudden commencement, the storm main phase and the recovery phase. Because of the major compression of the CME on the dayside, a sudden increase in the northward component of the low-latitude ground magnetic field is observed at sudden commencement, followed by a decrease in the storm main phase due to the major increase of the ring current. Substorms can be often found to occur during the course of a storm. The main phase usually lasts several hours but the recovery phase during which the horizontal magnetic field returns to pre-storm values can last several days. Ring current intensifies during the main phase, due to the increased convection of the injection of low entropy plasma [*Lemon et al.* 2004]. The strengthened ring current gradually decays during the recovery phase due to losses such as charge-exchange and precipitation.

1.4 Space Weather

Space Weather is the study of the environmental conditions on the Sun, the Earth's magnetosphere and ionosphere that have a societal impact on the Earth. The term Space Weather emerged in the 1990s when it was realized that space conditions could have significant impact on both Earth-based and space-based human technology. Variation of the solar wind causes changes of magnetospheric conditions can result in magnetospheric responses such as substorms and storms. Particularly, a severe storm, for example, could cause substantial damage to our technological assets. Thus another important and practical aspect that warrants our research is to understand and predict space weather.

Figure 1.4 shows several important identified impacts that severe space weather can have on our society that is now heavily relying on advance technology. I will briefly introduce these impacts in 1.4.1 and 1.4.2.

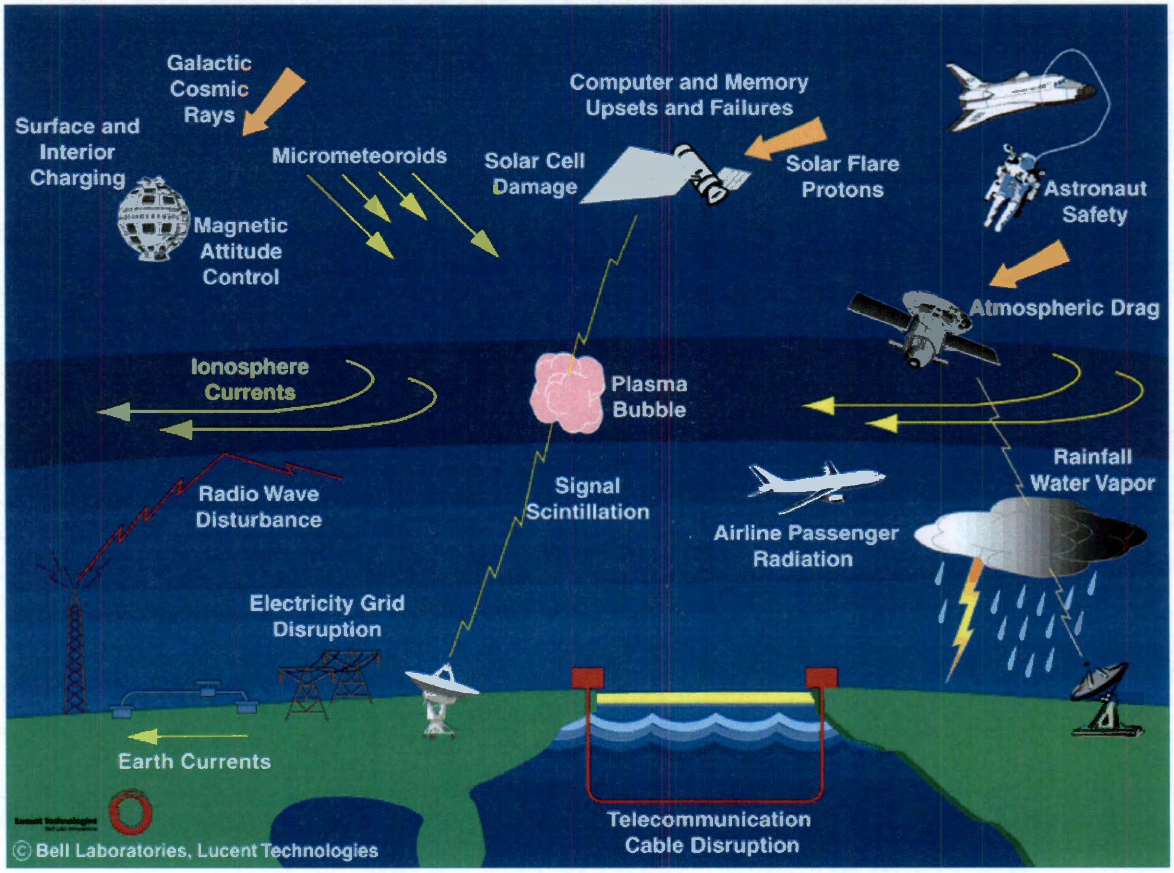

Figure 1.4 Illustration of space weather impacts on our technology dominated society. Adapted from NASA website.

1.4.1 Ground-based impacts

During storms and substorms, the electron content in the ionosphere is disrupted and currents are enhanced. That can disturb spacecraft to ground communication, such as the GPS signal. It can also affect the propagation of shortwave signals that are used in long-distant transmissions and radars since the wave would no longer be reflected at the ionosphere in a normal way. Radiation in the upper atmosphere will increase and could pose a health hazard for airline passengers especially for those on flights near the poles. Large perturbations in the magnetic field can also induce large currents on pipelines and electric power lines on the ground and lead to large-scale black-outs in power which can cause loss of billions of dollars. The induced currents can also disrupt communications through metal-based cable systems.

The perturbation of ground magnetic field can also destroy work done by our colleagues in the geosciences department. One of their inversion methods uses the measured change of magnetic field to infer sub-surface information. During a large storm/substorm, the change of magnetic field by the storm/substorm can be several orders of magnitude larger than the change caused by sub-surface conditions so that large errors would be introduced in their seismic image results. Modern oil-exploration surveys also heavily depend on the accuracy of the positioning system and the disruption of GPS signals could cause problems as well.

1.4.2 Assets in space

The increase of high-energy particles during severe space weather can be harmful to the onboard electronic systems on satellites. These particles can cause errors in computers or sometimes destroy the electronic hardware. Another common harmful effect caused by these particles is called spacecraft charging. It takes a lot of resource to launch and maintain spacecrafts and failures caused by theses high-energy particles are costly.

The radiation could also be harmful to humans in space. As astronauts are already exposed to higher radiations in space, the increase of radiation during severe space weather can be deadly.

1.5 Modeling of the Earth's magnetosphere

As space weather is very important to our society, efforts have been underway to obtain ability to predict space weather. Particularly, the space weather modeling effort is a promising way to describe the entire geospace environment by computer simulations.

To understand the Earth's magnetosphere, researchers generally take two approaches. One is experimental: satellites or probes are launched into space to measure interested quantities (plasma properties and fields) *in situ* or take a globe picture of emissions (image systems); magnetometers can measure magnetic perturbations on the ground; radar imagers can measure flow velocity and plasma density in the ionosphere. These experimental efforts provide direct information of the magnetosphere/ionosphere system and guide our theoretical research.

In a simple view, the plasma in the Earth's magnetosphere can be completely described by the Boltzmann's equation. If we further assume the plasma is collisionless, the simpler Vlasov equation (Boltzmann's equation without the collisional term) can also be used. With the addition of the Maxwell equations, the dynamics of the magnetospheric plasma can be completely described. However, these equations are hard to solve due to the large-scale size and complicated geometry. To reproduce the real dynamics in the magnetosphere, computer modeling has to be used. I will introduce 4 classes of widely used methods in the sub-sections below sorting by the computational cost from high to low.

1.5.1 Vlasov method

The Vlasov equation describes the evolution of the plasma phase space density $f(\vec{x},\vec{v},t)$ as:

$$\frac{df(\vec{x},\vec{v},t)}{dt}=\frac{\partial f}{\partial t}+\vec{v}\cdot\frac{\partial f}{\partial \vec{x}}+\frac{d\vec{v}}{dt}\cdot\frac{\partial f}{\partial \vec{v}}=0 \qquad (1.1).$$

If the right-hand side is replaced with a collisional term, then the Vlasov equation becomes the Boltzmann equation. Other than the Vlasov equation, a Vlasov model also includes the following to close the equations:

$$
\begin{aligned}
&\frac{d\vec{v}}{dt} = \frac{q}{m}(\vec{E} + \vec{v} \times \vec{B}) \\
&\nabla \times \vec{E} = -\frac{\partial \vec{B}}{\partial t} \\
&\nabla \times \vec{B} = \mu_0 \vec{J} + \frac{1}{c^2}\frac{\partial \vec{E}}{\partial t} \\
&\nabla \cdot \vec{E} = \frac{\rho}{\varepsilon_0} \\
&\nabla \cdot \vec{B} = 0 \\
&\frac{\partial \rho}{\partial t} + \nabla \cdot \vec{J} = 0
\end{aligned}
\qquad (1.2),
$$

in which ρ is the charge density and the other quantities have their normal meanings.

Using the Vlasov equation to model the magnetosphere is perhaps the ideal approach as it is complete (contains all the physics for the collisionless space plasma) and clean in terms of numerics. However, solving Vlasov equation is extremely costly even with today's most advanced supercomputers. As of today, Vlasov codes are often applied to waves, small-scale processes, e.g., reconnection and 2D/2.5D global simulations with limited boundary conditions [*Umeda*, 2011].

1.5.2 Particle-in-cell (PIC) method

PIC codes are, in a sense, approximate solutions to Vlasov equations. PIC codes track the trajectories of charged particles in electromagnetic fields, in a self-consistent fashion. The particles can be anywhere in the modeling region but the fields are only solved on a finite grid, thus the name "particle in cell" method. Usually the codes calculate charge ρ and current densities J on the grid by assuming a shape function S:

$$\rho(\vec{x}) = \sum_i q_i S(\vec{x} - \vec{x}_i) \qquad J(\vec{x}) = \sum_i q_i \vec{v}_i S(\vec{x} - \vec{x}_i) \qquad (1.3).$$

Then the charge and current densities are plugged into the Maxwell equation (2nd-5th equation shown in equation set (1.2)) to update the electric and magnetic field. The last step is to use updated electromagnetic fields to advance particle in real and velocity space using the Lorentz force equation (1st equation in equation set (1.2)).

The PIC codes are less computationally expensive than the Vlasov codes but they are still expensive compared to fluid-based codes. They are used in nearly every discipline of plasma physics including magnetic confinement fusion, space plasma physics and etc, mostly on small-scale problems.

There are some common issues with the PIC codes. One is the statistical noise due to finite number of particles (particle number is much smaller than reality), so one has to find a balance between the number of particles, which is constrained by computer resources and numerical noise. If one part of the modeling region cannot be covered by enough test particles, one has to find ways to fill in new particle if this region is important for your results. The other compromise in the PIC codes is to use an artificial proton to electron mass ratio, also due to computational constraints [*Bret et al.*, 2010]. Limited boundary conditions can be applied to PIC codes and periodical boundary conditions are often used for PIC simulations.

1.5.3 Hybrid methods

The hybrid method uses the idea that if we don't have enough resource to treat all plasma as particles, we can treat some of them as a fluid. Thus one can use the PIC method for one particle type and use fluid (MHD) method (section 1.5.4) for other species. Usually the ion kinetics is treated by PIC method and the electrons are treated as fluid. Careful treatment of the separated scales is required in a hybrid code [*Buchner et al.*, 2003].

1.5.4 MHD and related methods

As the focus of this thesis research is on the topic of MHD of its related methods. In this sub-section, I will introduce in more detail the basics of MHD of related methods. The MHD and other related fluid methods are still the most widely used methods in space plasma modeling. They tend to neglect some of the physics that PIC/Vlasov codes have but they are less computational expensive and seem to do a reasonable job of reproducing large-scale features.

1.5.4.1 MHD modeling of the global magnetosphere

An MHD model solves a form or variation of the ideal MHD equations list below.

$$\frac{\partial\rho}{\partial t}+\nabla\cdot(\rho\vec{v})=0$$

$$\rho\frac{d\vec{v}}{dt}=\vec{J}\times\vec{B}-\nabla p$$

$$\frac{d(p/\rho^{\gamma})}{dt}=0$$

$$\begin{aligned}&\frac{\partial\vec{B}}{\partial t}=-\nabla\times\vec{E}\\&\vec{E}+\vec{v}\times\vec{B}=0\\&\vec{J}=\frac{1}{\mu_o}\nabla\times\vec{B}\\&\nabla\cdot\vec{B}=0\end{aligned} \qquad (1.4),$$

in which ρ is the ion mass density, $\boldsymbol{J}$ is the current density and p is plasma pressure. γ is usually set to be 5/3, the ratio of specific heats. These equations can be derived from the collisional Boltzmann equation with some assumptions such as: (1) the system is a low-frequency and long-wavelength system, i.e. system size is much larger than the ion inertial length and time scales interested are much longer than the ion gyration period. (2) The net charge is zero in a macroscopic sense. (3) Assume the electron mass is zero. (4) The system is collision dominated so the collision frequency is much larger than other frequencies. For the plasma in the Earth's magnetosphere, these assumptions are usually good except the last one (in fact space plasma is mostly collisionless). Nevertheless, the ideal MHD equations still produce reasonably realistic results for large-scale plasma behavior since they are at least conservative equations that conserve mass, momentum and energy [*Chan*, lecture notes]. There are some variations of the ideal MHD equations, for example, the resistive MHD uses $\vec{E}+\vec{v}\times\vec{B}=\eta\vec{J}$ (η is the resistivity) instead of $\vec{E}+\vec{v}\times\vec{B}=0$ (frozen-in-flux) and the Hall MHD adds another term proportional to $\vec{J}\times\vec{B}$ in the Ohm's law.

There are numerous computational models that solve the MHD equations in various geometries for different applications. However, for the Earth's magnetosphere, it is usually not enough to just have a MHD solver since the inner boundary (the Earth) and the magnetospheric coupling to the ionosphere have to be carefully treated. If we limit our discussion on MHD models that are for the Earth's magnetosphere geometry and have some form of ionosphere coupling, then there are 4 popular models, namely, the BATS-R-US (Block Adaptive Tree Solarwind Roe Upwind Scheme) [*Powell et al.*, 1999], the OpenGGCM (Open Geospace General Circulation Model) [*Raeder et al.*, 2001], the LFM (Lyon-Fedder-Mobarry) [*Lyon et al.*, 2004] model and the GUMICS (Grand Unified Magnetosphere Ionosphere Coupling Simulation) [*Janhunen et al.*, 1996].

The main differences among these models lie in the form of equations (full conservative or semi-conservative) solved and the numerical methods used. The MHD numerics includes considerations on choice of grid, numerical solver for conservative law and approach to conserving magnetic flux. For the popular models listed above, BATS-R-US and GUMICS are implemented with more advanced, automatically refined Cartesian grids that can allow resolution change during the simulation. The OpenGGCM and the LFM use fixed grids but the LFM's grid is a deformed spherical grid

(BATS-R-US also has an option to use a polar grid) while the OpenGGCM uses a stretched-Cartesian grid which is much easier to parallelize.

The numerical solver is a scheme to solve a general conservative equation $\frac{\partial U}{\partial t}+\nabla\cdot\vec{F}(U)=0$ where U is a physical quantity such as mass and F is the physical flux. There are many ways to solve this kind of equation and we will discuss MHD solvers in more detail in Appendix C.

Conservation of magnetic flux is in fact a particular difficulty in MHD modeling. In equation set 1.4, the $\nabla\cdot\vec{B}=0$ equation basically provides an initial condition constraint and violation of $\nabla\cdot\vec{B}=0$ would lead to serious errors in the simulation [*Brackbill and Barnes*, 1980]. The most commonly used approach to conserve $\nabla\cdot\vec{B}=0$ is the so-called Constrained Transport (CT) method [*Evans and Hawley*, 1988] which can be achieved by a staggered mesh approach [e.g. *Yee et al.* 1996]. The LFM and the OpenGGCM (probably GUMICS as well) use this method to keep $\nabla\cdot B$ to numerical roundoff. BATS-R-US uses another approach that modifies the MHD in a way that $\nabla\cdot\vec{B}$ accumulated in the simulation region is propagated out of the boundaries [*Powell et al.* 1999]. There is also an expensive way to clean $\nabla\cdot\vec{B}$ by solving a Poisson equation. A good review of ways to conserve $\nabla\cdot\vec{B}$ can be found in *Toth*, [2000].

All these models take just the inputs (the solar wind and IMF) at the sunward boundary and then they can self-consistently solve for the time evolution of the magnetic field and plasma movement in their simulation region. In general, quantities related to larger scale features such as the location of the bow shock, the standoff distance (location of the magnetopause) and tail structures from the MHD models are thought to be realistic. Other quantities such as the reconnection location can also be realistic even though the MHD physics doesn't describe the micro-physics related to reconnection. (See Chapter 5 for a study related to reconnection using MHD). There are a lot of uncertainties for other MHD outputs especially for the near Earth region (e.g. the inner magnetosphere) where the model resolution is poor. MHD model results should always be treated with caution and we need to determine if the results are physical or numerical which can be quite difficult.

1.5.4.2 Inner magnetosphere models

In the inner magnetosphere, single fluid MHD cannot describe the dominant physics. Inner magnetosphere or ring current models such as the Rice Convection Model (RCM) [*Toffoletto et al.*, 2003], the Comprehensive Ring Current model (CRCM) [*Fok et al.*, 2001] and different versions of the RAM [Ring current-Atmosphere interaction Model] model [*Jordanova et al.* 2001; *Liemohn et al.* 1999] are carefully designed to treat the important energy dependent drift physics. These models differ slightly by formalism and whether the electric field is self-consistently computed. Only the standalone RCM assumes isotropic distribution, CRCM and RAM track the pitch-angle distribution.

I will just use the RCM's formalism as an example to describe inner magnetosphere drift physics, which starts from single charged particle motion in an electromagnetic field. In the magnetosphere, considering the dipole-like magnetic field, charged particles have three basic motions: (1) gyro-motion around the magnetic field. (2) bounce motion along the magnetic field. (3) drift motion perpendicular to the magnetic field. It is found that the time scale for each motion is widely separated so that there is an invariant associated with each of the three motions. If one further assumes isotropic distribution, the drift motion perpendicular to the magnetic field can be describe by

$$\vec{V}_D = \vec{V}_{E\times B} + \vec{V}_{GC} = \frac{\vec{E}\times\vec{B}}{B^2} + \frac{\vec{B}\times\nabla W_K}{qB^2} \qquad (1.5),$$

after applying the guiding-center approximation and averaging along the bounce motion. W_K is the kinetic energy of the particle. The first term in equation (1.5) is usually called the $\vec{E}\times\vec{B}$ drift and the second term represents the energy-dependent gradient and curvature drift. The drift velocity is then used to evolve the distribution function using conservation law $\frac{\partial\eta_s}{\partial t} + \vec{V}_D\cdot\nabla\eta_s = L + S$ where the density invariant η_s is defined as the number of particles per unit magnetic flux for a specific energy invariant. *s* can refer to different energy invariants or different species. *L* and *S* are losses and sources.

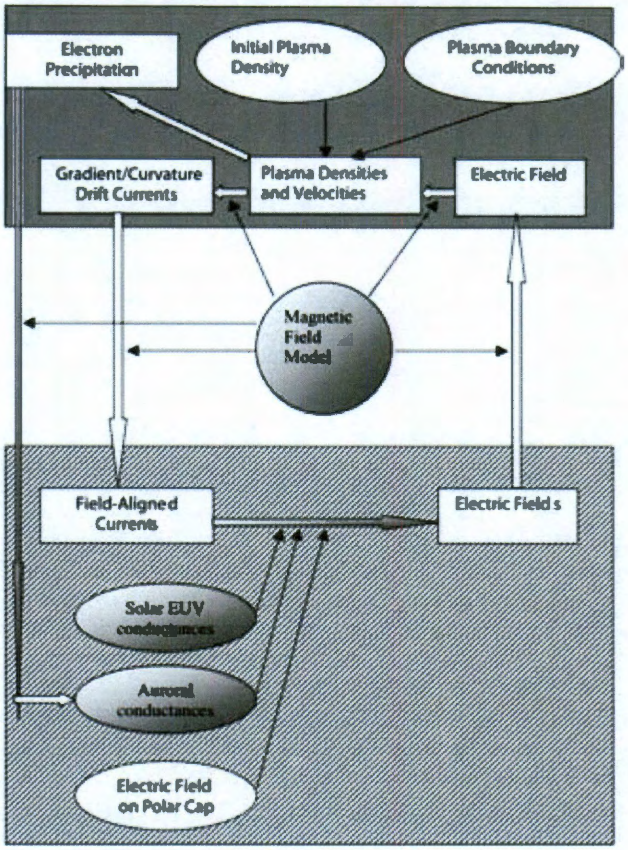

Figure 1.5 Flowchart of the Rice Convection Model. Adapted from *Sazykin*, [2000].

Changes in the plasma distribution in the inner magnetosphere affect the Birkeland currents that connect to the ionosphere system which result in changes in the electric field distribution which in turn affects the drifts. It is believed that the inner magnetosphere coupling to the ionosphere through Birkeland currents is important and a self-consistent electric field is need for accurately inner magnetosphere modeling. The M-I coupling is achieved by assuming zero potential drop along the magnetic field line and treating the ionosphere as a conductor. *Vasyliunas* [1970] proposed a logic loop for the M-I coupling, by plugging in the Vasyliunas equation $\frac{J_{\|in}}{B_{in}} - \frac{J_{\|is}}{B_{is}} = \frac{\hat{b}}{B} \bullet \nabla V \times \nabla P$ (assuming slow-flow and quasi-equilibrium) into the current conservation equation $\nabla_h \bullet (-\overleftrightarrow{\Sigma} \bullet \nabla_h \Phi) = (J_{\|in} - J_{\|is}) \sin(I)$ to get the fundamental equation of magnetosphere-ionosphere coupling:

$$\nabla_h \bullet (-\Sigma \bullet \nabla_h \Phi) = \sin(I) B_i (\frac{\hat{b}}{B} \bullet \nabla V \times \nabla P) \qquad (1.6).$$

For the above equations, V is the flux tube volume, P is the plasma pressure, J represents currents into the ionosphere and the subscripts s and n mean southern and northern hemisphere, I is the inclination angle, $\overleftrightarrow{\Sigma}$ is the ionospheric conductance tensor and Φ is the ionospheric potential. Using the potential obtained from equation (1.6), the new drifts can be calculated using equation (1.5). These formulas are represented in the RCM as shown in the flowchart in Figure 1.5.

The ring current models are usually very accurate numerically compared to the MHD models. However these models need time-dependent magnetic field model everywhere in the modeling region and the plasma distribution at the poleward boundary. These inputs are usually obtained from empirical models but in this case the magnetic field is not necessarily consistent with the plasma. To have the magnetic field self-consistently calculated, the RCM has been coupled to a magneto-friction code [*Toffoletto et al.* 2003]. The new RAM-SCB (RAM-self-consistent B field) model also has been coupled to a model similar to the friction code [*Zaharia et al.* 2004]. Chapter 2 and 3 will describe another approach to couple the RCM to MHD code so that not only the magnetic field is self-consistently computed but also the plasma outer boundary condition.

1.5.4.3 The magneto-friction code and the RCM-E

The friction code is a special MHD code to solve for a magnetosphere equilibria configuration, i.e. a solution satisfying $J \times B = \nabla p$ where J is the current density and p is the plasma pressure. In the friction code, a small friction term is added into the MHD momentum equation so that the system will evolve to a state with the lowest energy (force balanced).

With the coupling of the magneto-friction code to the RCM, the RCM-E [*Lemon et al.*, 2003] is a powerful model that has been used to simulate a lot of events [*Yang*, 2010]. Comparing to the MHD, the RCM-E has limitations that it cannot treat fast flow or reconnection, since the RCM assumes slow flow and neglects waves. However the RCM-E conserves the entropy (more on entropy in Chapter 2, 5) better than the MHD models. We will further describe the ongoing development of a new version of the friction code in Appendix C using newer numerics.

In the future it is hoped that all the models described in this section will be better and have more and more capabilities, so that eventually we are able to build a comprehensive frame work that can accurately represent all the regions in the magnetosphere and has the power to forecast space weather.

Chapter 2

One-way Coupling of the OpenGGCM and the RCM

2.1 Motivation

As stated in Chapter 1, the global magnetohydrodynamics (MHD) models cannot represent the inner magnetosphere well. Improving MHD models by adding missing physics to particular regions of the magnetosphere has been a longstanding goal in magnetospheric modeling [e.g. *Raeder*, 2003, 2006; *Lyon*, 2004; *Tóth et al.* 2005, 2007]. This chapter describes the forward coupling effort between the OpenGGCM and the RCM where the RCM takes inputs from the OpenGGCM to study a substorm injection event.

In the inner magnetosphere, energy dependent gradient and curvature drifts are important [*Wolf*, 1983] but are not represented in the MHD transport equations ($E + v \times B = 0$), and efforts have been underway for several years to couple global MHD models to various inner magnetosphere models [e.g. *Toffoletto et al.* 2003, *Fok et al.* 2001, *Jordanova et al.* 2001; *Liemohn et al.* 1999]. Such coupled models are expected to give a more accurate representation of ring current dynamics and the associated coupling to the ionosphere. Inner magnetosphere models, such as the Rice Convection Model (RCM), require certain inputs such as the magnetic field and plasma boundary condition. By coupling to a global MHD model, the RCM inputs can be self-consistently computed. Thus a more comprehensive model of the Earth magnetosphere can be obtained. Before I stepped into the area of space physics modeling, efforts to couple the MHD to inner magnetosphere models were already underway. *De Zeeuw et al.* [2004] firstly presented results from an effort to couple the BATS-R-US [*Powell et al.* 1999] global MHD code and the RCM, in which a two-way coupled BATS-R-US/RCM (where the RCM feeds back pressure) showed some encouraging improvements in the MHD code results, including more pronounced and well defined region-2 currents and more realistic inner magnetosphere pressure. *Toffoletto et al.* [2004] presented their results from the LFM [*Lyon et al.*, 2004]-RCM and showed that one-way coupling produced more realistic region-2 currents and ring-current-ion pressures in the RCM. More recently, *Fok et al.* [2006] used LFM results of a substorm simulation as input to the CRCM [*Fok et al.* 2001] and reproduced observable features of oxygen enhancement during a substorm. *Moore et al.* [2008] studied the effect of a plasmaspheric plume using results from one-way coupled LFM and CRCM model. In addition, *Buzulukova et al.* [2010] presented one-way coupled BATS-R-US and CRCM model simulations for both an idealized case and an actual storm and showed the model reproduced many known features of the inner magnetosphere dynamics.

For the OpenGGCM [*Raeder et al.*, 2001]-RCM coupling efforts, the forward mode (one-way) is an important first step before the complete two-way coupling. Because in the forward mode, the OpenGGCM would operate normally and its results would not be modified by the RCM, thus it is much easier to identify problems than two-way coupled code. The RCM is then driven by the MHD time-dependent data and we could test if the RCM results are reasonable so that we can then proceed with the two-way coupling. We will first introduce the coupling methodology and then use the forward coupling mode to simulate a substorm event that occurred on March 23rd, 2007. Unlike geomagnetic storms, which are the result of many hours or days of strong southward IMF, geomagnetic substorms events are shorter processes on a time scale of a few hours. Thus the process is expected to be less sensitive to RCM pressure feedback to the OpenGGCM. We chose the March 23rd event because it is a well-known THEMIS substorm that has been extensively studied [e.g. *Angelopoulos et al.,* 2008; *Keiling et al*., 2008a, 2008b; *Liu et al*., 2009; *Zhu et al.* 2009] and the standalone OpenGGCM simulation is available for comparison [*Raeder et al.*, 2008].

The standalone OpenGGCM simulation of the March 23rd event reasonably well reproduced many substorm salient features including rapid field dipolarization, a westward traveling surge, and an increase in density observed by some THEMIS probes [*Raeder et al.,* 2008]. The magnetic field produced by the model also shows good agreement with THEMIS observations. However, as the MHD description is only single fluid, lacking inner magnetosphere energy dependent drift physics, it can only provide single fluid information about a particle injection, and is not able to capture dispersion features related to energetic particle injection [e.g. *Belian et al.* 1978; *Mauk and Meng*, 1987; *Thomsen et al.,* 2001]. Injection of high-energy particles into the inner magnetosphere is one of the major indicators of substorm onset. There are already many models that use test particle simulations in either specified electromagnetic pulse or precomputed MHD electric and magnetic field [e.g. *Zaharia et al.,* 2000, 2004; *Birn et al*., 1997, 1998; *Li et al.,* 1998, 2003; *Liu et al*., 2009]. *Taktakishvili et al.* [2007] did metrics analysis on two proton injection events using the Fok ring current model [*Fok et al.,* 1999] driven by precomputed magnetic/electric field and plasma information from the BATS-R-US MHD model, and found the model performed fairly well for the injection event under strongly varying solar wind conditions. *Zhang et al.* [2007] did a storm simulation using two-way coupled BATS-R-US/RCM; they compared the model outputs to geosynchronous plasma moments data and they found good agreement. Our initial assumption in this work was that the OpenGGCM reasonably well represents the magnetic field during the substorm. Since the effect of the induced electric field is implicitly included through time-dependent magnetic field mapping [*Toffoletto et al.,* 2003], the coupled OpenGGCM-RCM model is a self-contained tool to cover the injection part of the substorm simulation.

Another important implication of this simulation is to verify and confirm the picture of low entropy flow channels. Recent work using the RCM to simulate substorm injections has shown the consistency of the picture that these injections are associated with earthward moving magnetic bubbles. A bubble is defined as a set of magnetic flux tubes in the magnetosphere that have a lower entropy parameter $PV^{5/3}$ than their surroundings [e.g. *Pontius and Wolf*, 1990; *Birn et al.*, 2004; *Zhang et al.*, 2008, *Wolf et al.*, 2009], where P is the plasma pressure and $V = \int_{s}^{n} dS / B$ (B is the magnetic field strength and the integral is along the magnetic field line, from the southern hemisphere to the northern hemisphere) is the flux tube volume. It is believed that these bubbles are produced by an non-adiabatic process such as magnetic reconnection [*Birn et al.*, 2006] or current disruption in the inner part of the plasmasheet [e.g. *Lui*, 1992; *Sitnov et al.,* 2007; *Wolf et al.*, 2009] and they are important for plasma transport from tail to the inner magnetosphere [e.g. *Lyons et al.*, 2003; *Apatenkov et al.*, 2007; *Sergeev et al.*, 1996b]. Observational evidence of a bubble propagation into the inner magnetosphere has emerged from Cluster and Double Star observations [e.g. *Walsh et al.,* 2009], which support the existence of an earthward moving bubble as near as 7 R_E. Recent modeling work has also suggested that these bubbles play a crucial role in the injection of plasma into the stormtime ring current. Using a self-consistent RCM-E simulation, where the magnetic field is computed to be in force equilibrium with the RCM-computed plasma pressures, *Lemon et al.* [2004] showed that even under strong convection, plasma cannot be injected into the inner magnetosphere, unless one reduces $PV^{5/3}$ below typical middle-plasma-sheet values. *Yang et al.* [2008] simulated a saw-tooth event using the RCM, by treating each tooth as separate substorm and manually reducing the $PV^{5/3}$on the RCM boundary at each expansion phase with the intentional goal of matching observations. The simulated energetic particle flux and neutral atom fluxes matched well with observations. *Zhang et al.* [2008, 2009] presented another RCM simulation that injects a bubble into the inner magnetosphere, also by performing a reduction of $PV^{5/3}$ over a range of local time at the RCM simulation boundary, and correspondingly increasing the electric field E_y. In either of the above simulations, a bubble is introduced through the RCM outer boundary assuming that the bubble is produced by a process outside the RCM modeling region. Thus, a RCM or RCM-E simulation of a substorm always involves a depletion of $PV^{5/3}$ on the boundary resulting in the injection of the bubble. In this study, when the substorm produces bubbles in the MHD model, they propagate into the inner magnetosphere via interchange [*Wolf et al.*, 2009].

In this chapter, we use the one-way coupled OpenGGCM-RCM model to study the injection event in the March 23rd, 2007 substorm and compare model results with data from different LANL geosynchronous satellites. We explore the features of the bubble that was injected into the inner magnetosphere during the substorm expansion phase and discuss the creation of the bubble. In the initial run, we used the ionospheric potential distribution computed by OpenGGCM to compute the ionospheric potential distribution that transports particles in the RCM. We will label this run RCM Run1 or Run1 in this chapter. We also present a comparison run that uses the ionospheric electric field computed from RCM pressures and Birkeland currents. This run will be labeled as RCM Run2 or Run2. The first part of this chapter will describe in detail the model setup and coupling methodology. In the second part, we show model results of the substorm event including comparisons with observations. In the latter part of the chapter, we explore how the bubbles are created in the MHD simulation and also discuss features of the self-consistent electric field. The last section gives conclusions and summarizes the chapter. Appendix A describes the equations used in the information exchange in the code coupling.

2.2 Model descriptions and setup

2.2.1. OpenGGCM description

The OpenGGCM is a large-scale model of the Earth's magnetosphere originally developed at UCLA by Jimmy Raeder [*Raeder et al.,* 1998]. The OpenGGCM self-consistently solves the MHD equations for the magnetic field, plasma density and pressure and ionosphere potential in its simulation domain. The current version of OpenGGCM consists of three components: the global magnetosphere, the ionosphere and the CTIM (Coupled Thermosphere Ionosphere Model) [*Fuller-Rowell et al.,* 1996; *Raeder et al.*, 2001] module. The global magnetosphere model solves the semi-conservative MHD equations inside the simulation domain (the simulation box is usually 600R_E by 100R_E by 100 R_E) to the inner boundary which is at about 3.5R_E. The OpenGGCM uses a stretched-Cartesian grid which not only allows straightforward and efficient parallelization, but also has optimized grid resolution near regions of interests. For spatial discretization, the

OpenGGCM uses a hybrid flux construct scheme (switch between a fourth-order and a first-order Rusanov flux scheme, depending on the gradients in the solution.) and an explicit predictor-corrector finite difference scheme in time stepping. It is important in every MHD model that the divergence of magnetic field is kept close to zero and the OpenGGCM achieves this by putting variables on a staggered grid, which can maintain zero divergence to numerical roundoff [*Evans and Hawley, 1988*]. The code uses an anomalous resistivity which is parameterized by the local current density, and is nonzero only when the normalized current density exceeds a specified threshold. Birkeland currents at the inner boundary are mapped to the ionosphere assuming a dipole magnetic field; these currents are used to solve for the potential in the ionosphere using $\nabla \cdot \Sigma \cdot \nabla \Phi = -j_{\parallel} \sin I$ where I is the field inclination angle at the ionosphere and Σ is the conductance tensor. The potential is then mapped back to the inner boundary of the MHD code which is used as a boundary condition. The ionospheric component of the model is coupled to the CTIM model, which takes inputs from the MHD model for electron precipitation parameters and electric field. It also uses parameterized solar 10.7cm flux and the tidal modes. CTIM self-consistently solves the neutral and ion fluid equations to provide conductances to the OpenGGCM ionosphere for the potential calculation. A detailed description of the OpenGGCM can be found in *Raeder* [2003] and *Raeder et al.,* [2008].

2.2.2 The Rice Convection Model

The Rice Convection Model (RCM) is an inner magnetosphere model that has been developed at Rice University [e.g. *Wolf, 1970*; *Jaggi and Wolf*, 1973; *Harel et al.*, 1981; *Wolf*, 1983; *Spiro et al.*, 1988] and is designed to carefully treat the physics of the inner magnetosphere and its coupling to the ionosphere using a scheme first proposed by *Vasyliunas* [1970]. By neglecting the inertial terms in the MHD momentum equation and assuming a known time-dependent magnetic field, the RCM computes bounce-averaged particle motion in the slow flow region of the inner magnetosphere on a 2 dimensional ionospheric grid. The RCM assumes an isotropic pitch-angle distribution and treats different energy components in the plasma distribution function as independent fluids (channels), each with an energy invariant λ_s. Using adiabatic drift convection theory, the kinetic energy for given plasma fluid with energy invariant λ_s and location *x* is given by $W(\lambda_s, x, t) = \lambda_s V^{-2/3}$. The RCM computes currents, electric field and particle $\vec{E} \times \vec{B}$ and gradient-curvature drifts of each channel self-consistently, given user specified plasma distribution and potential on the boundary. The basic equations used in RCM for the plasma evolution are

$$(\frac{\partial}{\partial t} + \vec{v}_s \cdot \nabla)\eta_s = S(\eta_s) - L(\eta_s) \tag{2.1}$$

$$\vec{v}_s = \frac{\lambda_s}{q_s B^2}\vec{B} \times \nabla V^{-2/3} + \frac{\vec{E} \times \vec{B}}{B^2} \tag{2.2}$$

$$\vec{E} = -\nabla(\Phi_{iono} + \Phi_{corotation}) \tag{2.3}$$

where $\vec{v}_s$ is the bounce-averaged particle drift velocity for channel s, η_s is the number of particles per unit magnetic flux(flux tube content), q_s is the particle charge, S and L are the sources and losses and $\vec{E}, \vec{B}$ have their usual meaning as electric and magnetic field respectively. The induction E-field is introduced by time-varying magnetic field mapping from the ionosphere. The RCM has its own routines for calculating Birkeland currents as well as ionospheric conductances and potentials, but in the coupled code, Φ_{iono} can come either from the OpenGGCM (for RCM Run1) or the RCM (for RCM Run2. A more detailed description of the RCM can be found in the review paper by *Toffoletto et al.* [2003] and the references therein.

2.2.3 Coupling methodology

As noted in the previous sections, the RCM and OpenGGCM work on different spatial domains and use different mathematical descriptions and coordinate systems. In order to couple the two codes, conversion of three-dimensional plasma moments to field-line averaged values and back is required. Figure 2.1 shows the diagram of the coupling methodology. Since the RCM operates only in the closed field line region, field lines are traced to find the open/closed boundary and MHD-based plasma information is averaged along the field line (See Appendix A). At each exchange time (every 1~5 minutes, 3 minutes used in this chapter), the MHD nodes assemble the necessary field and plasma information and send it to the RCM. The OpenGGCM ionosphere node also assembles the potential (without co-rotation), and when needed, the conductance information and sends them to the RCM. The RCM node then uses this information to prepare a run for the RCM, tracing from every RCM ionosphere grid point to get the field mapping information and flux tube volume, as well as the field-line-averaged temperature and density on the polar boundary. Coordinate transformations are conducted in the tracing to convert the MHD information, which is in GSE coordinates, to the RCM, which works in SM coordinates. (The standalone RCM can be thought to be working in GSM coordinates, though, since GSM and SM are the same within the assumption of a zero dipole tilt).

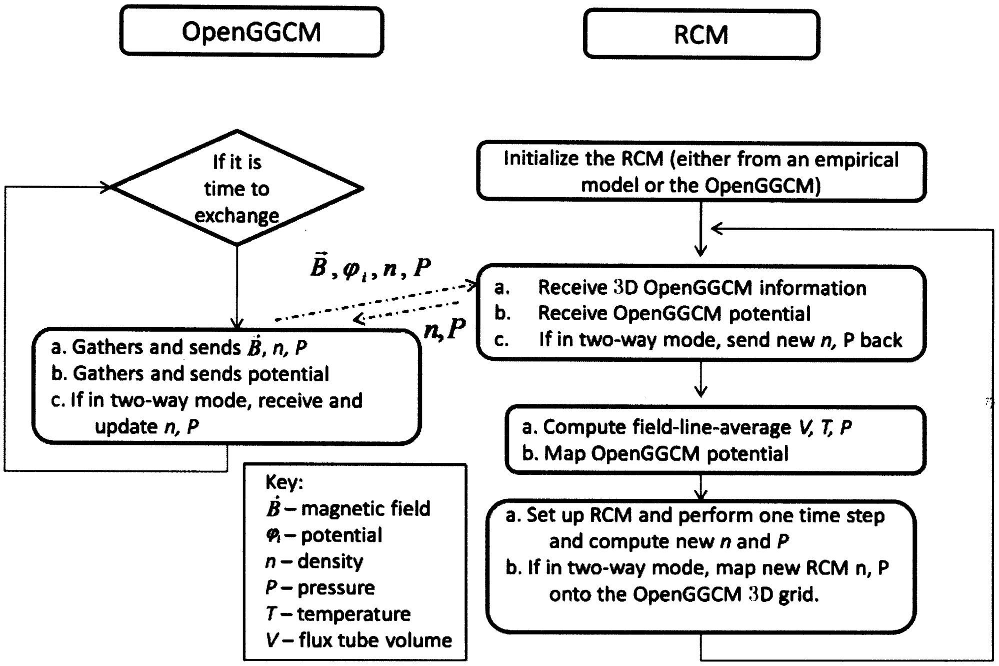

Figure 2.1 Diagram of OpenGGCM and RCM coupling methodology for the case where the RCM uses the ionospheric potential computed by OpenGGCM.

The RCM assumes symmetry between the two hemispheres and its grid is in the northern hemisphere. For simplicity, only the potential and conductance (for RCM Run2) on the OpenGGCM northern ionosphere are mapped onto the RCM grid, and the corotation potential is included in the RCM calculations. For MHD runs with non-zero dipole-tilt, the ionospheric potential is not necessarily the same at the ionospheric footprints of a field line, due to numerical errors in the MHD code, and that causes errors in the coupled-code results. Figure 2.2 indicates the size of this error, by comparing the

MHD-computed potential drop across the RCM modeling region for the two hemispheres; we find they differ by less than 20%. Due to the non-zero dipole tilt, the MHD conductances at the northern and southern ionospheric footprints of a field line may be the different; our use of just the northern-ionospheric conductance is also a source of error in the coupled-code results. Another option would be to use the averages of the MHD potentials for RCM Run1 and the total conductance, total Birkeland current, and average boundary potential for RCM Run2 [e.g. *Buzulukova et al.* 2010].

When the RCM gets all the necessary information, it creates input files which have the formats that are normally used by the standalone RCM. The coupling interface specifies the start and stop time and calls the main RCM program to run for an exchange interval. When the RCM finishes its calculation, it can use the MHD-based magnetic field to update the pressures and densities at MHD grid points. The OpenGGCM code runs simultaneously when RCM is running, until the next exchange time, at which the MHD nodes will receive updated RCM pressure and density information. The MHD can choose to use this information to nudge its pressure and density (in this case we call it a two-way-coupled run). Since the two-way coupled code is currently undergoing testing, the simulation presented here, in which a high resolution MHD grid is used, the feedback is turned off, i.e. the MHD code only sends its information to the RCM and there is no feedback to the MHD.

2.2.4 Simulation Setup

For the results presented here, all MHD parameters are set as in *Raeder et al.* [2008]. The run time for the OpenGGCM and RCM was from 7:00 UT to 15:00 UT on March 23, 2007. The model inputs include the upstream solar wind and interplanetary magnetic field (IMF) which are taken from the WIND satellite at ~198R_E sunward. The solar wind and IMF are propagated ballistcally to the sunward boundary of the simulation (20.01R_E) at the prevailing solar wind speed. The orientation of the solar wind magnetic structure is taken into account by computing the normal direction of the solar wind discontinuities using the minimum variance method [*Raeder et al*, 2001]. The coupled thermosphere ionosphere model (CTIM) was used for more realistic conductance calculation. The OpenGGCM grid for this run contains 37.8 million cells and the smallest grid spacing is ~0.15R_E. The RCM grid resolution in latitude and longitude is 200 x 101. For the RCM calculation, we used 200 invariant energy channels and the *Spence and Kivelson* [1993] model for the initial setup of the plasma distribution. While there is an option to use the MHD plasma information for the RCM's initial condition, but that results in unrealistically low particle fluxes, due the unrealistically low initial particle pressure in the MHD code's inner magnetosphere. We assume a kappa distribution in converting from single fluid quantities to RCM multi-fluid information, where κ=5 was assumed for protons and κ=3 is for electrons. These kappa parameters were chosen to be in a reasonable range as discussed in *Yang et al.*, [2008] and *Christon et al.*, [1988].

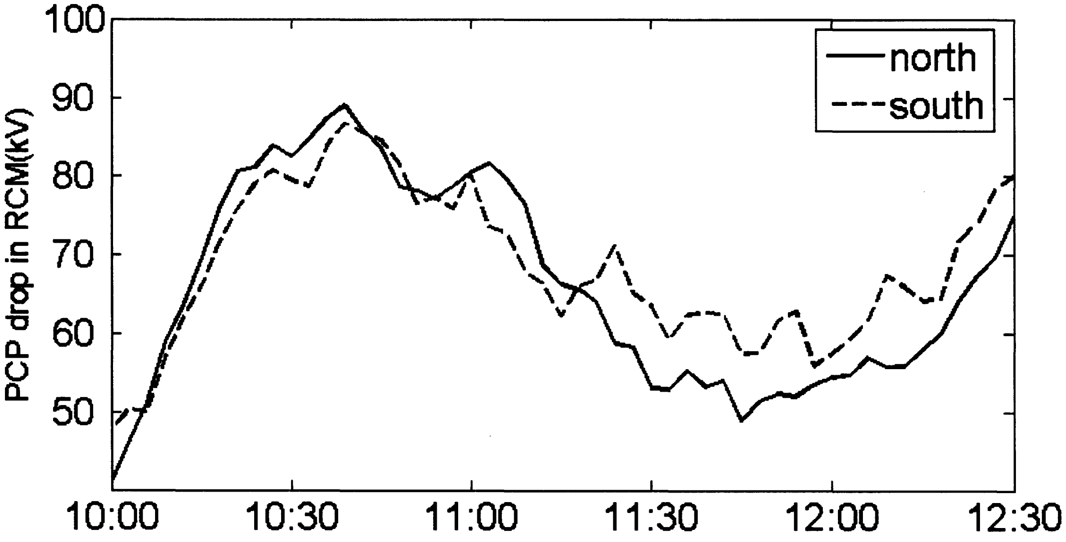

Figure 2.2 Potential drop (*kV*) at the RCM polar boundary for the northern (solid line) and southern hemisphere (dashed line).

The RCM takes magnetic field and boundary information from the OpenGGCM throughout the run except for the initial plasma condition. A comparison of magnetic field between OpenGGCM simulation and measurements by GOES11 (around 01-02 MLT during the injection) is shown in Figure 2.3. The MHD time in Figure 2.3 is in simulation UT and has not been time-shifted. Φ_{iono} in equation (3) is taken from OpenGGCM by default but the potential can be also solved by the RCM. We present results from using both ionospheric potentials. All loss mechanisms in RCM (charge exchange for ions and strong pitch angle scattering for electrons) are turned off for simplicity. Charge exchange for the ions is a relatively slow process and would have small effect on the short simulation presented here, but electron losses can be significant. As a result, in both cases the simulation should tend to overestimate particle fluxes, particularly for electrons. The number of channels (~200) and the energy invariant (λ) associated with each channel are preset before the run to ensure that the distribution function is properly resolved at the tailward boundary.

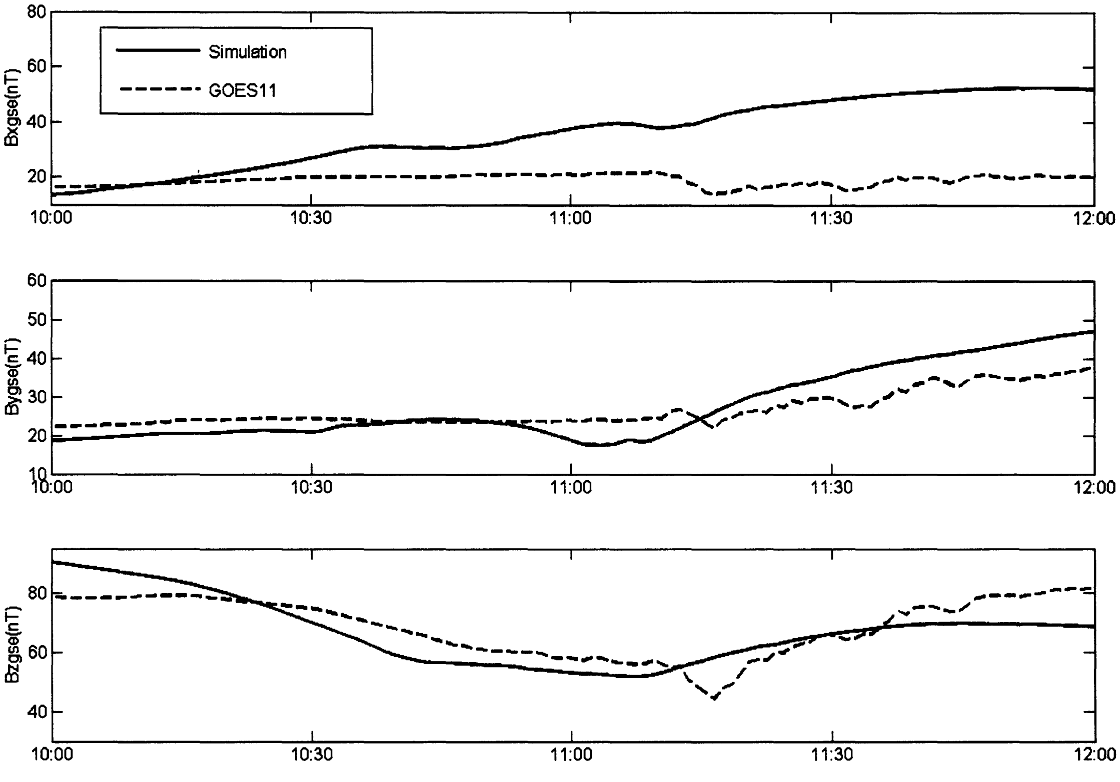

Figure 2.3 Comparison of magnetic fields measured by GOES11 (dashed line) and OpenGGCM simulation (solid line, not time-shifted) as a function of UT. GOES11 is around 01-02 MLT.

2.3 Model outputs and Results for RCM Run1

2.3.1 Bubbles

It is believed that during the expansion phase of a magnetic substorm, depleted flux tubes in the plasma sheet are formed, possibly because of reconnection or some other non-adiabatic process such as current disruption [*Zhang et al.*, 2008*; Zhang et al*, 2009; *Wolf et al.*, 2009]. These bubbles have a lower $PV^{5/3}$ than their surroundings and are interchange unstable. They tend to move earthward and sometimes are seen as BBFs (Bursty Bulk Flows) in the plasma sheet [e.g. *Angelopoulos et al.*, 1994]. These high speed flows or bubbles are thought to be one of the major mechanisms for tail flux transport and bringing plasmasheet particles near the Earth during geomagnetically active periods. Figure 2.4 shows eight RCM equatorial time series snapshots for $PV^{5/3}[\mathrm{nPa}(R_E/\mathrm{nT})^{5/3}]$ from Run1, after the "code substorm onset time" (~10:40 simulation time in the MHD [*Raeder et al.,* 2008]; we will use the simulation time in this chapter) . The Sun is to the left. The first two plots in Figure 2.4 show how the low $PV^{5/3}$ channel (yellow in color) that starts to open up in the midnight sector at simulation time ~10:45UT. In the subsequent plots, this low $PV^{5/3}$ channel expands in local time (e.g. centered in the premidnight sector between 2100LT and 0130LT as shown in the fourth plot in Figure 2.4), which is consistent with the conclusion of *Liu et al.* [2009] that the injection initiated between 2100LT and 0100LT. The leading edge of the bubble moves closer to the Earth and has a tendency to travel westward because of gradient and curvature drifts. From the time series of the contours, the potential electric field increases in the bubble region during the injection and exhibits weak shielding near the Earth. Throughout the injection, the entropy parameter of the newly injected flux tubes is ~ 0.06 (nPa(R_E/nT)$^{5/3}$); the bubble reached ~5R_E from the Earth. There are also signatures of possible interchange instability on the leading edge of the bubble, as seen by the presence of the finger-like structures in the second plot. The closure of this low $PV^{5/3}$ channel took place at ~11:45UT; by 12:00UT, the $PV^{5/3}$ configuration in the inner magnetosphere has almost returned to the pre-injection state.

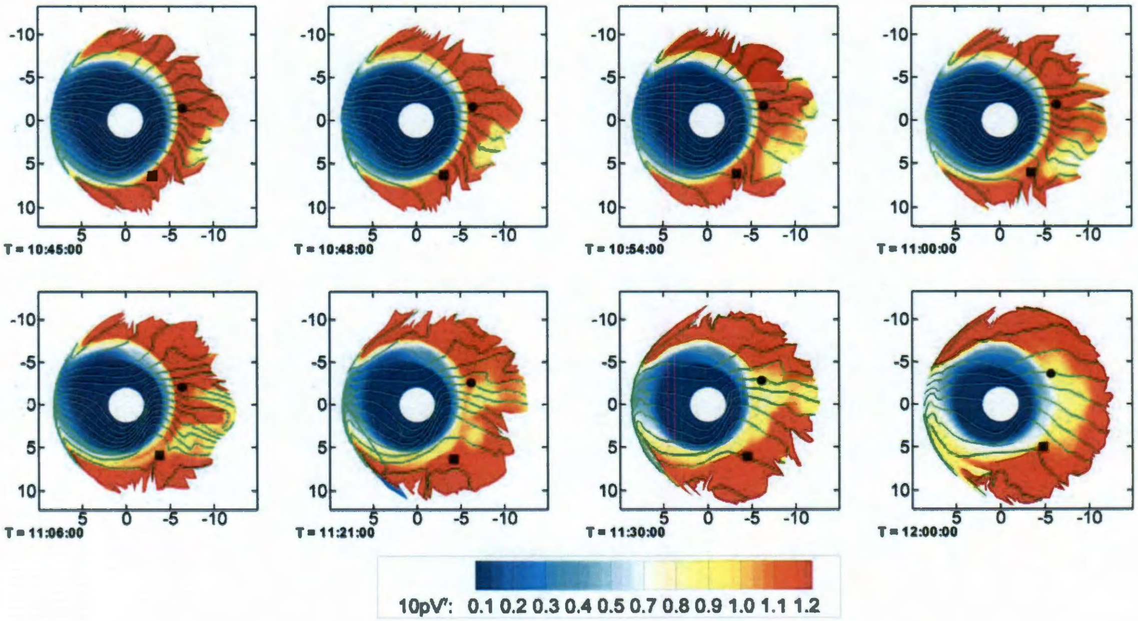

Figure 2.4 $PV^{5/3}$ [nPa(R_E/nT)$^{5/3}$] time series of the bubble injection on the RCM equatorial plane with potential solved by OpenGGCM (5kV spacing) for RCM Run1. The Sun is to the left. Locations of LANL97A (LANL89) are marked as squares (circles).

The equatorial RCM pressure from Run1 before and after the bubble injection is shown in Figure 2.5(a),(b). The pressure in the inner magnetosphere increases and the peak pressure occurs closer to Earth after the bubble injection. These features of the model produced bubble are qualitatively in agreement with the results presented in *Zhang et al.* [2008, 2009] and the picture first suggested by *Pontius and Wolf* [1990]. However, the way that the OpenGGCM imposes low $PV^{5/3}$ boundary condition seems to be different from *Zhang et al.* [2008] in which the flux tube content is reduced at the boundary, but the magnetic field is not changed correspondingly. In the OpenGGCM run, despite the slight change in particle pressure, the RCM sees rapid magnetic field dipolarization at the boundary starting at ~10:40 (at x=-9 R_E, B_z =23.9 nT at 10:45, comparing to B_z =13nT at 10:36). *Zhang et al.* [2009] include the field stretching and collapsing of the magnetic field. Thus in the MHD results as well as in *Zhang et al.* [2009], P changes relatively little, and the decrease in $PV^{5/3}$ is mostly associated with the decrease in V during the dipolarization. Figure 2.5(c) shows the OpenGGCM pressure in the equatorial plane and it is much weaker than the RCM computed pressure in (a) and (b). Examples of OpenGGCM Birkeland currents and RCM computed Birkeland currents (from Run2) are shown in Figure 2.5(d) and (e). The currents from the OpenGGCM are more diffusive and the region-2 currents are weaker. Figure 2.5(f) shows higher ion and electron temperature in the injection region for Run1.

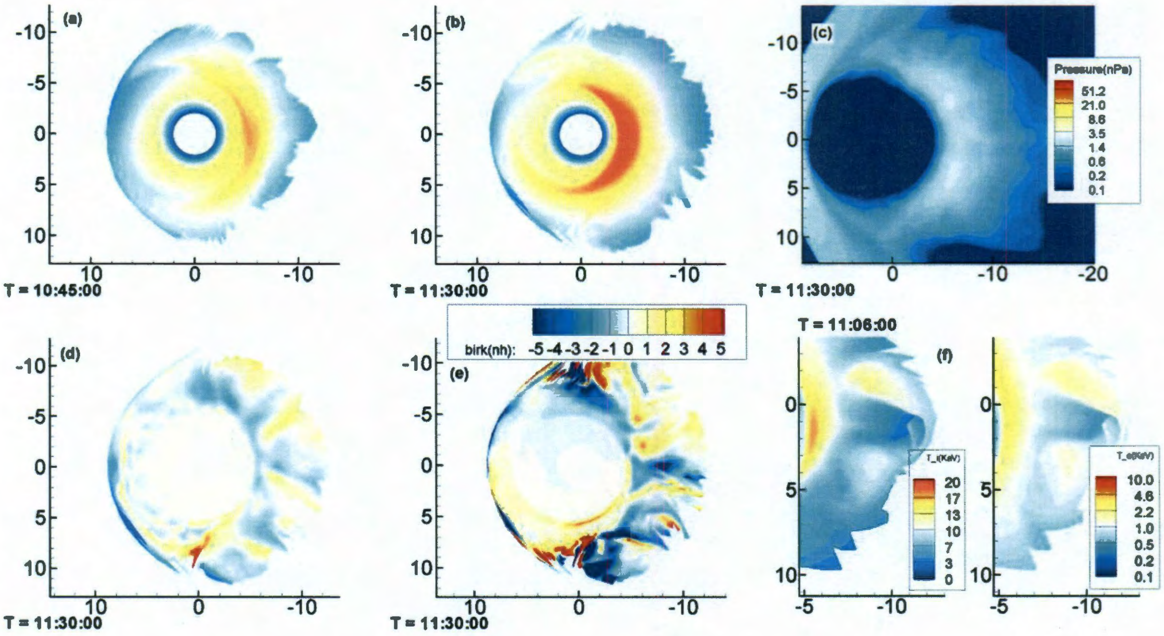

Figure 2.5 (a) & (b) RCM pressure on the equatorial plane before and after the onset from Run1. (c) OpenGGCM (the third) pressure on the equatorial plane after onset. (d) & (e) Comparison of equatorial maps of ionospheric Birkeland currents computed by OpenGGCM (d) and the RCM from Run2 (e). (f) RCM ion and electron temperatures (*keV*) in the equatorial plane from Run1.

2.3.2 Bubble creation in the OpenGGCM

To provide a closer look at how these bubbles are created in the MHD code, Figure 2.6 shows the entropy parameter $PV^{5/3}$ in the equatorial plane in the MHD domain along with the field line shape and the velocity in the noon-midnight meridian, for three different times: 10:30UT, 10:42UT and 11:01UT. The first three rows are plasma pressure with field lines and flow velocity in x direction in the noon-midnight-meridian plane, with the Sun to the right. The last row presents the field line averaged quantity $PV^{5/3}$ $=(\int_{s}^{n} P^{3/5}\frac{ds}{B})^{5/3}$, plotted on the magnetic equatorial plane, with the Sun to the left. Since $PV^{5/3}$ is a field line averaged quantity, points not on closed field lines are not shown. The fieldline tracing was stopped at the ~4R_E inner shell because inside the inner boundary the MHD field is assumed to be dipolar and is constant with time.

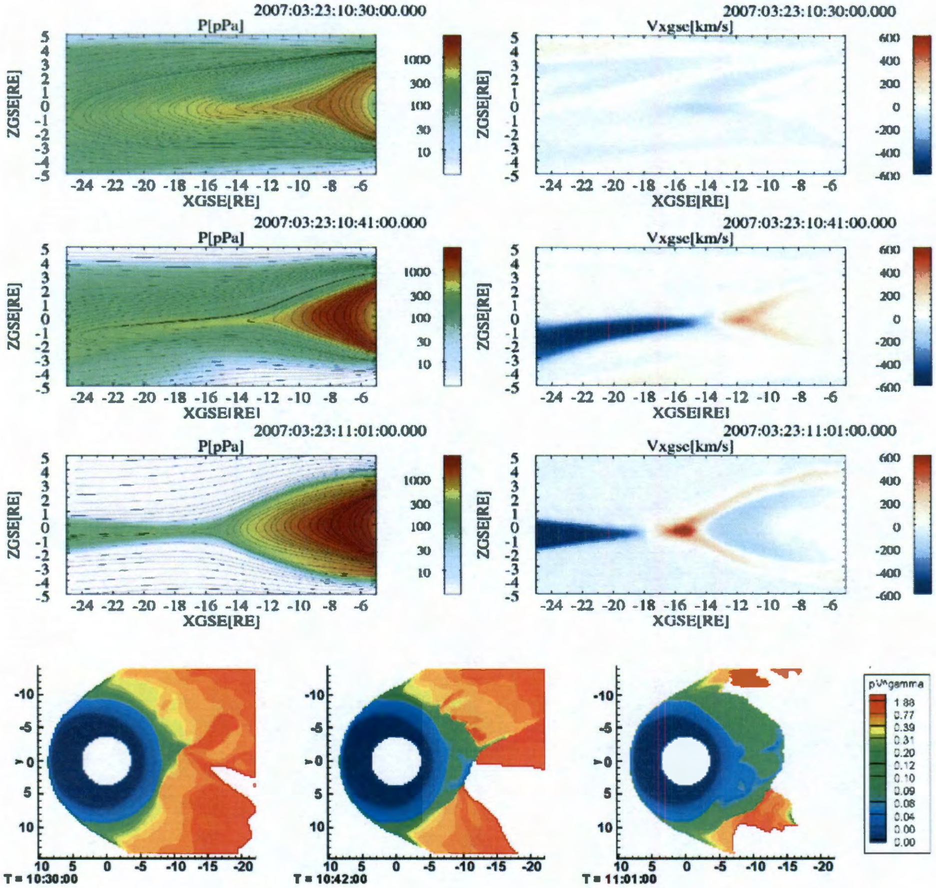

Figure 2.6 The first three rows are midnight-meridian plane cut for OpenGGCM pressure with magnetic field line topology and velocity in the GSE x direction with the Sun to the right. The last row is $PV^{5/3}$ on the equatorial plane with the Sun to the left (There are no $PV^{5/3}$ values in the white region due to field line traces not being closed). Columns are for UT 10:30, 10:42 and 11:01.

At 10:30UT, which is near the end of the substorm growth phase, the field lines are quite stretched and there are no noticeable earthward flows. Most of the plasmasheet points are on closed field lines, though there is a patch of open field lines towards the dusk side of midnight; they show up as blank in the equatorial plane. Post-midnight, there is a pair of high/low $PV^{5/3}$ flux tubes and we will discuss this in the next paragraph. The MHD code onset time is about 10:42UT [*Raeder et al.*, 2008], when earthward flows are seen in the ~13R_E region, associated with the field dipolarization. (Actual substorm onset occurred 30 minutes later.) A bubble emerges from the reconnection site, which is duskward of the local midnight, and moves earthward at an MHD-estimated speed of ~160Km/s. At around the same time, the RCM sees a depleted $PV^{5/3}$ channel opening at its tailward boundary (~10R_E). The third column of the $PV^{5/3}$ plots shows time 11:01UT, by which time the reconnection that powers the major activation of the substorm, occurs over a wide range of local times resulting strong earthward and tailward flow. One can also see this from the field topology; the X-line is at ~17R_E at local midnight. Magnetic field lines are quite dipolarized earthward of the X-line, and the current sheet is thinning on the tailward side. The $PV^{5/3}$ figure for 11:01UT shows that depleted flux tubes are formed and bubbles rapidly move earthward with an MHD-estimated speed of ~200Km/s. These bubbles are emerging from the X-line and they gradually slow down as they travel closer to the Earth into the RCM modeling region. In fact, reconnection at ~20R_E, which results in consistent earthward flows, lasts until ~11:30; during the expansion phase, the reconnection site moves more tailward.

In the substorm growth phase (~10:22), at ~11 R_E towards the dawn side of local midnight, a local maximum in $PV^{5/3}$ *(blob)* appears next to a minimum in $PV^{5/3}$ (bubble), Figure 2.7 shows the $PV^{5/3}$ on the equatorial plane and the OpenGGCM flow velocity in X direction, for UT 10:22, 10:25 and 10:28. The anomalous resistivity as computed by the OpenGGCM is shown as black spots in the $PV^{5/3}$ figures with the Sun to the left. From the first row, the blob is seen at ~10:22; it moves anti-sunward and is associated with patches of anomalous resistivity. The anomalous resistivity is determined by local current and it must reach certain threshold before switched on thus it is nonzero for only a few grid points in strong current sheets [*Raeder et al.* 1998]. From the results, the blob forms while the anomalous resistivity is zero, so its formation is possibly due to numerical resistivity. The OpenGGCM flow plots in Figure 2.7 show both the earthward flow of the bubble and the anti-sunward motion of the blob, which accelerates as it travels tailward. This weak bubble moves earthward but it does not propagate deep into the inner magnetosphere. The separation of the bubble and the blob could create a more favorable magnetospheric configuration for further instabilities such as magnetic reconnection to occur. Thus the interchange instability resulted from the bubble/blob pair may have important implications for the substorm expansion phase, though careful further study is needed to confirm this simulation result.

Overall, the majority of bubbles that propagate into the RCM modeling region during the substorm expansion phase are caused by magnetic reconnection in the tail which powers the main activation of the substorm. There are multiple reconnection sites during this event and bubbles created at different locations tend to have different properties. The field is quite dynamic during the substorm expansion phase and more investigations are needed to fully understand the onset mechanism in this event.

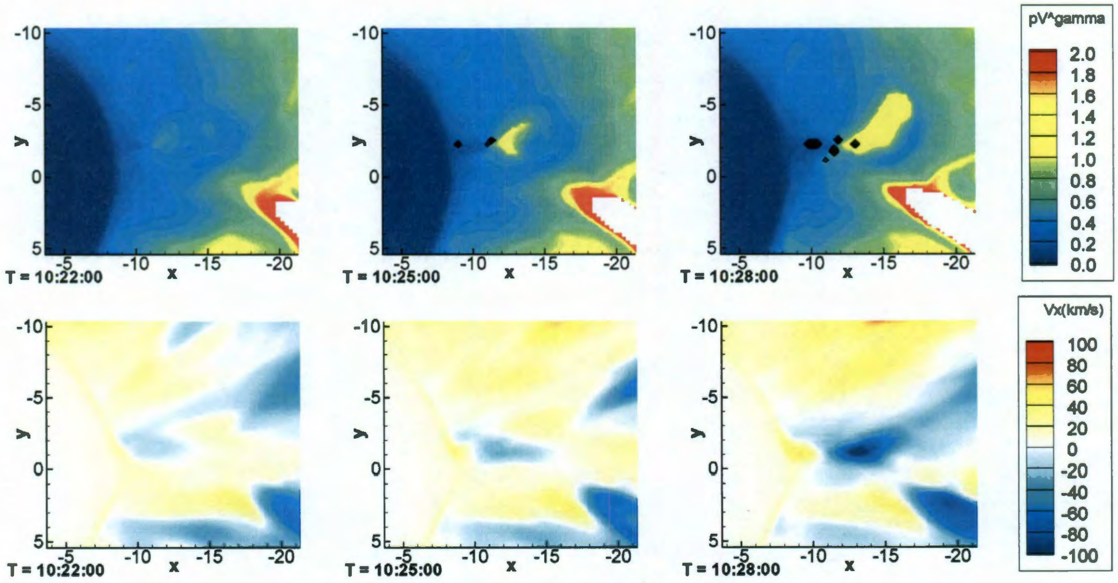

Figure 2.7 $PV^{5/3}$ and OpenGGCM flow velocity in GSE X direction on the RCM equatorial plane, for UT 10:22, 10:25 and 10:28. The black spots on $PV^{5/3}$ plots indicate where the anomalous resistivity in the OpenGGCM is non-zero.

2.3.3 LANL Energetic particle flux and MPA measurements

In this section, we compare our model produced particle flux with two LANL satellites LANL89-046 and LANL97A at geosynchronous orbit, where an increase in high energy particle flux is often observed during a substorm expansion phase. The energization of these particles is often attributed to induced, impulsive electric fields possibly associated with field dipolarization. There is evidence that earthward moving bubbles are also associated with a substorm injection [e.g. *Lyons et al.*, 2003].

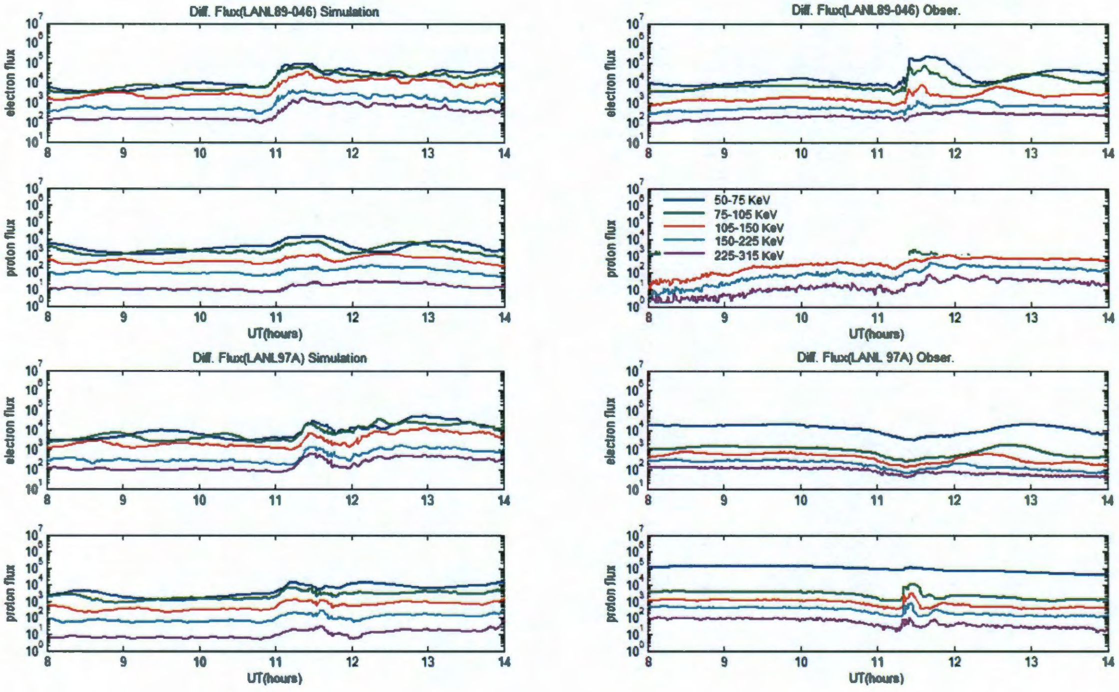

Figure 2.8 Simulated SOPA fluxes (left column) vs. observations (right column) for satellite LANL89-064 and LANL97A for RCM Run1. The energies are 50–75, 75–105, 105–150, 150–225 and 225-315keV from blue to purple. The simulation results have been time-shifted 30 minutes.

At substorm onset, LANL89-046 satellite was located near local midnight and LANL97A near 2100LT. Figure 2.8 shows comparisons for RCM Run1 between the energetic particle differential flux ($/cm^2/s/sr/keV$) measured by SOPA instruments on LANL89-046 and LANL97A and the simulation outputs. Since the OpenGGCM onset time is ~10:40UT, earlier than the actual onset times (~11:00UT and 11:19UT), we time-shifted the simulation 30 minutes for easier comparison with observations. The discrepancy in onset time may be due to the preconditioning in the MHD code. In this run, the MHD code started 4 hours before the actual event which may not be long enough to remove any remnants of the initial condition used to start the MHD code [*Raeder et al.*, 2008]. Other effects such as insufficient resolution in the MHD code, and missing physics such as kinetic effects and feedback from an inner magnetosphere model such as the RCM may also play a role in the timing of substorm onset. For the post midnight satellite LANL89-046, a major dispersionless electron injection is observed along with an increase in proton fluxes that exhibits a slight dispersion. The simulation results for LANL89-046 basically reproduce the dispersionless electron injection, and the ion flux is also roughly in agreement with observations.

For the pre-midnight satellite LANL97A, an ion injection with small dispersion is observed and this is consistent with the slightly dispersed injection in the observations. The electron fluxes in the simulation show an increase which is different from the observations, partly because the satellite is close to the RCM dusk side tailward boundary and the westward electric field there draws particles at the boundary towards the Earth to 6.6R$_E$. Since LANL89-046 is inside the injected bubble at the time of code onset, one would expect it to see dispersionless flux increases from both electrons and ions. LANL97A is outside the simulated bubble region, and it does not see the newly injected particles directly but sees them after they gradient and curvature drift around to the satellite; thus it observes dispersional proton injection. The injection picture we infer from the simulation is generally consistent with the analysis in *Liu et al.* [2009], except that we also see a dispersionless ion flux increase since our injection boundary is wider in local time compared to their conclusion. The dispersionless electron injection in our simulation has a ramp-up time in the order of ~10minutes, while the injection in the observation is faster (a few minutes). That difference may be partially due to the fact that the earthward flow in the MHD is slower than what was observed. The observation at THEMIS C (closest to tail center at X~-7R$_E$) indicates earthward flow as high as 300*km/s*, while the MHD earthward flow velocity is ~100*km/s* at ~-9R$_E$ around the code onset time (Figure 2.6).

Figure 2.9 compares the simulation results from Run1 with the observed MPA moments, specifically the partial density and partial pressure in the energy range for the two LANL satellites. The left column in Figure 2.9 is the simulation results and the right column is the observational data. LANL MPA instruments measure the charged particle distribution from 1eV to ~40keV, while the corresponding RCM quantity is obtained by summing the energy channels within the measurement range. The partial pressure for the measurement is calculated by summing the partial pressure for the high energy protons (0.13-45keV) and the pressure for the electrons. Though there are unfortunate gaps where observations were not available, overall, the simulation captures the trend of the density and pressure variation. However, the RCM tends to over-estimate the density. This is partly due to the higher density at the inner edge of the plasmasheet resulting from the boundary condition that was imposed on RCM before the dipolarization. In addition, the RCM pressure is higher than the observations and this and the higher densities may be due to the fact that the magnetic field is not responding to the RCM pressures, since feedback to the MHD code is not turned on. In simulations with self-consistent magnetic fields, the pressure in the inner magnetosphere tends to be lower than in simulations with non-self-consistent magnetic field [*Zaharia*, 2005]. Pressure is lower in two-way-coupled OpenGGCM/RCM runs than in the standalone RCM. These results do suggest the importance of a self-consistent magnetic field in matching observations.

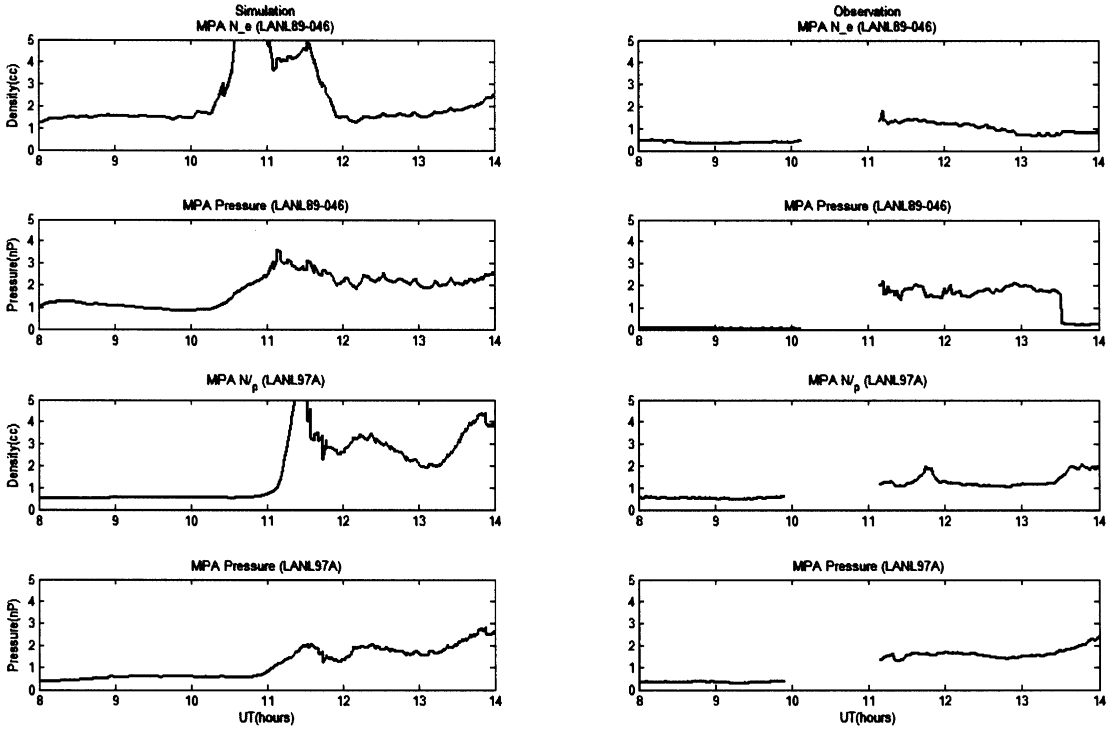

Figure 2.9 Top two rows are MPA moments for simulation (left column) vs. observations (right column) for satellite LANL89-064 from RCM Run1. Bottom two rows show MPA moments for simulation (left column) vs. observations (right column) for satellite LANL97A from RCM Run1. The simulation results have been time-shifted 30 minutes.

The overall reasonable agreement between simulation and data confirms the association of substorm injections with earthward moving bubbles. It also demonstrates that the OpenGGCM model, when coupled with the RCM, can be used to simulate substorm injection events, although feedback to the magnetic field could be important.

2.4. Results using the RCM computed electric field (RCM Run2)

2.4.1 Differences between MHD- and RCM-computed electric fields

In this section, we present results from a run in which the potential electric field was computed using RCM rather than MHD machinery. There are several major differences in the procedure:

(i) The two procedures calculate Birkeland currents in profoundly different ways. OpenGGCM calculates $\hat{b}\cdot\nabla\times\mathbf{B}$ on a spherical surface at ~4 R$_E$ and then maps the currents to the Earth's surface assuming dipole field lines. The RCM uses a completely different approach, based on the current conservation equation written in the form

$$\frac{J_{\parallel i}}{B_i} = -\int \nabla\cdot\mathbf{J}_\perp \frac{ds}{B} \tag{2.4}$$

The two approaches are both based on MHD and are equivalent, in principle, provided that inertial currents are unimportant. However, the OpenGGCM usually do not have enough grid points near 4.5 RE to resolve the complex auroral Birkeland currents.

(ii) The MHD code includes inertial currents in its calculation of $\mathbf{J}_\perp$, while the RCM neglects those currents entirely and assumes that $\mathbf{J}_\perp = \mathbf{B}\times\nabla P / B^2$. (Substituting this in (4) gives Vasyliunas equation $J_\parallel = \hat{b}\cdot\nabla V\times\nabla P/2$, after some manipulation).

The RCM's neglect of inertial currents constitutes a fundamental problem in using the code to treat fast-moving bubbles. As noted in section 2.2, use of the RCM is usually limited to subsonic flow regions and precludes representation of waves. The run presented here that uses the MHD-calculated ionospheric potential includes inertial currents, but it has numerical difficulties, as described in items (i), (iii), and (iv). We are still working to find a procedure that includes the effects of inertial currents without the numerical problems inherent in the MHD code.

(iii) The MHD code sets Birkeland currents equal to zero for field lines with $L<\sim 4$.

(iv) Figure 2.5 makes it clear that the RCM- and MHD-computed pressure distributions, which strongly affect the Birkeland currents, are very different. There are several reasons for this:

(a) The RCM initial condition includes a realistic trapped particle population near the Earth, while the MHD initial condition does not. Consequently, the RCM pressures are higher near the Earth.

(b) The MHD code does not include transport by gradient/curvature drift, which is important in the inner plasma sheet and ring current.

(c) There is much more numerical diffusion in the MHD code than in the RCM, and it tends to diffuse plasma outwards from the high-pressure near-Earth region.

In the two-way coupled case, MHD pressures are forced to be approximately consistent with RCM values, but that is not true in the present one-way-coupled code used here. Considering all of the differences between the two approaches for computing $J_{\parallel}$, one might expect them to give different results, and they do. The MHD-computed Birkeland currents shown in Figure 2.5 are indeed very different from the RCM results.

(v) Both codes use routines for solving $\nabla \cdot \Sigma \cdot \nabla\Phi = -j_{\|} \sin I$ on a 2D spherical grid; the RCM grid is denser than the OpenGGCM ionospheric grid but covers less latitude. The two have the same potential on the high-latitude boundary of the RCM, because the RCM takes its boundary condition there from MHD. However, the low-latitude boundary conditions for the potential solvers are different and are applied at different locations (45° latitude for RCM, 0° for MHD). Since the mapping originates from a spherical shell around the Earth at ~ 3.5R_E, the MHD electric field solution below ~58° is artificial. The conductances are the same, as the OpenGGCM conductance model is used in both cases.

2.4.2 Bubble

Figure 2.10 shows four snapshots of the entropy parameter $PV^{5/3}$ and the potential for the run using the RCM potential solver (Run2); it should be compared to results shown in Figures 2.4 for Run1, which used the MHD potentials. The bubble injection process in this run is quite similar in the two runs. For example, the low $PV^{5/3}$ channel opens and closed at around the same times as in the run with OpenGGCM potential, which is due to the OpenGGCM magnetic field and plasma boundary conditions. Both runs show enhanced westward electric field inside the bubble. However, the electric field in the bubble is stronger in the run using RCM potential and the bubbles travel slightly faster (e.g. by comparing plots at UT 11:21 and 12:00). The difference is probably due to a combination of factors (i), (ii), and (iv) in Section 4.1. Figure 2.11 shows the mapped equatorial time series plots for the ionospheric Birkeland currents with potential contours. From the time series of the contours, the potential electric field increases in the bubble region during the injection and exhibits weak shielding near the Earth, although the region-2 Birkeland currents are well-defined. The leading edge of the bubble caused a misalignment of the gradient of $PV^{5/3}$ and the gradient of the flux tube volume. Thus according to the Vasyliunas equation [*Wolf*, 1983] a wedge-like current is generated in the RCM around midnight. After the injection these currents become weaker. The two runs also give similar SOPA predictions; Figure 2.12 shows the geosynchronous SOPA fluxes for the case using RCM computed electric field and they are very similar to the results using the OpenGGCM potential(Figure 2.8). Figure 2.13 compares observational data with model-computed plasma moments, for the run using the RCM electric field, and they are also similar to the results using the OpenGGCM potential (Figure 2.9) except that pressure and density values obtained in this run are closer to observations.

The differences between the two electric fields are greatest in the near Earth region. The MHD-based potential from Run1 shown in Figure 2.4 exhibits little or no shielding in the inner magnetosphere while in the same region the RCM potential from Run2 in Figure 2.10 shows significant shielding of the cross tail potential. The weaker region-2 currents computed by the MHD may be due to the limited resolution for computing currents in the inner magnetosphere.

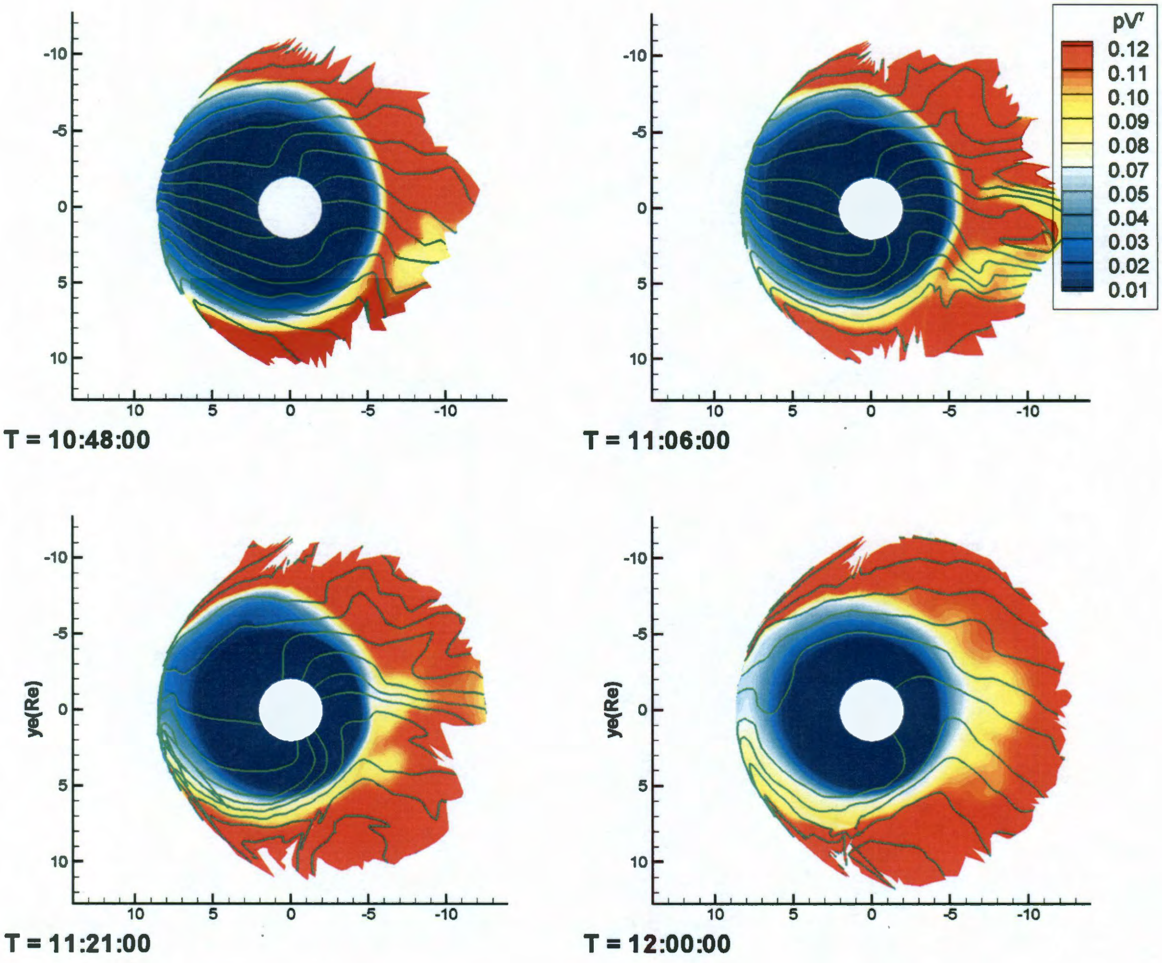

T = 10:48:00

T = 11:06:00

T = 11:21:00

T = 12:00:00

Figure 2.10 $PV^{5/3}$ time series plot of the bubble injection on the equatorial plane for the run using RCM potential solver (Run2). Solid lines are ionospheric potential with a spacing of $5kV$.

The bubble injections are quite similar in the two runs, due to the fact that the bubbles were injected partly by the induction electric fields (same in both runs) and partly because the potential electric field in the bubble differs only moderately in the two runs. The RCM generally produces a more realistic electric field distribution, particularly because it exhibits significant shielding and other known features. Some implications of that difference will be explored in the next sub-section.

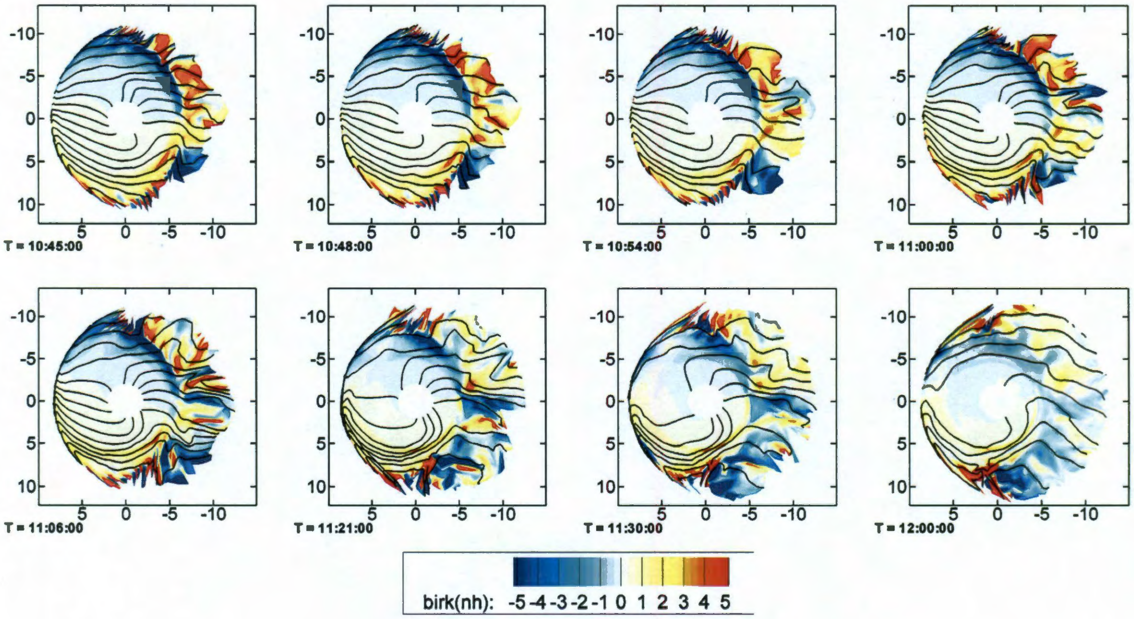

Figure 2.11 Birkeland currents in $\mu A/m^2$ (color) and potential (contours) for the run using the RCM electric field (Run2). Positive Birkeland currents (yellow-red) are down into the ionosphere, while negative currents (blue) are up from the ionosphere. The current densities are ionospheric values mapped to the equatorial plane.

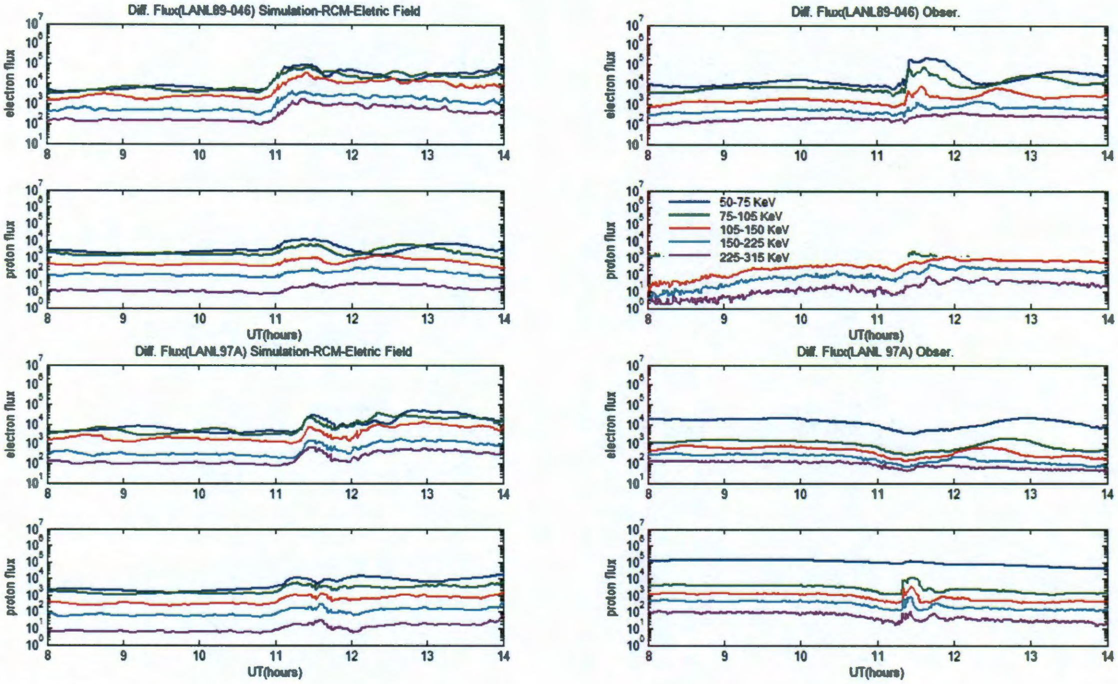

Figure 2.12 Simulation of SOPA fluxes vs. observations for satellite LANL97A and LANL89-064, using the RCM electric field (Run2). The energies are 50–75, 75–105, 105–150, 150–225 and 225-315keV from blue to purple. The simulation results have been time-shifted 30 minutes.

2.4.3 Plasmasphere plume after bubble injection

The plasmasphere contains particles of mostly ionospheric origin with energy around 1 eV. The motion of these cold particles is determined by the electric field, including the effect of the Earth's rotation. The plasmasphere can have significant structure; such as the plasmaspheric plume, which is thought to form during enhanced magnetosphere convection [e.g. *Pierrard et al.*, 2009]. To simulate the plasmasphere in the RCM, we set the lowest energy channel with density values from *Gallagher* [2000] model as an initial condition. This low energy channel has a very low invariant energy so it carries a large density but an insignificant total pressure. This approach neglects the long-term effects such as refilling and night side losses, but the effects of these are limited due to the short runs.

Figure 2.14 shows snapshots of the plasmaspheric density from Run2 for three times, one before the arrival of the bubbles, one during the bubble injection and one just after. The potential lines on these plots are ionospheric potential with corotation and thus are approximately the instantaneous drift paths for this low energy channel, aside from the effects of induction electric fields, which are modest in the inner magnetosphere. Figure 2.15 shows the equatorial potential electric field comparison between Run1 (top-row left) and Run2 (top-row right). RCM Birkeland currents on the ionosphere in the run using RCM potential (Run2) and the OpenGGCM field-aligned currents on the ionosphere (bottom-row middle) are also compared in Figure 2.15. The RCM electric field computed self-consistently with the plasma shows an enhanced electric field in the dusk and midnight sector (~5-6R_E) after the bubble injection. These strong electric fields near the dusk side of the plasmapause, usually called SubAuroral Ionization Drift (SAID) events [*Spiro et al.*, 1979], cause particles in the plasmasphere to $\vec{E} \times \vec{B}$ drift westward and then sunward, and eventually creating a plasmaspheric plume [*Goldstein et al.*, 2005]. The polar cap potential drop in the RCM modeling region decreases from ~80kV to ~ 50kV (shown in Figure 2.2) during the injection, and shielding appears. If viewed on the ionosphere, the downward region-2 currents in the dusk-midnight sector move equatorward into the lower conductance region and thus strong electric field is produced [Southwood and Wolf, 1978]. Since the OpenGGCM does not resolve the Birkeland currents at this region, the electric field it obtains does not show this feature in the inner magnetosphere. There is a region near the Earth with strong electric field from OpenGGCM (Run1) after the onset as seen in Figure 2.15. Since this region is inside the OpenGGCM inner boundary, the strong electric field could be an artifact of the low conductance and the weak region-2 currents (shown in Figure 2.15). The spotty structures shown in OpenGGCM computed Birkeland currents, although are consistent with many observations [e.g. *Iijima and Potemra, 1976, Sitnov et al.*, 2010] will be further investigated in future studies. Unfortunately there are no available observations at the event time to confirm the existence of a plasmaspheric plume in this event, but the results indicate the need to use RCM self-consistent electric field to more accurately model the inner magnetosphere electric field.

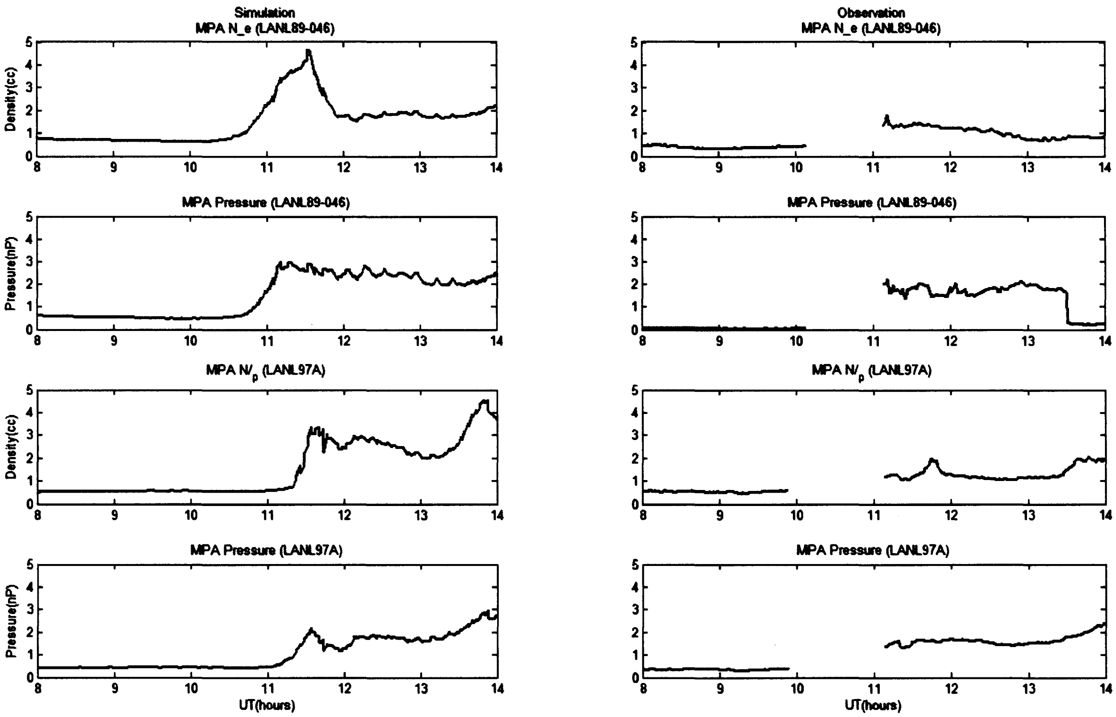

Figure 2.13 The same as Figure 2.8 but for the run using the RCM electric field (RCM Run2).

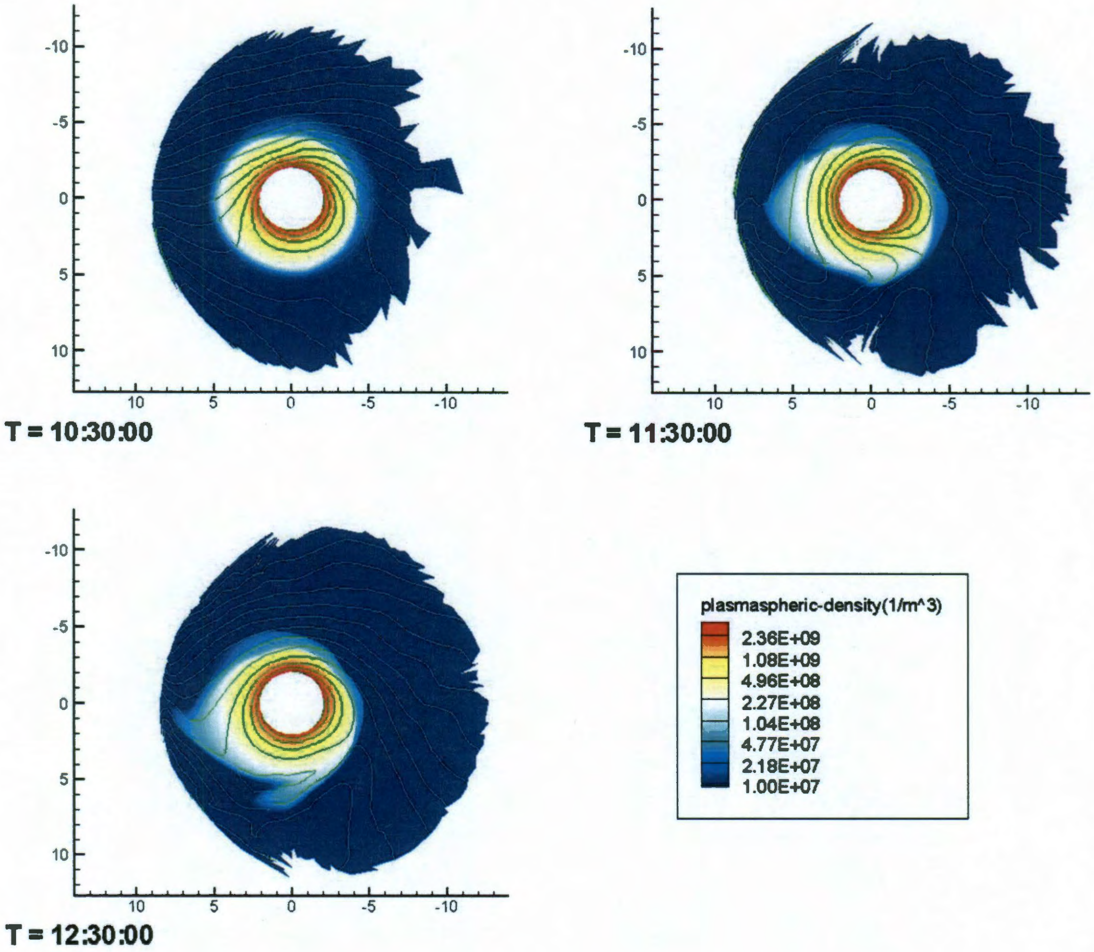

Figure 2.14 Plasmaspheric density on the equatorial plane, before, during and after the bubble injection for RCM Run2. Solid lines are the potential (including corotation).

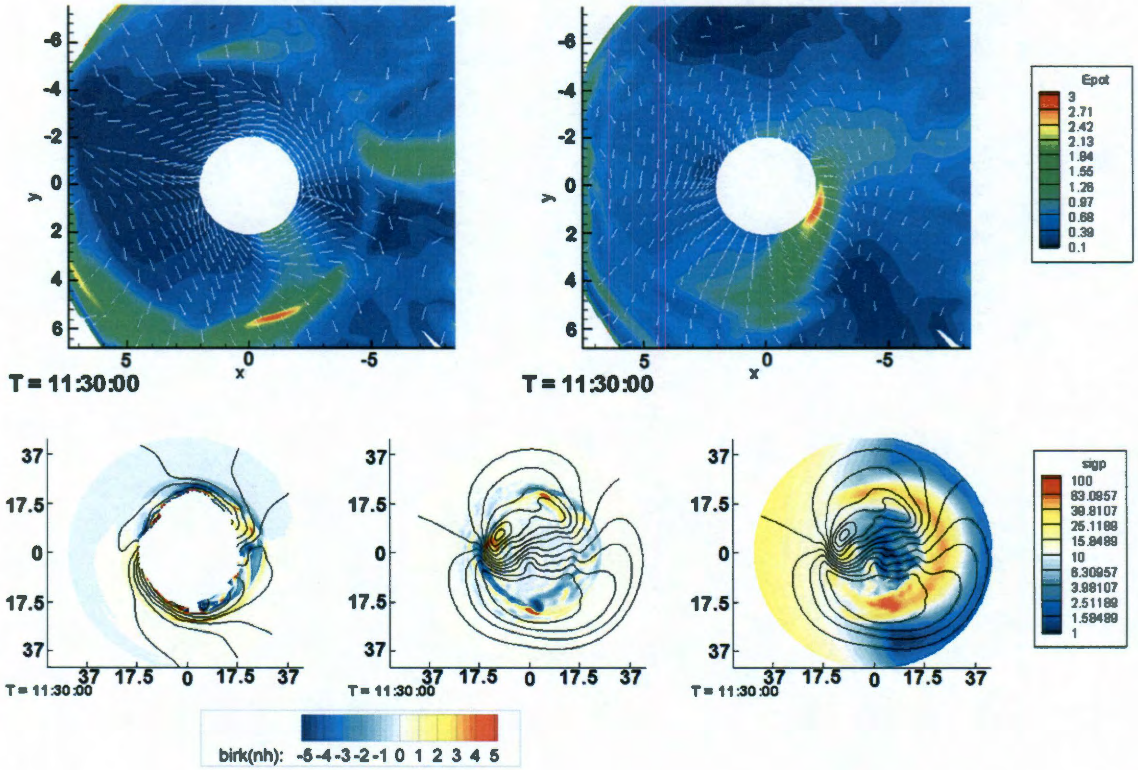

Figure 2.15 Equatorial potential electric field (mV/m) comparison between the RCM potential from Run2 (top-row left) and the OpenGGCM potential from Run1 (top-row right). Contours are electric field strength and the vectors show the direction. RCM Birkeland currents ($\mu A/m^2$) from Run2 are shown in the ionosphere in solid lines with a spacing of 5kV (bottom-row left). OpenGGCM field-aligned currents ($\mu A/m^2$) in the ionosphere with OpenGGCM computed potential in solid lines with a spacing of 5kV (bottom-row middle). The Pedersen conductance (*S*) in the ionosphere is shown on bottom-row right with OpenGGCM computed potential. The Sun is to the left. All ionospheric parameters shown are for northern hemisphere.

2.5 Discussion and Conclusions for Chapter 2

A one-way coupled OpenGGCM and RCM simulation was carried out to investigate a substorm event on March 23, 2007. It is the first time that a coupled MHD-RCM code has been used to simulate a substorm injection event, picturing the injection process in terms of earthward moving bubbles. In this simulation, the OpenGGCM magnetic field and plasma information are used as input and boundary conditions to the RCM, assuming the OpenGGCM provides reasonably good magnetic field, although feedback of the RCM pressures and densities will likely change the magnetic field in the inner magnetosphere and have some impact on the results at geosynchronous orbit. In addition, a quiet time ring current model is used as the RCM initial condition. We found bubbles to be injected into the inner magnetosphere during the substorm expansion phase and the associated geosynchronous energetic particle injection. The bubble injection picture is consistent with other recent modeling work which uses different methods to drive the RCM. In the earlier simulations (e.g., *Yang et al.* [2008] and *Zhang et al.* [2008, 2009]), bubbles were produced by assuming low-$PV^{5/3}$ on part or all of the RCM tailward boundary; in the present case, the bubbles were produced by the MHD calculation itself.

To gain insight into how the MHD code created bubbles, we looked at the entropy parameter $PV^{5/3}$ in the OpenGGCM and found that the major injected bubbles were from magnetic reconnection in the MHD code. Multiple reconnection sites at different local times and distances were observed and their evolution through time was found to be complicated. There were signs of violation of ideal MHD before the code onset near ~11R_E on the night side, probably because of numerical diffusion. The simulation indicates that in a real event, the bubble creation and propagation could be more complicated than the simplified 2D picture. I will describe further study on violation of ideal MHD frozen-in-flux condition in Chapter 5. The MHD calculation suggests that the processes are much more complex and dynamic than was represented by the simple ad hoc boundary conditions assumed in the earlier calculations [*Yang et al.*, 2008; *Zhang et al.*, 2008, 2009].

We compare the RCM energetic particle flux with data measured by the SOPA and plasma moments with MPA data on LANL-97A and LANL-89-046 satellites. The simulation results are in general consistent with observation. In our simulation, a dispersionless injection is predicted at the virtual LANL-89-046 satellite and dispersed flux increase at the LANL-97A virtual satellite. The simulation showed a qualitatively reasonable picture of the bubble injection into the inner magnetosphere during a magnetospheric substorm.

The simulation also demonstrated that by coupling an inner magnetosphere ring current model to a global MHD model, one can add missing physics to the MHD model, which cannot study processes like dispersed substorm particle injection on its own. The implication of the bubble injection found in this simulation is encouraging for the continuing development of MHD and RCM coupling, since it provides a consistent approach to non-adiabatic bubble creation and adiabatic bubble convection.

A comparison simulation in which the electric field is self-consistently solved by RCM is also presented, confirming the injection picture and suggesting the need to use RCM's electric field. The reasons why the two setups of runs gave similar bubble dynamics and fluxes are: (1) The bubble injection is a short time scale process and the inner magnetosphere on a global scale might not have enough time to respond. Although the movement of the bubble has feedback to its local electric field, it is generally not sensitive to the ionospheric feedback of the region-2 currents in such short time scale. In particular, the more energetic particles are not sensitive to the electric field. (2) The motion of the bubble largely depends on the local magnetic field (the same in two runs) and electric field (similar in the bubble region). From Figure 2.5, we can see that the current structure in the bubble-injection region is similar in the RCM and OpenGGCM cases, although the MHD currents are more diffuse, and region-2 currents are weaker. (3) Before the injection, the IMF Bz is mostly northward and the convection strength is weak from 07:00UT to 10:00UT. When the IMF turns southward at ~10:00UT, the polar cap potential starts to increase and region-2 currents start to build up. Since the RCM in Run2 use the OpenGGCM potential for its polar boundary condition, after a short time, the electric field from Run2 is similar to the electric field from Run1 at 10:45UT except for the slightly better shielding. The similar pre-injection electric field configuration contributes to the similar bubble dynamics of the two runs.

Work towards a fully coupled RCM and OpenGGCM model will be continued to achieve better magnetospheric self-consistency. In these simulations, the pressure profiles computed by OpenGGCM and RCM differ considerably in the inner magnetosphere (e.g. the pressure profile comparison shown in Figure 2.5c). Although the timescale for a substorm event is much shorter than a storm, it may still be substantially impacted by the RCM feedback to the OpenGGCM, e.g. in the growth phase of the substorm. In the next chapter, I will show how much impact the lack of pressure consistency between the RCM and the MHD has in terms of the detailed dynamics of a substorm.

Another issue that arises with the use of RCM to simulate the fast moving bubbles is the possibility of violating the RCM slow-flow assumption. The neglect of inertial currents limits the RCM to work in subsonic flow regions and precludes representation of waves. The problem could be partially addressed by adding those currents into the Vasyliunas equation and evaluation of the effects is needed. We are working to address these issues and will describe some initial results in Chapter 4.

Chapter 3

Initial results from the two-way coupled OpenGGCM/RCM

In this Chapter we will describe the other part of the coupling of the OpenGGCM global MHD code with the Rice Convection Model by presenting some initial results of the two-way coupled code. In these runs, the OpenGGCM-computed ionospheric potential, magnetic field and plasma parameters were used as inputs to the RCM (as in the forward mode). In return, the RCM returns pressure and density information back to the OpenGGCM.

3.1 Introduction

Global MHD models [e.g. *Raeder et al.*, 1998, 2001, *Lyon et al.*, 2004 *Powell et al.,* 1999, *Janhunen et al.*, 1996] are powerful tools for modeling the Earth's magnetosphere and have been applied to address many scientific questions with great success. However, in the inner magnetosphere, where the energy dependent drift physics is important, one-fluid MHD models usually produce unrealistic results partly due to the neglect of gradient/curvature drifts in the transport equation. A lot of effort has been undertaken in an attempt to add the missing physics back by coupling the MHD models to inner magnetosphere models such as the RCM [*Toffoletto et al.*, 2003] or the CRCM

(Comprehensive Ring Current Model) [*Fok et al.*, 2001]. In early efforts, the MHD only provided time-dependent magnetic field and plasma boundary condition to the RCM/CRCM where it was shown that the RCM/CRCM can produce a more realistic inner magnetosphere by using inputs from MHD models [*Toffoletto et al.*, 2004, *Moore et al.*, 2008, *Buzulukova et al.*, 2010, *Hu et al.*, 2010]. However, these one-way coupled models lack self-consistency, i.e. the MHD's solution is not changed at all by the inner magnetosphere model. To improve model consistency, two-way coupled models, where the MHD also takes input (usually density and pressure) from the inner magnetosphere models have been developed resulting in more realistic inner magnetosphere pressure and region-2 currents [*De Zeeuw et al.* 2004, *Pembroke et al.*, 2011].

The first model that had two-way coupled MHD/RCM implemented was the Space Weather Modeling Framework (SWMF) and it has been applied to idealized studies and used for extensive model/data comparisons [e.g. *De Zeeuw et al.* 2004, *Zhang et al.* 2007] with great success. This model is available on the NASA run Community Coordinated Modeling Center (CCMC) website for online runs on request. In the SWMF coupling, the RCM by default feeds back only the pressure to the global magnetosphere (GM) module (BATS-R-US) of the SWMF where BATS-R-US pressures are gently nudged to the RCM values. There is also an option to enable the density feedback [*Yiqun Yu*, private communications]. The coupling exchange interval is 10 seconds by default.

Another ongoing project has been the coupling of the Lyon-Fedder-Mobary (LFM) to the RCM. Using a nudging scheme similar to that used in the BATS-R-US/RCM coupling, the LFM's pressure and density are constantly modified towards the RCM values. In the density feedback, an additional static empirical plasmasphere model is used to cool down the inner magnetosphere. The detailed coupling approach and initial results of the LFM/RCM model are described in *Pembroke et al.*, 2011.

In this chapter, we will present initial results from the two-way coupled OpenGGCM and RCM model, where there is feedback of both pressure and density. Generally, the standalone MHD codes do not always produce the same results with similar inputs [e.g. *Raeder*, 1999, *Gombosi et al.*, 2000, *Raeder*, 2000] and the MHD/RCM coupled models usually produce even more pronounced differences in the results. Some of the results are difficult to interpret due to the feedback of the coupling between models. The addition of our results from OpenGGCM/RCM coupling projects may help improve our understanding on how a more comprehensive magnetosphere model can be built. We should note here that this and other the coupling efforts are still ongoing and the results in this chapter should be treated with caution. We will describe in Section 3.2 the model descriptions and scheme for the coupling. In section 3.3, we will present idealized runs to show the effect of RCM's feedback to the OpenGGCM. In addition, initial results from a substorm event simulation using the two-way coupled code are shown in Section 3.4. Section 3.5 and 3.6 will be a discussion and summary.

3.2 Model descriptions and setup

In this section we will briefly introduce the coupled model. We refer the reader to the description of the OpenGGCM and RCM as well as the forward coupling method to *Raeder et al.*, 2001 and *Hu et al.* 2010 (Chapter 2). Note that, in addition to the original method describe in *Hu et al.*, 2010 for determining the RCM's outer boundary, a plasma beta based boundary determination method has been added to the model as an option. The plasma beta based boundary condition limits the RCM modeling region to where the plasma beta, defined as the ratio of field-line averaged pressure and equatorial magnetic energy density, is less than a certain specified threshold. This boundary choice is designed to restrain the RCM modeling region to approximately where the slow-flow assumption is valid.

For the feedback, we have used a similar approach as described in *De Zeeuw et al.* 2004 and *Pembroke et al.*, 2011. After the RCM has run for a specified time, the density and pressure are returned by tracing field lines from each of the MHD grid points to the RCM's ionospheric grid, using the assumption that pressure and density are constant along field lines. This fieldline tracer used for feedback has been parallelized to speed up the process. The corrections from the RCM then act as source terms to the MHD mass and energy equations while keeping the momentum unchanged (OpenGGCM tracks mass, momentum and fluid energy; thus changes in mass while keeping momentum unchanged effectively result in velocity changes):

$$\rho^{MHD\_new} = s \cdot \rho^{RCM} + (1-s)\rho^{MHD} \qquad (3.1),$$

$$e^{MHD\_new} = e^{MHD} + s \cdot (p^{RCM} - p^{MHD})/(\gamma - 1) \qquad (3.2),$$

$$s = \alpha * dt / T \qquad (3.3),$$

in which ρ is the fluid mass density, e is the fluid energy density, p is the plasma pressure, T is the data exchange interval and dt is the OpenGGCM timestep. α is a factor to control the nudging rate. If α is 1, then the MHD pressure is nudged towards the RCM pressure in one exchange interval. An α less than 1 helps to improve code stability. For the runs presented in this chapter, α is set to 0.8, which is the same as what was used in OpenGGCM/CRCM coupling.

Usually there is a preconditioning period before the OpenGGCM's first coupling call to the RCM; this allows the OpenGGCM to form a magnetosphere starting from a dipole field [*Raeder et al.*, 2001]. For the runs presented here, we ran the OpenGGCM for two hours of southward IMF, after which the RCM takes its initial plasma condition from the OpenGGCM. We also have an option to use an empirical plasmasphere model [*Gallagher et al.* 2004] to modify RCM computed density before it is fed back to the OpenGGCM. This essentially reduced the fast mode speed in the very near Earth region and helps improve code stability. For the coupled runs presented in this chapter, only 1/100th of the density from the plasmasphere model is added to the RCM density. The added density corresponds to ~20 particles per cc at the MHD inner boundary, similar to the inner boundary density value reported by *Toth et al.*, [2011].

3.3 Response of the RCM coupling to the OpenGGCM – idealized runs

To illustrate the effect of the RCM coupling on the OpenGGCM, two idealized runs are presented in this chapter. In these runs, the upstream solar wind was held steady with 400km/s x velocity, 5 particles/cm^2 density and 0.016 nPa pressure. The interplanetary magnetic field only had a z component with $|Bz|$ = 5 nT which was alternated from southward to northward every 2 hours. The ionospheric Pedersen conductance was set to a uniform 10 Siemens for simplicity and the Hall conductance was set to zero. The MHD inner boundary for these runs was set to 2.5 R_E to keep away from the ring current peak which is typically at around 4 R_E. The grid resolution for OpenGGCM is 210x120x120 in x, y, z direction for these idealized runs. For the RCM, the electron losses were turned on and the ion losses were turned off. In these coupled runs, RCM used the plasma beta based boundary condition with a beta threshold set to 1. Other RCM outer boundary choices tend to produce fast tailward flows in the near Earth region. Figure 3.1 shows the solar wind input for the idealized runs. The IMF in the first two hours (0:00 to 2:00) is -5 nT for preconditioning when the OpenGGCM runs standalone for both runs.

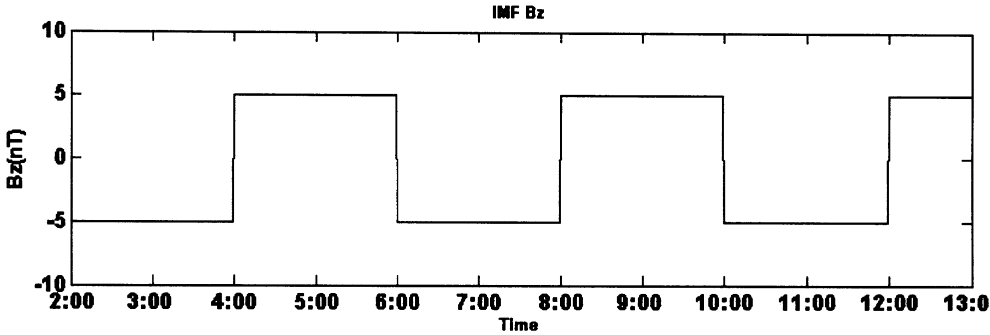

Figure 3.1 The IMF *Bz* component of the solar wind inputs to the OpenGGCM model.

3.3.1 Polar cap potential drops and Dst

To get an overall impression of the effect of the coupled model, a time series of the polar cap potential drop and estimated Dst are plotted in Figure 3.2. The estimated Dst is calculated by taking a four-point average of magnetic field perturbation near the Earth at 3.5 R_E. This is a very crude estimate and only serves to reveal the general variations of the Dst. The polar cap potential drop is obtained by subtracting the maximum and the minimum potential in the northern ionosphere.

For the Dst panel, the two runs reach the same Dst at 02:00 when the coupling is turned on for the coupled run. The Dst in the coupled run quickly drops under southward IMF driving from 02:00 to 04:00 while the Dst in the uncoupled run stays roughly the same since the preconditioning uses the same southward IMF driving. After the northward turning at 04:00, Dst in both runs recovers while the coupled one recovers slightly slower than the uncoupled one. The next southward IMF driven drops the coupled Dst even more because the ring current energy is increasing. The continuous decreasing minimum Dst may be caused by the loss mechanism of ions being turned off. It has been shown in a LFM/RCM coupled run that Dst can level out when the ion loss is turn on. [*Toffoletto,* 2011, private communication].

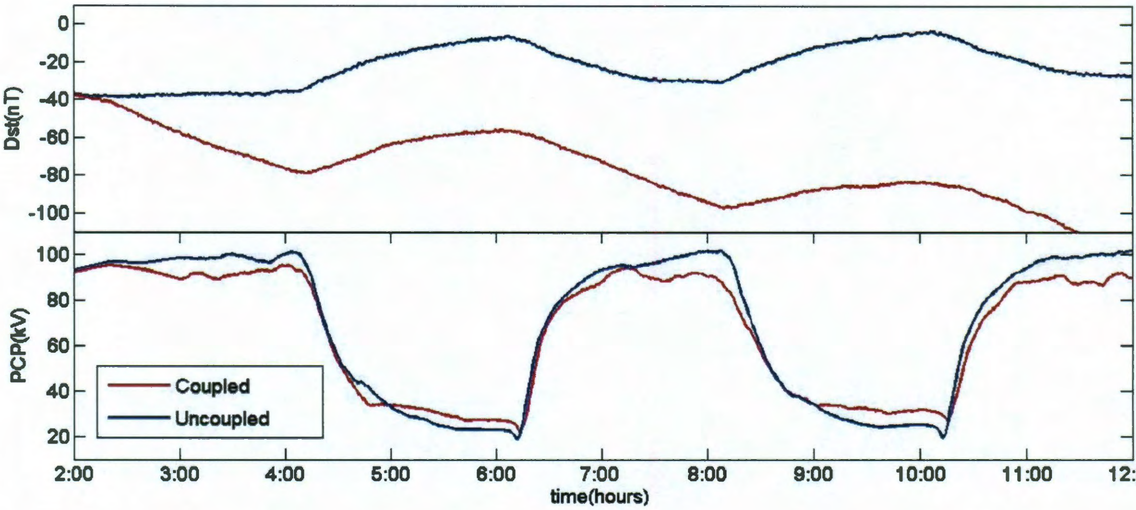

Figure 3.2 Estimated Dst and polar cap potential drop from simulation time 02:00 to 12:00 for the coupled run (red) and uncoupled run (blue).

The polar cap potential drop in the coupled run is lower than the uncoupled one during southward IMF driving but higher during northward IMF driving, as shown in the bottom panel in Figure 3.2. The difference is very small, only ~10%. However, the conclusion of the RCM coupling effect to the OpenGGCM potential cannot be drawn here since in some other test runs where the RCM's boundary is determined by open/closed fieldlines, the potential drop in the coupled run can be higher than the standalone OpenGGCM run.

3.3.2. Inner magnetosphere pressure and density

Figure 3.3 shows an equatorial view of the plasma pressure for times 08:00, 10:00 and 12:00 for both the coupled OpenGGCM/RCM and OpenGGCM only. The upper panels are from the coupled OpenGGCM/RCM and the bottom panels are from the standalone OpenGGCM. It is apparent that the coupled model produces a westward-peaked ring current with much more realistic pressure while the OpenGGCM-only has a very weak symmetric ring current. At the end of the last southward IMF interval, the peak pressure in the coupled model is ~ 40 nPa but the peak pressure in the standalone OpenGGCM is

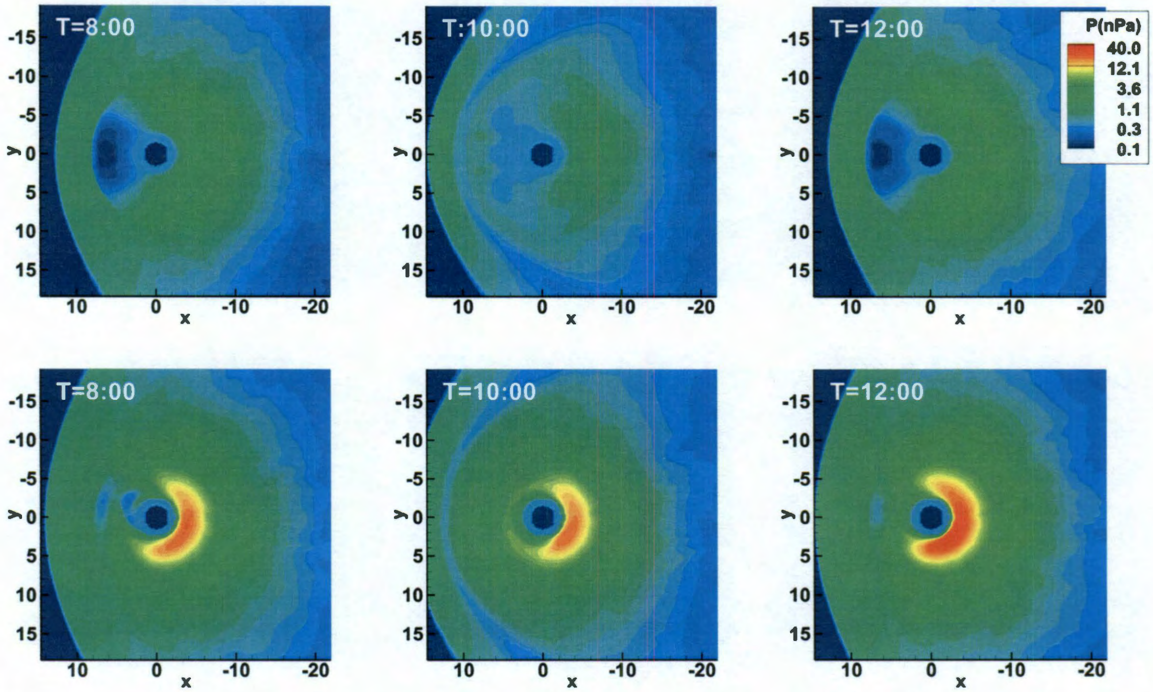

Figure 3.3 Equatorial pressure for OpenGGCM only (top row) and coupled OpenGGCM/RCM (bottom row)

only ~ 2 nPa. At T=12:00, the ring current in the coupled run is more symmetric than at T=08:00. Note that, in the one-way coupled mode, the RCM usually produces a ring current with peak pressure at ~100 nPa or more under similar driving conditions. It has been shown that self-consistent magnetic field usually reduces ring current pressure [*Zaharia et al.*, 2000].

The increase in the ring current pressure on the nightside is due to the fact that gradient and curvature drifts carry injected energetic ions quickly around to the dayside and place some of them on trapped orbits, whereas $E \times B$ drift by itself would just carry these particles to the dayside magnetopause. On the dayside, there is a weak pressure region in the OpenGGCM only run, since the MHD only transport plasma in the $E \times B$ drift direction and thus the earthward convected plasma cannot get into that region but lost through the dayside magnetopause. However, the RCM can keep track of those particles that should be in closed drift paths and these particles fill the dayside magnetosphere. The increase of pressure in the dayside inflates the magnetosphere as the magnetopause in the coupled run is more sunward compared to the uncoupled run.

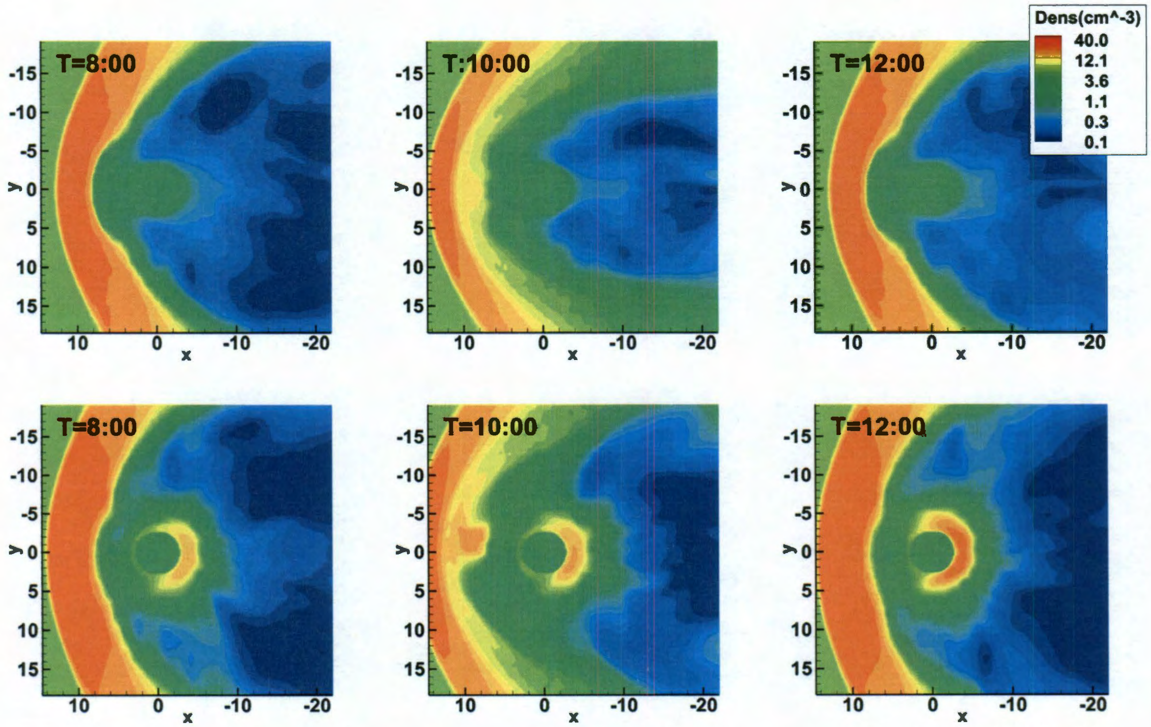

Figure 3.4 Equatorial density for OpenGGCM only (top row) and coupled OpenGGCM/RCM (bottom row)

Figure 3.4 shows the equatorial density in a similar format as Figure 3.3. The OpenGGCM has very low density in the inner magnetosphere while the coupled one shows the ring current with higher density. The added plasmasphere essentially gives an inner boundary density of ~20 particles per cc but drops quickly further out from the Earth. In this run, the standalone OpenGGCM has an inner boundary density source density of ~ 2 particles per cc. The density profile in the inner magnetosphere is mostly enforced by the RCM.

3.3.3 Magnetic field in the OpenGGCM

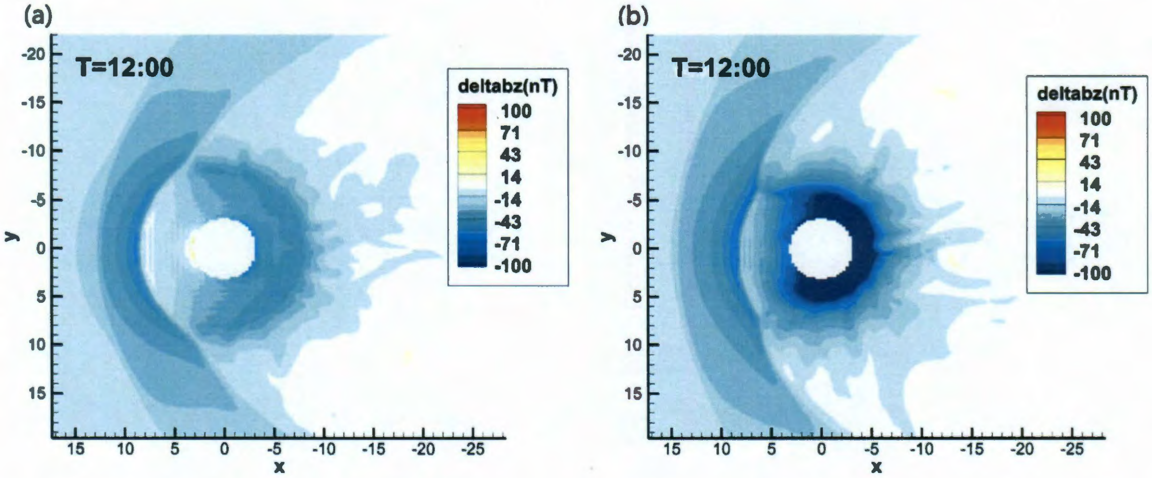

Figure 3.5 ΔB_z in the equatorial plane for (a) the uncoupled run and (b) the coupled OpenGGCM/RCM at T=12:00.

One response of the OpenGGCM to the increased ring current pressure is the reduction of the magnetic field in the near Earth region. When pressure in the OpenGGCM increases, the field lines stretch to balance the increased pressure gradients. The ΔB_z (differences to the dipole field) in the equatorial plane for the uncoupled run and the coupled one at the end of the last two hours southward IMF driven is shown in Figure 3.5. Compared to the standalone OpenGGCM, the coupled model shows overall reduction in magnetic field that is particularly strong near the ring current peak (minimum ΔB_z for panel (b) is -190 nT). At geosynchronous orbit on the nightside, the field reduction in the coupled model is ~ -67 nT compared to ~ -40 nT in the uncoupled one. The difference is even more pronounced near the Earth.

The more stretched field lines are shown in Figure 3.6, in which the blue colored field lines are traced from ionosphere with colatitudes (25°, 26°, 27°, 28°, 30°) at midnight local time. While the standalone OpenGGCM shows some field stretching after the last two hours southward IMF driving, the fieldlines in (a) are still more dipolar like as compared to the field lines in the coupled model (b). Lack of magnetic field stretching in the standalone MHD models due to lack of inner magnetosphere pressure is known to be unrealistic. The more stretched field lines obtained in the coupled model is consistent with the findings in early studies from other MHD/RCM coupling efforts [e.g. *De Zeeuw et al.*, 2004, *Huang et al.*, 2006] as well as magnetosphere equilibrium code/RCM coupling [*Toffoletto et al.*, 2001].

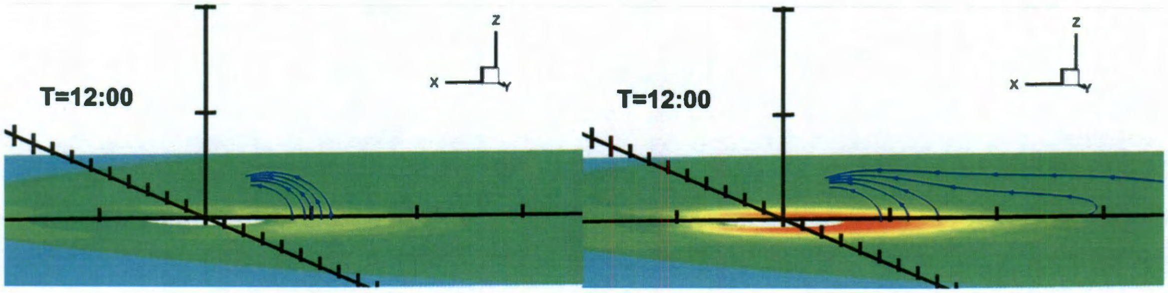

Figure 3.6 Magnetic field lines traced from co-latitudes (25°, 26°, 27°, 28°, 30°) at midnight local time for (a) the uncoupled run and (b) the coupled OpenGGCM/RCM at T=12:00. Ticks are spaced every 5 R_E and the color contours represent pressure.

3.3.4 Ionospheric responses

One of the major characteristics of inner magnetosphere electrodynamics is the build-up of region-2 field-aligned current in the ionosphere to shield the driven convection electric field and the standalone MHD model usually fails to adequately represent the region-2 currents. Figure 3.7 shows the field-aligned currents and the corresponding potential maps for two times 08:50 and 10:50. The region-2 currents are small even for the southward driven case (10:50). Note the MHD models should not need inner magnetosphere drift physics to generate region-2 currents [*Garner*, 2003]. The explanation for the weak region-2 currents in global MHD models is probably lies in poor resolution. One consequence of the weak region-2 currents is the convection electric field at 10:50 shown in Figure 3.6 for the uncoupled model is not well-shielded.

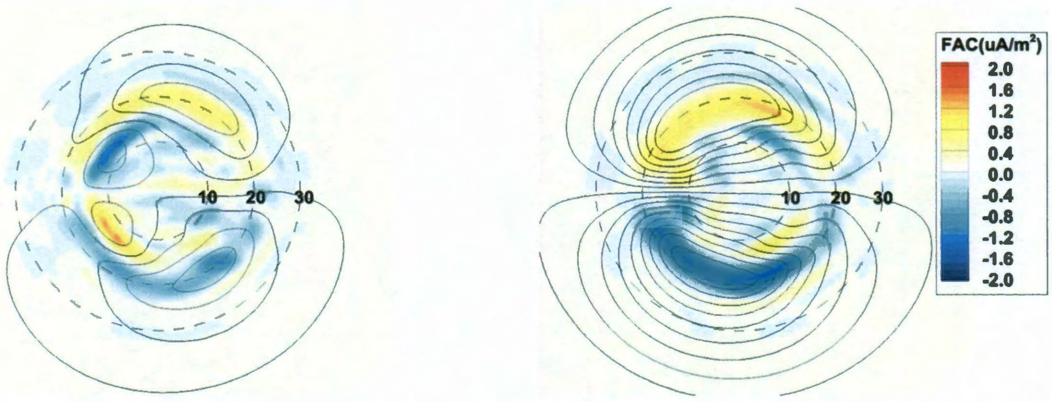

T = 08:50:00 **T = 10:50:00**

Figure 3.7 Field-aligned current density (color contour) and potential (line contour) on the ionosphere from the uncoupled OpenGGCM run for T = 08:50:00 (50 minutes after the second northward turning) and T = 10:50:00 (50 minutes after the last southward turning). Positive currents are downward into the ionosphere. The dashed circles show the co-latitudes and the Sun is to the left.

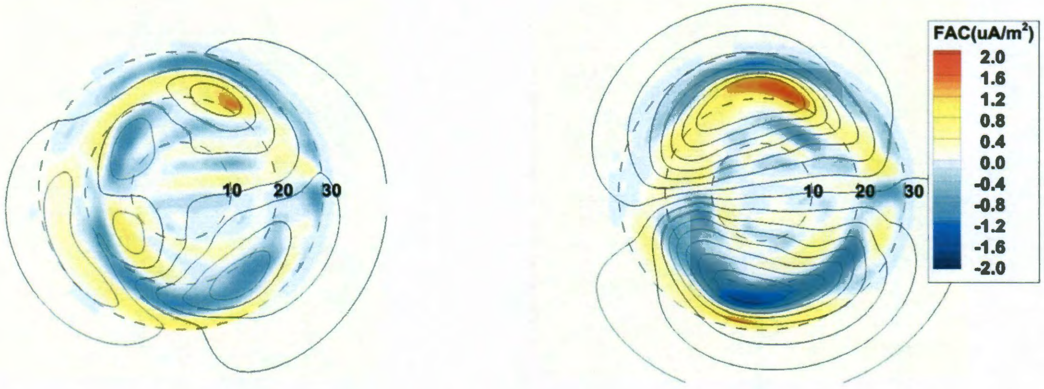

T = 08:50:00 **T = 10:50:00**

Figure 3.8 Field-aligned currents (color contour) and potential (line contour) on the ionosphere from the coupled OpenGGCM run for T = 08:50:00 (50 minutes after the second northward turning) and T = 10:50:00 (50 minutes after the last southward turning). Positive currents are downward into the ionosphere. The dashed circles represent co-latitudes and the Sun is to the left.

Figure 3.8 shows the same plots at 08:50 and 10:50 for the coupled model. Both the region-1 and region-2 currents are stronger compared to the uncoupled run. The stronger region-2 currents provide some shielding of the convection electric field as evidenced by the greater distance between equipotentials at lower latitudes for the southward IMF case. For the northward driven time, the region-2 currents rotates the electric field in the coupled run however they are not strong enough to produce over-shielding [e.g. *Spiro et al.*, 1988].

These ionospheric responses are consistent with other coupling studies [*De Zeeuw et al.* 2004, *Pembroke et al.*, 2011] and thus encouraging. It is expected the region-2 currents can be even stronger during steady southward IMF. However, although the region-2 currents are increased in the coupled run, they are still constrained by model resolution. Another approach to compute the region-2 currents will be discussed in Chapter 4 and it could improve the resolution of the MHD region-2 currents.

3.3.5 Time series at geosynchronous orbit

To see more clearly on the behaviors of the coupled model, the time series of several important quantities at geosynchronous orbit (r = 6.6 R_E) are plotted for three local times 03:00, 00:00 and 21:00.

Figure 3.9 shows the magnetic field variations at geosynchronous orbit. Again, it is seen that the coupled model overall has lower *Bz* than the standalone one. However the abrupt variation of *Bz* in the coupled model is more pronounced than the uncoupled one, as oscillations are observed both under southward IMF and northward IMF. At ~08:00 and 00:00 LT, *Bz* in the coupled model is even higher than the uncoupled one. Figure 3.10 shows the same time series but for the pressure, which is always higher in the coupled run than in the standalone OpenGGCM run. The pressure increases for all local times shown and there is more time variability on time scales less than an hour. These oscillations in the pressure seem to correspond to the variations in the magnetic field. The x-velocity time variations are shown in the same format in Figure 3.11. The x-velocity from the standalone OpenGGCM shows oscillations as well as the x-velocity from the coupled run. However, the amplitude of changes in velocity is much larger in the coupled model. The increase in earthward flow seems to occur when there is an increase in *Bz* (dipolarization).

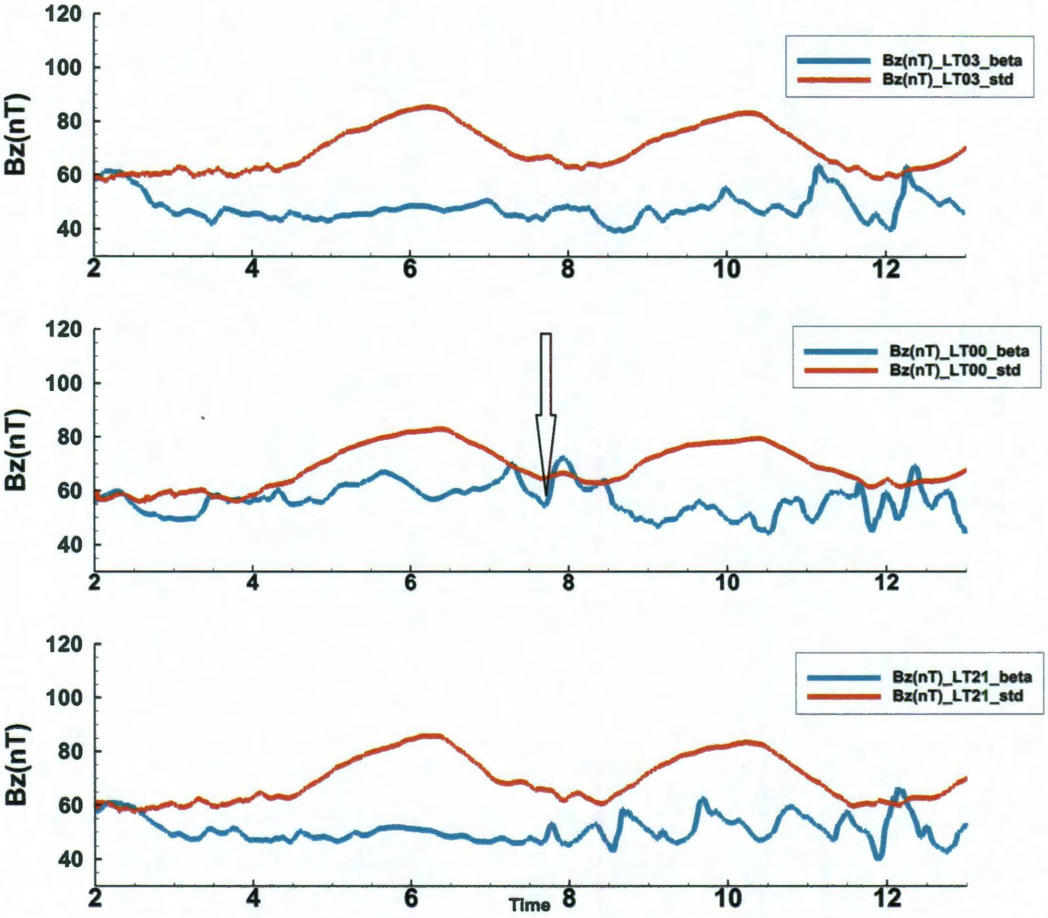

Figure 3.9 Variations of magnetic field *z* component as a function of time in hours from the coupled model (cyan) and the uncoupled model (red) at geosynchronous orbit for local times 03:00, midnight and 21:00.

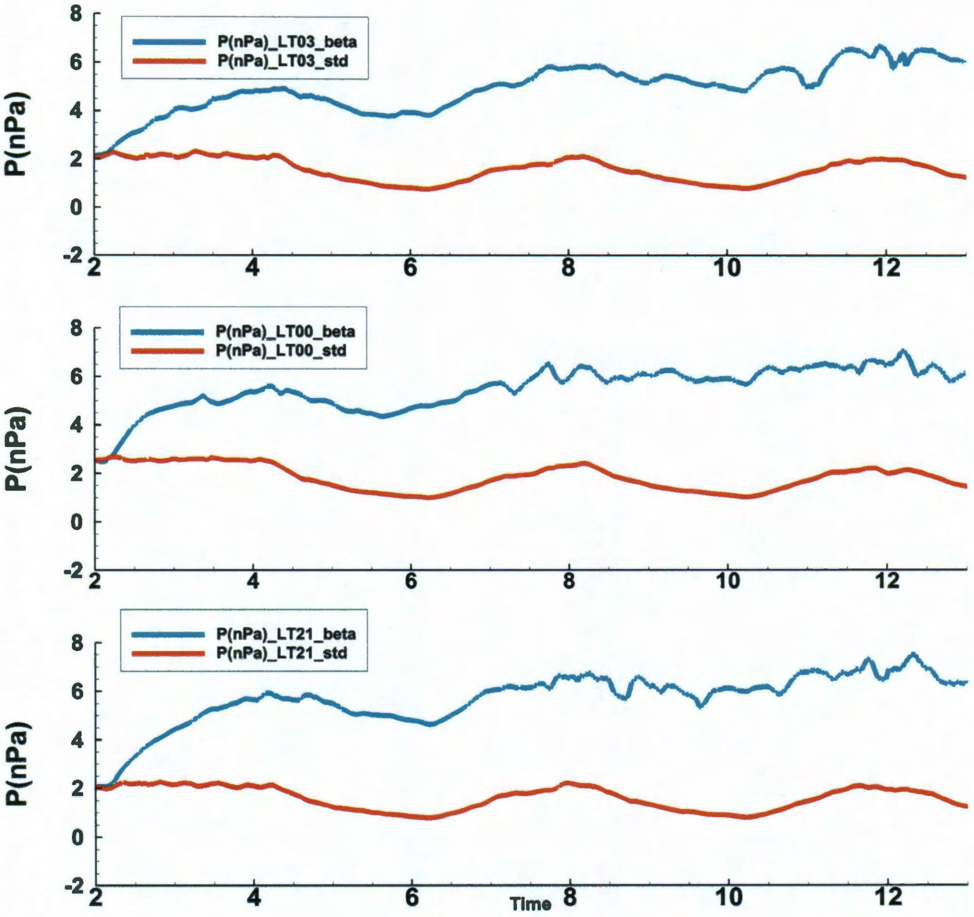

Figure 3.10 Pressure variations as a function of time in hours from the coupled (cyan) model and the uncoupled model (red) at geosynchronous orbit for local times 03:00, midnight and 21:00.

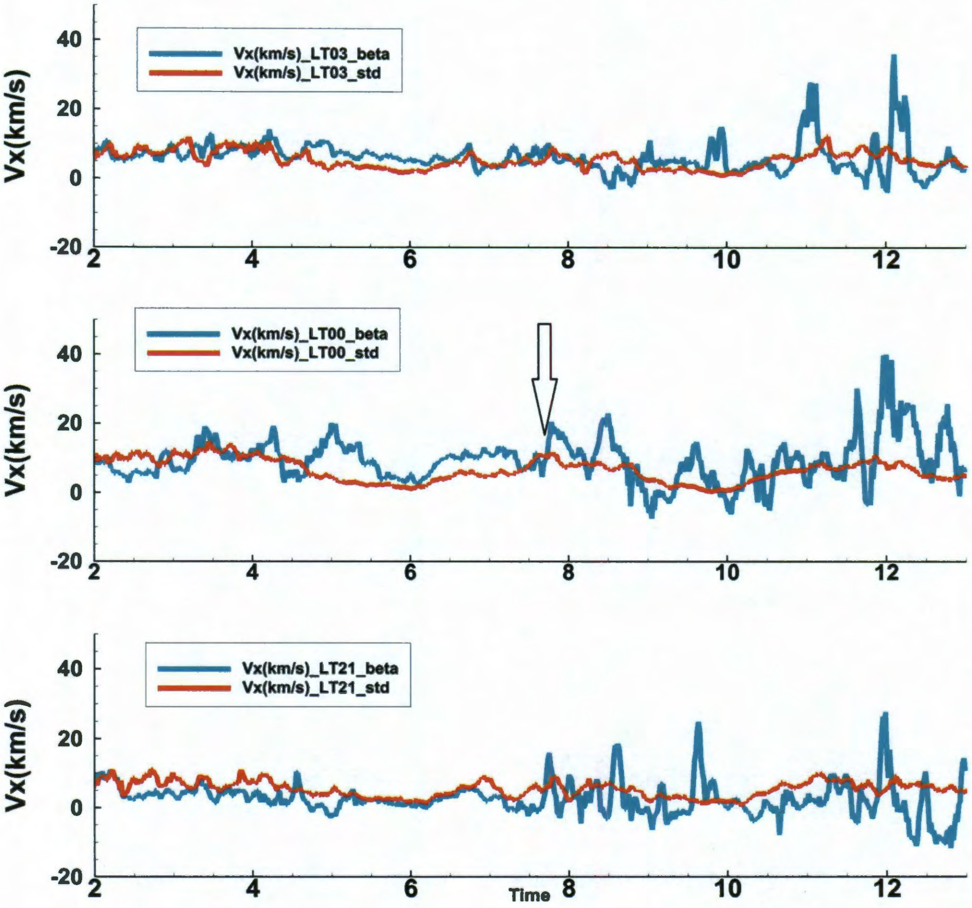

Figure 3.11 Velocity x component time variations from the coupled model (cyan) and the uncoupled model (red) at geosynchronous orbit for local times 03:00, midnight and 21:00.

These time series plots show a more dynamic inner magnetosphere compared to the standalone OpenGGCM. To investigate the cause of those variations, the entropy parameter $pV^{5/3}$(actually calculated as $(\int p^{3/5}\frac{ds}{B})^{5/3}$) is plotted in the equatorial plane for both runs in Figure 3.12. Points on open field lines are blanked with white color. At

07:52, a bubble, coming out of the x line, is seen at ~ -15 R_E slightly on the pre-midnight sector for the first panel in the bottom row. As described in Chapter 2, these low entropy bubbles tends to move earthward and are associated with field dipolarization. It is possible that this bubble brings the variations shown in Figure 3.9 and Figure 3.11 in which increases in both *Bz* and *Vx* are observed.

There is another mechanism that also could cause the bubble found in the time series. At 07:54, there is a bubble and blob pair formed at ~x = -10 R_E post midnight. The bubble moves earthward and the blob quickly surges tailward due to interchange. The formation of the bubble/blob could be attributed to pressure diffusion and a more detailed study on the bubble/blob is presented in Chapter 5 [*Hu et al.*, 2011]. Given the magnitude of the velocity variation shown in Figure 3.11, the overall oscillations in the coupled run are more likely due to the bubbles that formed with the blobs. Figure 3.12 also shows the inner edge of the plasmasheet is deformed by these bubbles compared to the uncoupled run.

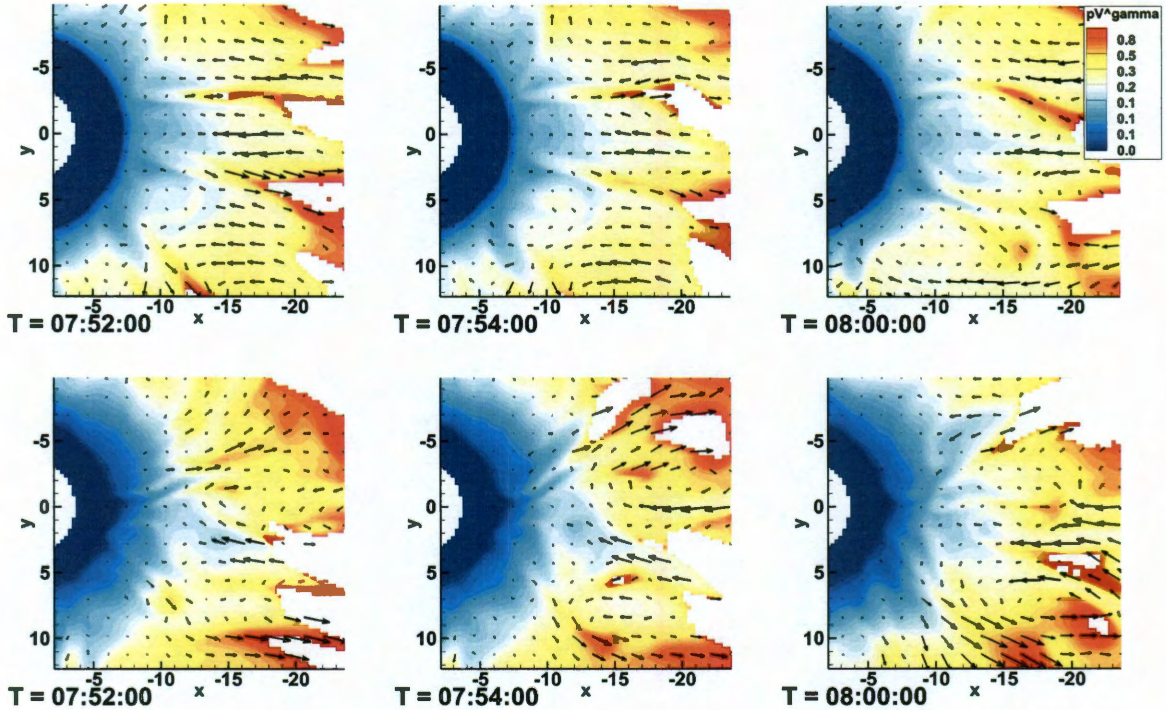

Figure 3.12 Entropy parameter $(\mathrm{nPa}(R_E/\mathrm{nT})^{5/3})$ on the equatorial plane from the uncoupled run (top row) and the coupled run (bottom row) for three times 07:52, 07:54 and 08:00, with arrows representing the velocity in the plane.

3.4 The 2007-03-23 Substorm event

In Chapter 2, the one-way coupled model was used to simulate the 2007-03-23 substorm event and thus this event is a very good candidate to test the coupled model. In the two-way coupled run, the same resolution (630x200x300) as the one in Chapter 2 is used and the other inputs are set as in *Raeder et al.* 2008. Note the beta-based boundary condition is not used for this run. The original method described in Chapter 2 is used to determine the RCM's outer boundary condition.

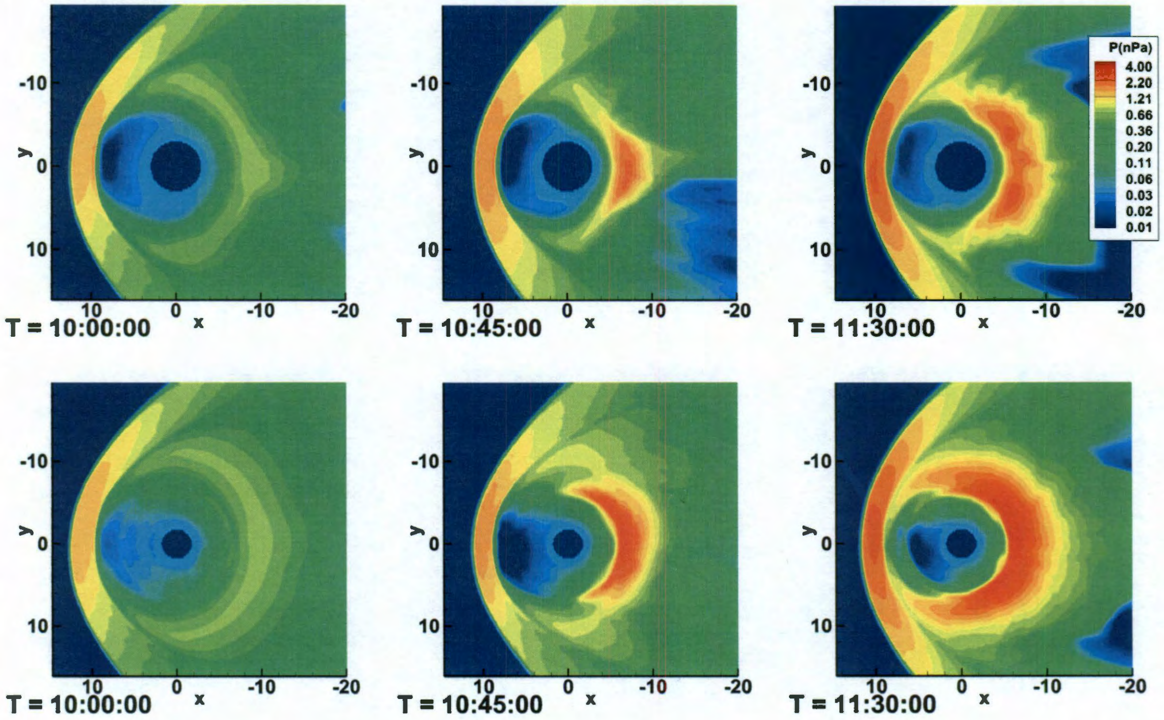

Figure 3.13 OpenGGCM pressure in the equatorial plane for the uncoupled run (top row) and the coupled run (bottom row) at 10:00, 10:45 and 11:30.

Figure 3.13 shows the pressure comparison of the coupled event and the uncoupled one which has been described in Chapter 2. As mentioned previously, the substorm onset was near 10:45 thus at 10:00 it is before the injection and the 11:30 is after. At 10:00, the difference in the ring current pressure is small between the two runs except on the dayside. This is because the IMF was mostly northward before 10:00. After the substorm onset, the injected particles cause the inner magnetosphere pressure to increase, which is reproduced in both runs. However the coupled one shows a stronger injection due to the RCM, as the post-substorm pressure is approximately twice as large as the uncoupled one.

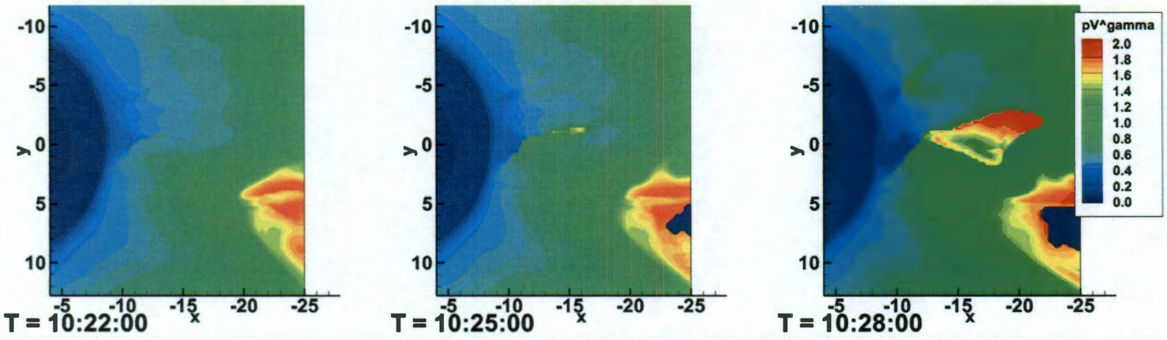

Figure 3.14 Bubble/blob pair in the two-way coupled OpenGGCM/RCM simulation for the substorm occurred on 2007-03-23, in the same format as Figure 2.7.

Despite the pressure differences, the overall dynamics in the coupled run is qualitatively similar, as the coupling effect is only more pronounced after the substorm onset. Figure 3.14 shows the entropy parameter in a similar fashion as Figure 2.7. The bubble blob pair before the onset of the substorm is also found in the coupled run, although in a different shape. This actually verifies our assumptions for the study presented in Chapter 2 that the injection process is quick and not too sensitive to the feedback of RCM pressure.

3.5 Discussion

In the idealized runs presented in this chapter, a beta-based RCM boundary condition is used to keep the RCM modeling region in the slow-flow part of the magnetosphere. This boundary condition by far gives the most stable results as runs using other boundary conditions may present fast tailward flows (> 600 km/s) in the near Earth region. Although the standalone OpenGGCM produces near earth tailward flows, those flows are much stronger in the coupled run.

Entropy analysis for these fast tailward flows suggests that these tailward flows are associated with blobs, similar to the ones shown in Figure 3.12. If the code diffuses plasma tailward, then a bubble blob pair can form (more details in Chapter 5). To see more clearly if the pressure is diffused by the OpenGGCM, a test was conducted in which the OpenGGCM pressure under two resolutions is nudged toward a constant specified pressure profile. The higher resolution grid has 38 million cells with a minimum grid spacing of ~0.15 R_E. The lower resolution grid has 3 million cells with a minimum grid spacing of ~ 0.3 R_E. The constant source has a peak pressure of ~ 75 nPa and drops to 0 outside -6 R_E.

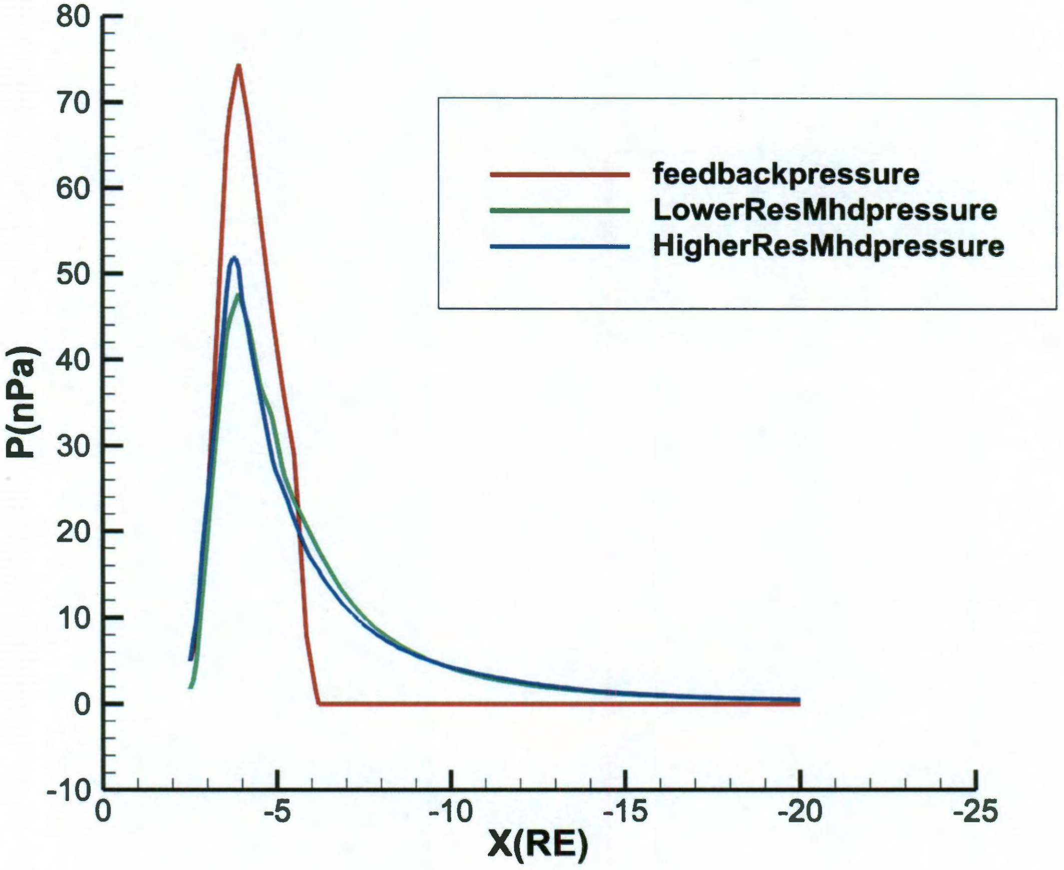

Figure 3.15 Pressure profile along the nightside x axis for the constant source, lower resolution OpenGGCM pressure in response to the constant source and higher resolution OpenGGCM pressure in response to the constant source.

Figure 3.15 shows the constant source along with the OpenGGCM's responses to the nudging after reaching quasi-steady state. The peak pressures in the OpenGGCM are lower than the feedback pressure for both resolutions and there is clear evidence of numerical diffusion outside -6 R_E. The higher resolution result is better in that it leads to higher peak pressure and sharper overall profile. This suggests a higher resolution might be needed for the coupled model due to the increased inner magnetosphere pressure.

3.6 Summary

In this chapter we have described the two-way coupling of the RCM to the OpenGGCM global MHD model. The initial results shows encouraging features in the coupled model such as a more realistic inner magnetosphere pressure and density, stronger region-2 currents and shielding of the convection electric field.

We found the inner magnetosphere is more dynamic in the coupled model compared to the uncoupled case, and oscillations are observed at geosynchronous orbit. The flows and magnetic field change are associated with low-entropy bubbles that either formed at the tail x-lines or bubble/blob pairs. Although bubble/blob pairs do form in the standalone version, the tailward flows associated with the blobs are more frequently seen in the coupled run.

The method for coupling described in this chapter is not necessarily the best approach, although it is probably the simplest, and the coupling project is still ongoing. For example, the use of a reduced plasmasphere could be replaced with a more realistic one. The choice of RCM's beta based boundary condition limits the RCM modeling region to 5-6 R_E on the nightside and thus important drift physics outside of the RCM modeling region is missing from the coupled model. MHD stability issues often present themselves when MHD is coupled with RCM and there is certainly room to improve on the MHD numerics as well. Nevertheless, the initial results from coupling the RCM to MHD are encouraging, making us optimistic about eventually reaching the goal of a more comprehensive model of the Earth's magnetosphere which can realistically reproduce large-scale features as well as the ring current.

Chapter 4

A Direct-integration Method for Birkeland Current Calculation

4.1 Introduction

A major difficulty with global magnetohydrodynamics (MHD) models is the under-resolution of the Birkeland currents that are computed near the inner boundary of the code [*De Zeeuw et al.*, 2004]. These Birkeland currents are used as the inputs to the MHD ionosphere module in the current conservation equation described in Chapter 1 and are used to determine the ionospheric convection pattern and in turn the boundary condition (plasma motion) at the inner boundary of the MHD code. This coupling of magnetosphere and ionosphere through Birkeland currents plays a very important role in magnetosphere convection and most global MHD models include this calculation as part of their model. The region-2 Birkeland currents are often unrealistically weak in MHD models and as a result they often fail to reproduce important inner magnetosphere electrodynamics such as shielding of the convection electric field at low latitudes.

As was shown in the previous chapter, coupling the RCM to the MHD models results in stronger region-2 currents due to increase of pressure gradients, but these currents are still not nearly as well-defined as the ones obtained in the RCM using the 2D

Vasyliunas equation (an example is shown in Figure 4.5). The MHD field-aligned currents are usually obtained by taking the field-aligned component of the curl of the magnetic field near the inner boundary which are then mapped down onto the ionosphere along dipole magnetic field lines (assuming $\frac{J_{\parallel}}{B}$ is constant along the field line). It is believed that poor resolution near the inner boundary and low ring current pressure are the reasons for the weak and diffuse MHD region-2 currents and part of the motivation for this work is to see if there is a more accurate way of computing these currents. In this chapter, we explore the use of an alternative method of computing the Birkeland currents in MHD and compare it with the original method used.

From the RCM's perspective, having an accurate way to compute Birkeland currents from MHD quantities is useful for compensating for one of RCM's major limitations. While the RCM accurately computes the Birkeland currents using Vasyliunas equation, it assumes the magnetic field line and the plasma are in force equilibrium. That means that the RCM cannot treat fast flows when the inertial term becomes large. It also limits the RCM's validity for time scales longer than MHD wave travel times. In contrast, the MHD models do not assume slow flow and the MHD Birkeland currents contain contributions from the inertial effects. If the MHD Birkeland currents can be accurately computed, they could be used to add the inertial effects back to the RCM. The two-way coupled OpenGGCM/RCM has inertial currents in the Birkeland currents but they are poorly resolved.

In this chapter, I will describe the initial attempt at a new way to calculate the Birkeland currents from the MHD magnetic field. I will start by deriving the direct integration formula (section 4.2) and then present some preliminary test results.

4.2 Generalized Vasyliunas equations

We start from the basic equation of conservation of current (4.1):

$$\nabla \cdot \vec{J} = 0 \tag{4.1}$$

Apply the divergence theorem to a small part of the flux tube by expanding the divergence in magnetic coordinates (α, β, φ),

$$\nabla \cdot \vec{J} = \frac{1}{h_\alpha h_\beta h_\varphi}[\frac{\partial(h_\alpha h_\beta J_\varphi)}{\partial\varphi} + \frac{\partial(h_\alpha h_\varphi J_\beta)}{\partial\beta} + \frac{\partial(h_\beta h\varphi J_\alpha)}{\partial\alpha}]=0 \tag{4.2}$$

In the magnetic coordinates, the gradient of a scalar *u* is given by

$$\nabla u = \vec{\alpha}\frac{1}{h_\alpha}\frac{\partial u}{\partial\alpha} + \vec{\beta}\frac{1}{h_\beta}\frac{\partial u}{\partial\beta} + \vec{\varphi}\frac{1}{h_\varphi}\frac{\partial u}{\partial\varphi} \tag{4.3}$$

where α, β, φ are unit vectors in the directions of the gradients of the three coordinates. Substituting *u* with α, β, φ into equation (4.3), we get

$$|\nabla\alpha| = \frac{1}{h_\alpha}, |\nabla\beta| = \frac{1}{h_\beta}, |\nabla\varphi| = \frac{1}{h_\varphi} \tag{4.4}$$

in magnetic coordinates,

$$\vec{B} = \nabla\alpha \times \nabla\beta \tag{4.5}$$

These coordinates are known as Euler potentials. With (4.4), we have $B = \frac{1}{h_\alpha h_\beta}$.

Equation (4.2) can be written as

$$B\frac{\partial(\frac{J_{\parallel}}{B})}{\partial s}+\frac{1}{h_{\alpha}h_{\beta}h_{\varphi}}[0+\frac{\partial(h_{\alpha}h_{\varphi}J_{\beta})}{\partial\beta}+\frac{\partial(h_{\beta}h\varphi J_{\alpha})}{\partial\alpha}]=0 \qquad (4.6)$$

where s is the distance along the field line.

The second term in equation (4.6) is the divergence of $J_{\perp}=(0,J_{\alpha},J_{\beta})$ in magnetic coordinates.

Equation (4.6) then can be written as

$$B\frac{\partial(\frac{J_{\parallel}}{B})}{\partial s}=-\nabla\cdot J_{\perp} \qquad (4.7).$$

Integrating from the equatorial plane to the ionosphere, we obtain an expression for the Birkeland currents

$$J_{\parallel i}=-B_i\int_e^i\frac{ds}{B}\nabla\bullet\vec{J}_{\perp} \qquad (4.8).$$

For open field-lines we use

$$\left(\frac{J_{\parallel}}{B}\right)_i=\left(\frac{J_{\parallel}}{B}\right)_b-\int_b^i\frac{ds}{B}\nabla\cdot\vec{\mathrm{J}}_{\perp} \qquad (4.9).$$

where b is the boundary for the integration and subscript i refers to point in the ionosphere.

The generalized Vasyliunas equations (4.8) and (4.9) provide an alternative way of computing the Birkeland currents from a MHD model. Compared to using Ampere's law near the inner boundary of the MHD code, this formula takes contributions from not only the poorly resolved ionosphere region but also the equatorial region where the MHD code usually has better resolution. Since the equatorial magnetic field is much weaker than the ionospheric field, it is expected that the integrand in equation (4.8) would weigh heavily near the equatorial plane.

4.3 Computing $\nabla \cdot \vec{J}_\perp$

From equation (4.8) and (4.9), it is clear that the success of this method partly depends on the accuracy of computing the integrand $\frac{\nabla \cdot \vec{J}_\perp}{B}$. To obtain $\nabla \cdot \vec{J}_\perp$, we have two choices numerically: one is to get $\nabla \cdot \vec{J}_\perp$ directly and the other is to compute $-\nabla \cdot \vec{J}_\parallel$ since $\nabla \cdot \vec{J}_\perp + \nabla \cdot \vec{J}_\parallel = \nabla \cdot \vec{J} = 0$.

The direct calculation yields

$$\begin{aligned}
J_{\perp x} &= ((B^2 - Bx^2)Jx - BxByJy - BxBzJz) / B^2 \\
J_{\perp y} &= (-ByBxJx + (B^2 - By^2)Jy - ByBz) / B^2 \\
J_{\perp z} &= (-BxBzJx - ByBzJy + (B^2 - Bz^2)Bz) / B^2
\end{aligned} \tag{4.10}$$

$$J_{\parallel i} = -B_i \int_e^i \frac{ds}{B} \left(\frac{\partial J_{\perp x}}{\partial x} + \frac{\partial J_{\perp y}}{\partial y} + \frac{\partial J_{\perp z}}{\partial z} \right)$$

while the indirect calculation yields

$$J_{\|i} = -B_i \int_e^i \frac{ds}{B} \nabla \bullet \vec{J}_\perp = B_i \int_e^i \frac{ds}{B} \nabla \bullet \vec{J}_\|$$

$$= B_i \int_e^i \frac{ds}{B} \nabla \bullet \left(\frac{((\nabla \times \vec{B}) \bullet \vec{B}) \vec{B}}{\mu_0 B^2} \right)$$

$$= B_i \int_e^i \frac{ds}{B} \left(\vec{B} \bullet \nabla \left(\frac{(\nabla \times \vec{B}) \bullet \vec{B}}{\mu_0 B^2} \right) \right) \qquad (4.11).$$

$$= B_i \int_e^i \frac{ds}{B} \left(B_x \frac{\partial T}{\partial x} + B_y \frac{\partial T}{\partial y} + B_z \frac{\partial T}{\partial z} \right)$$

$$T = \frac{(\nabla \times \vec{B}) \bullet \vec{B}}{\mu_0 B^2}$$

For the results presented here, both approaches are implemented but only the results from the second approach are presented as examples. I will first present application of the new method in OpenGGCM and OpenGGCM/RCM models and then an analysis for analytical cases using the Tsyganenko [*Tsyganenko et al.*, 1996] magnetic field model.

4.4 OpenGGCM tests

4.4.1 Initial test using standalone OpenGGCM outputs

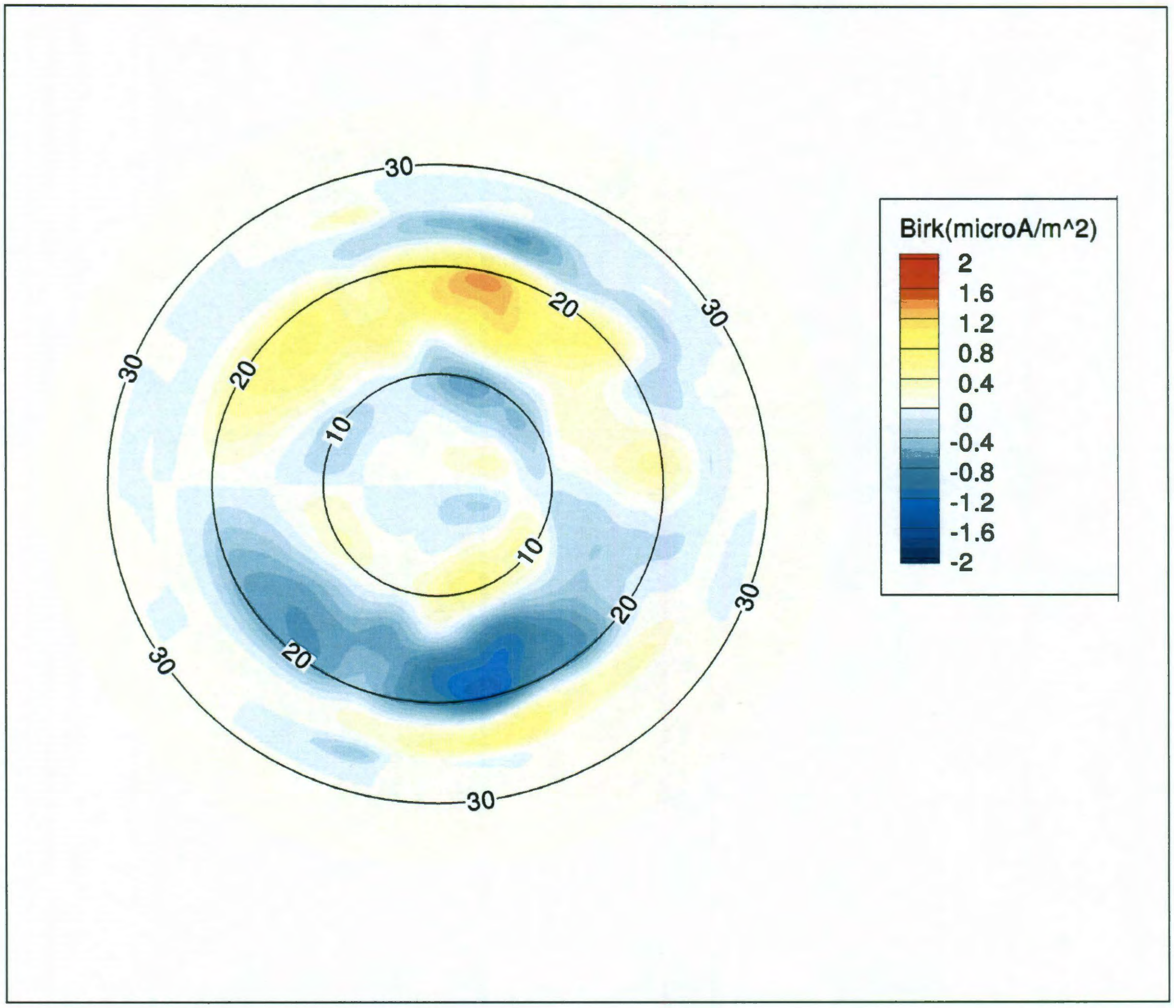

Figure 4.1 OpenGGCM Birkeland currents in the ionosphere. Solid circle lines represent co-latitudes (90° -latitude). The sun is to the left. Positive currents correspond to down into the ionosphere.

Figure 4.1 shows the usual Birkeland currents obtained in OpenGGCM using the Ampere's law near the inner boundary. The sun is to the left. Region-2 field-aligned currents between 20° and 30° co-latitudes are present but are weak. The region-1 currents in the high latitude region (below 20° co-latitude) are well-defined but diffusive. The

OpenGGCM grid resolution for where the current is taken is 0.3 R_E x 0.6 R_E x 0.8 R_E. Figure 4.2 shows the Birkeland currents obtained using the direct-integration method, using the same OpenGGCM outputs. For open field lines, the boundary current value (the first term of the RHS of equation (4.9)) is taken at the 6.5 R_E sphere. Thus the currents on open field lines obtained using the new method look similar to the ones obtained from Ampere's law. However, there are big differences in the closed field line region as the currents are noticeably sharper and stronger. Particularly, it is encouraging that the region-2 sense currents are much stronger.

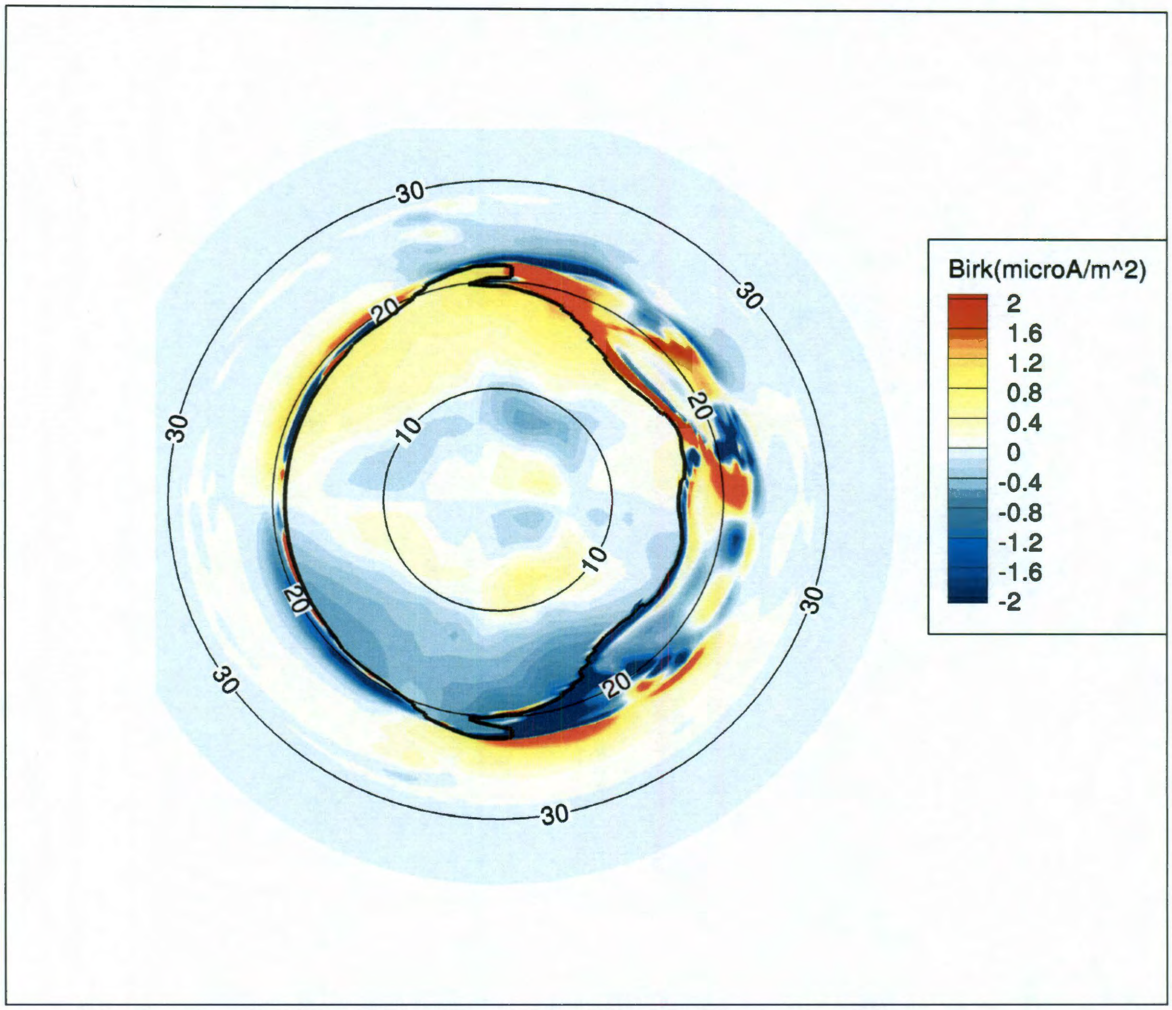

Figure 4.2 Birkeland currents from field line integration. For regions of the polar cap on open field lines, the integration stops at sphere of radius 6.5 R_E. Solid black curve represents the open/closed boundary.

There is a sharp boundary (discontinuity) for currents inside and outside the polar cap (shown as the thick black curve) due to the difference in the way closed and open field lines are treated. In the closed field line region, there are currents that look noisy and these currents may be artifacts from the tracing which I will discuss in section 4.5.3. If the currents in figure 4.2 are smoothed spatially using a 3 pass scheme, it begins to resemble the current distribution shown in Figure 4.1. The smoothed version is shown in Figure 4.3.

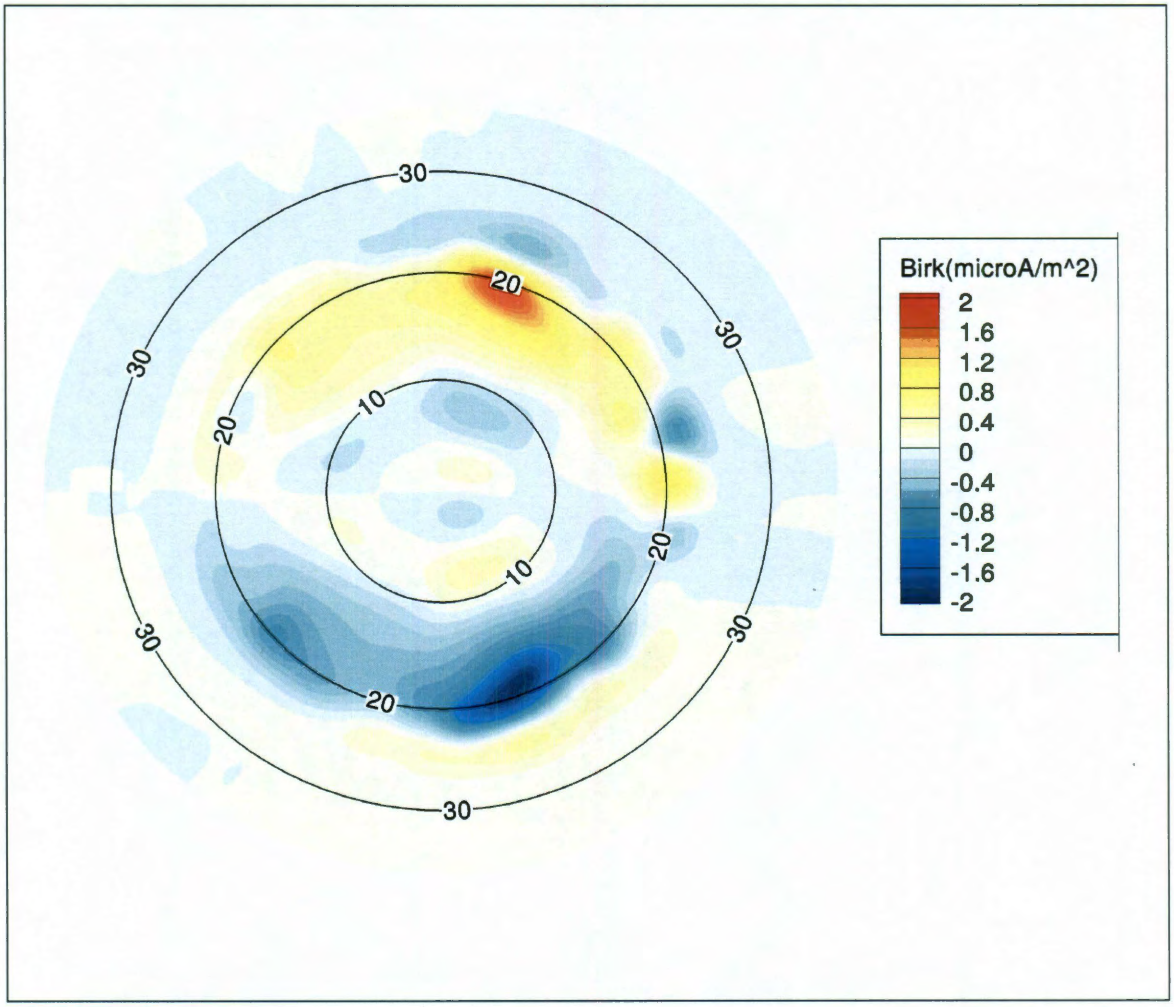

Figure 4.3 Integrated currents in Figure 4.2 after smoothing.

The new method was then applied to another time (3 hours earlier for a steady southward IMF run) from the OpenGGCM and the result is shown in Figure 4.4. It looks quite different from the traditional MHD Birkeland currents, because of the noisy features near the open/closed boundary especially on the dayside. These results suggest that the new method may sometimes have numerical difficulties. I will explore the conditions where it might be having problems in section 4.5.

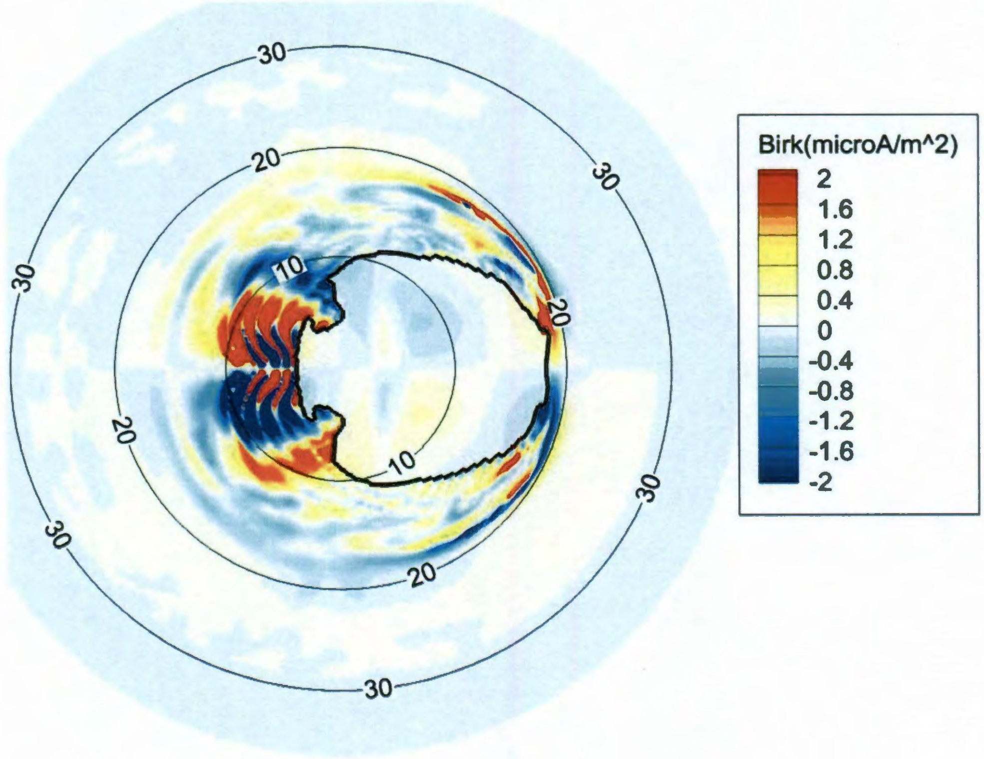

Figure 4.4 The currents obtained using the direct integration method for a different time from OpenGGCM output. The solid black curve represents the open/closed boundary.

4.4.2 Initial test in a two-way coupled OpenGGCM/RCM run

In this test run, the OpenGGCM still computes its currents and potentials in its usual way but it takes the feedback of pressure and density, in a slightly different way than the method describe in Chapter 2. For the pressure, the MHD pressure is nudged towards $P = P_{MHD} \frac{P_{RCM} V^{5/3}}{[\int P_{MHD}^{3/5} ds / B]^{5/3}}$ to allow variations along the field line.

In the RCM modeling region, the Birkeland currents are calculated using two approaches; one is using the Vasyliunas equation as is traditionally done in the RCM and the other is to use the direct integration method described above but only in the RCM modeling region. The result using the Vasyliunas equation is shown in Figure 4.5. This is a typical RCM computed Birkeland current distribution with strong and well defined region-2 currents. The electric potential contours show the strong region-2 currents and the resulting strong shielding in the inner magnetosphere.

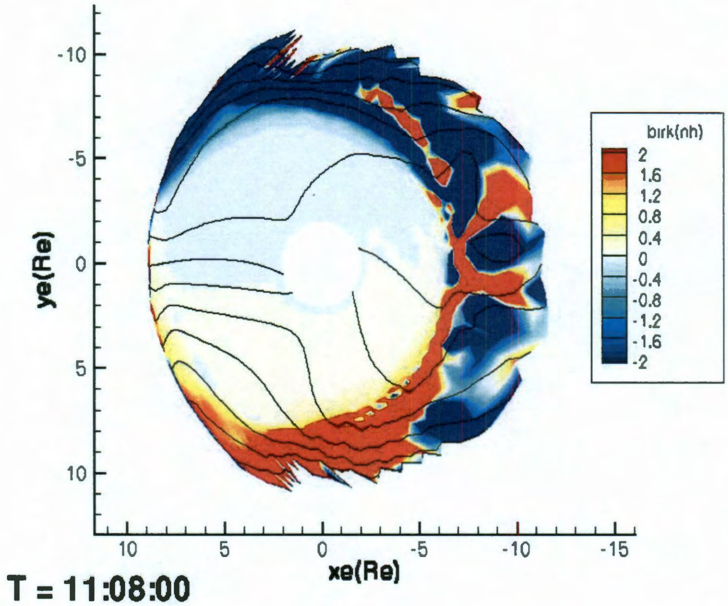

Figure 4.5 Birkeland currents obtained using the Vasyliunas equation in the RCM.

The direct-integration currents are shown in Figure 4.6 with OpenGGCM potentials. Figure 4.7 is the OpenGGCM currents computed using the Ampere's law method for the same time. By comparing these two figures, we once again see the original OpenGGCM currents are weak and diffusive and the new method gives sharper and stronger region-2 currents. The currents are overall better resolved in the RCM modeling region using the new method. Note the potentials in Figure 4.6 are solved using the currents shown in Figure 4.7 so the shielding is weak. In this coupled run, the OpenGGCM and the RCM were driven by the same potential solved by the OpenGGCM (potential shown in Figure 4.6). The RCM computed the currents using the Vasyliunas equation and solved for the corresponding potential for comparison only.

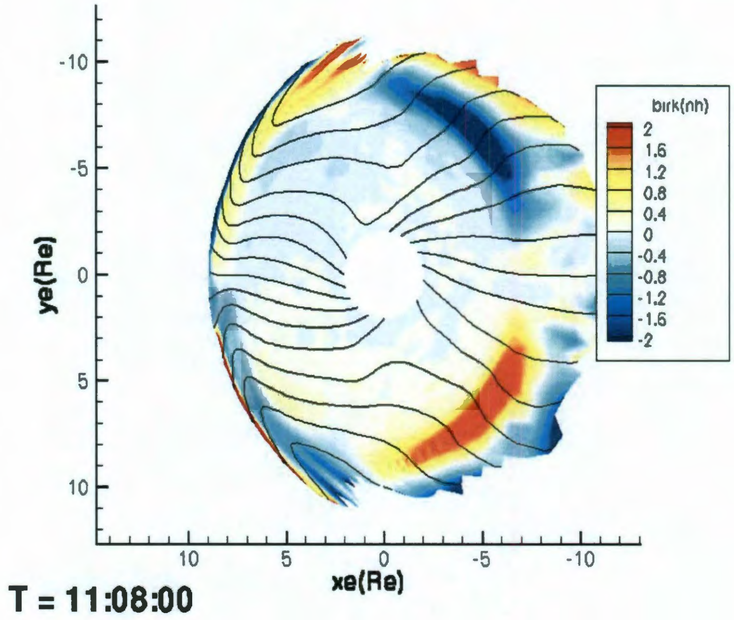

Figure 4.6 Birkeland currents in the RCM modeling region obtained using the direct integration method.

In principle, the currents shown in Figure 4.5 should differ from Figure 4.6 and 4.7 because of the inertial currents and the difference between the RCM-computed pressure and the nudged OpenGGCM pressure. Figure 4.6 and Figure 4.7 should be the same. Qualitatively they describe similar physics, but quantitatively they are different, because of numerical errors. This once again reminds us that we should always be careful with numerical results and always pay close attention to potential sources of errors.

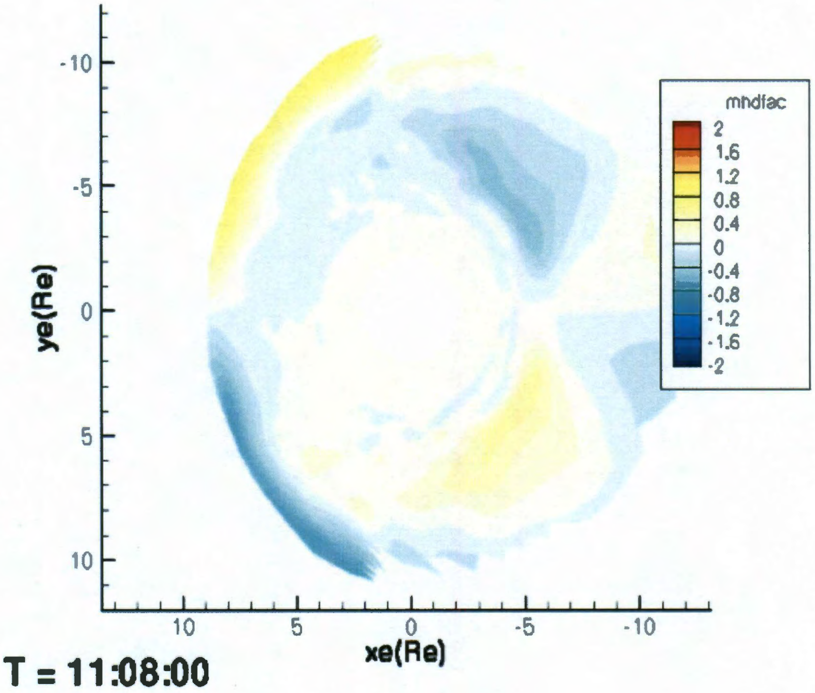

Figure 4.7 Birkeland currents that are calculated in the OpenGGCM using Ampere's law and then mapped onto the RCM grid.

4.4.3 Summary for OpenGGCM tests

Compared to the MHD currents, the new method consistently provides stronger region-2 currents which again suggest it could be applied to MHD models to improve their inner magnetosphere electrodynamics. Currents are overall much more noisy and resulting currents at lower-latitudes are less noisy than higher-latitude ones. There is a noticeable discontinuity at the open/closed boundary.

4.5 Tests using the Tsyganenko 96 magnetic field model

The tests with OpenGGCM models show some encouraging features in the resulting Birkeland currents but yet suggest that there are numerical concerns which might be resolution-related. However, the OpenGGCM has limited precision and grid resolution. In this section, tests with a Tsyganenko field model (T96) are presented in an attempt to address this issue, since the T96 model is in principle analytic so we can use this model to get an idea on what resolution is needed to resolve the complex 3D current structure and what other sources of error can contribute to the noisy currents.

4.5.1 The integrand $\frac{\nabla \bullet \vec{J}_\perp}{B}$ at different z planes

Figure 4.8 shows four z plane cuts of the integrand $\frac{\nabla \bullet \vec{J}_\perp}{B}$, calculated on a very fine grid so that it can be assumed that the contours show how $\frac{\nabla \bullet \vec{J}_\perp}{B}$ vary with z closely with what would be obtained theoretically using the T96 model. From $z = 0\ R_E$ to $z = 2\ R_E$, $\frac{\nabla \bullet \vec{J}_\perp}{B}$ decreases which confirms our assumption that the equatorial $\frac{\nabla \bullet \vec{J}_\perp}{B}$ should contribute most to the integral in equation (4.8). For $z > 2\ R_E$, the integrand near the Earth is close to zero. In T96, the magnetopause is a discontinuity and won't be resolved even using high resolution.

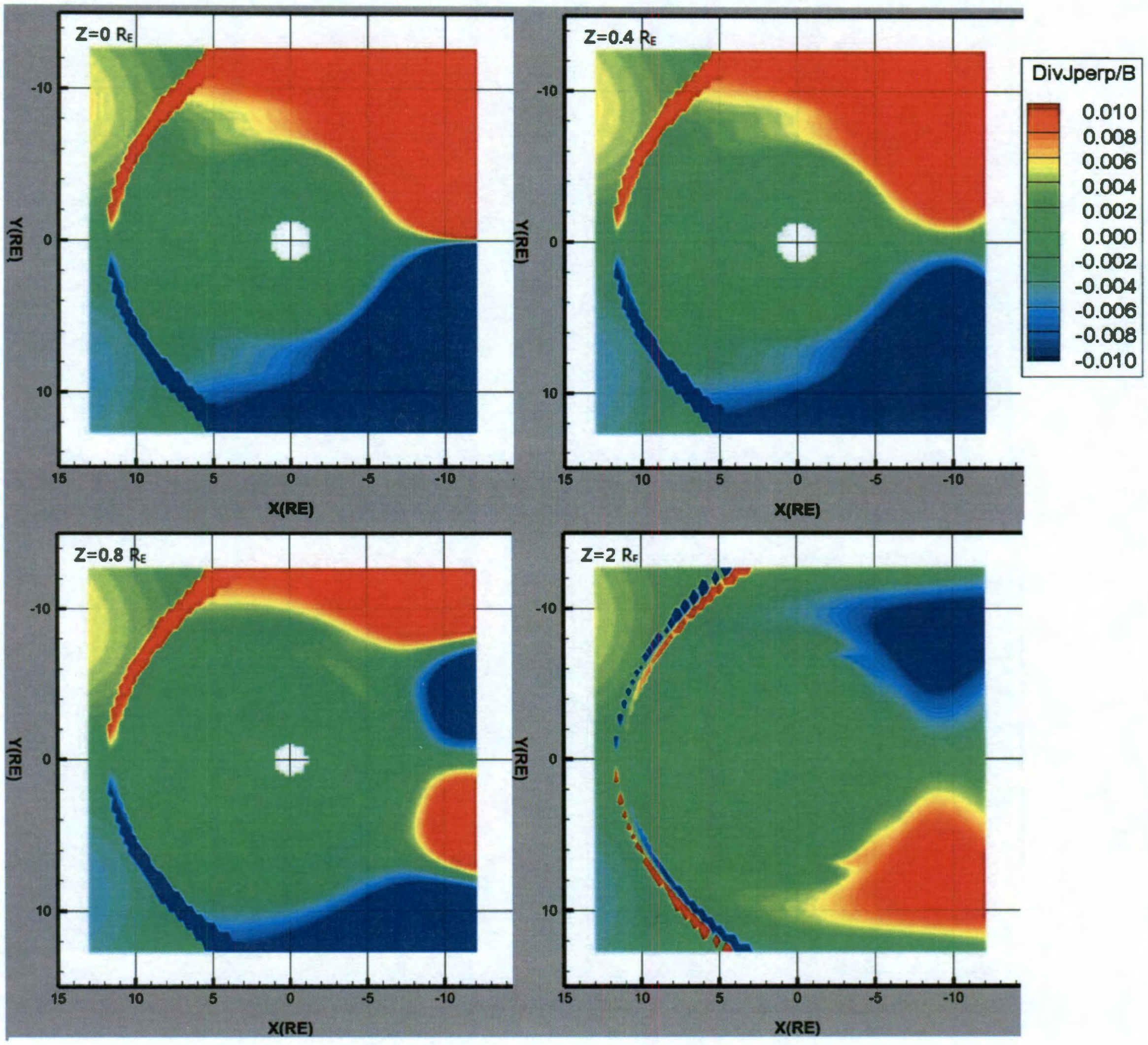

Figure 4.8 $\frac{\nabla\bullet\vec{J}_\perp}{B}$ cuts at z=0, 0.4, 0.8 and 2.0 R_E using the T96 magnetic field model on a very fine grid.

4.5.2 Effect of different grid resolutions on $\frac{\nabla\bullet\vec{J}_\perp}{B}$

The first row ((a) and (b)) of Figure 4.9 shows the integrand $\frac{\nabla\bullet\vec{J}_\perp}{B}$ at the $z = 4$ R_E plane with grid resolution $0.001R_E$ (a) and $0.1R_E$ (b). In the near Earth region, the results obtained using 0.1 R_E resolution exhibits a large amount of noise while the one with higher resolution does not. On the z=0 R_E plane, results from the two resolutions are similar. This may explains why the method worked better for currents that mapped to lower latitudes since the field-lines that originate from higher latitude are more likely to cross high z planes and pick up contributions from this artifact that are caused by insufficient resolution.

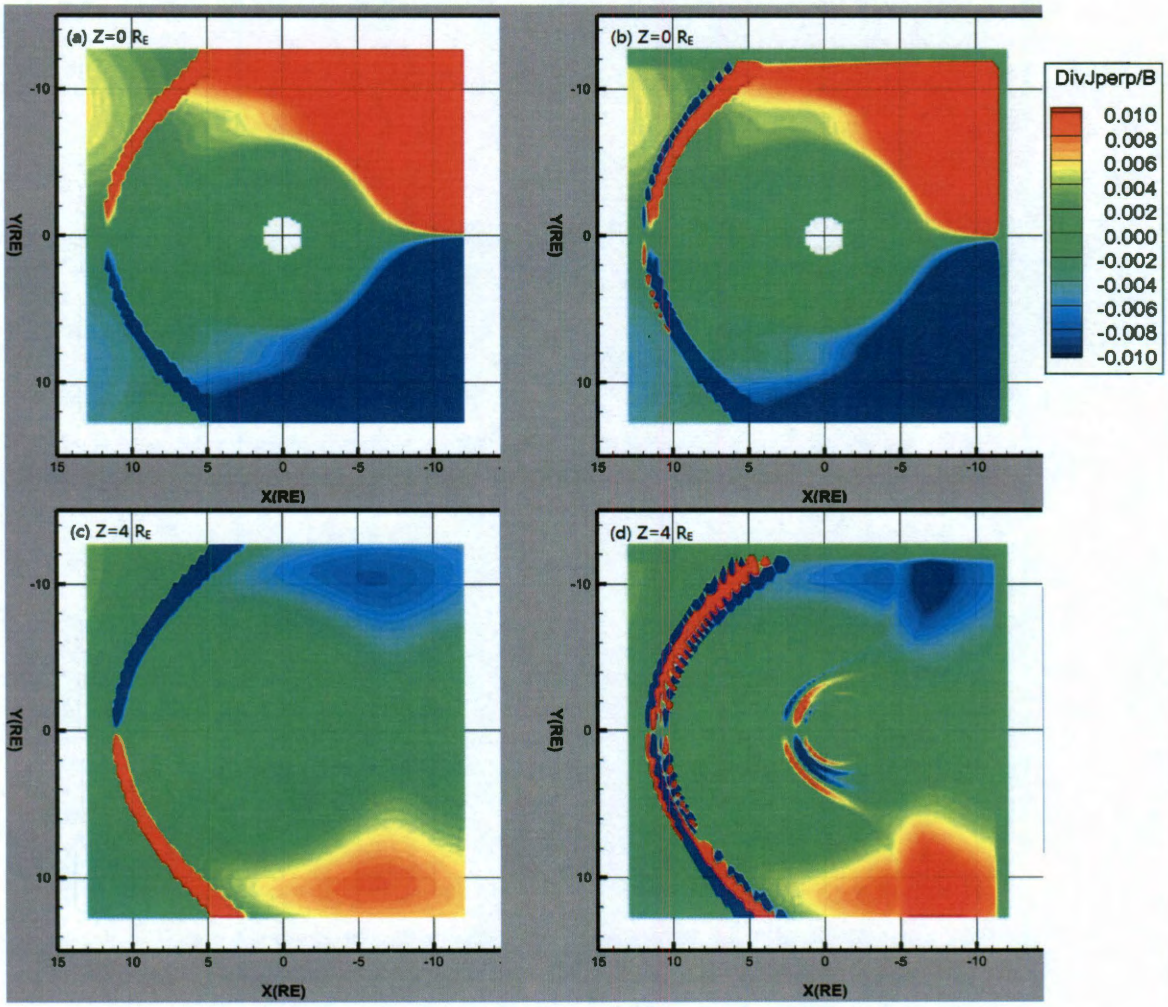

Figure 4.9 $\frac{\nabla\bullet\vec{J}_\perp}{B}$ at different z (0 or 4 R_E) and obtained using different resolutions ($0.1R_E$ for (a)(c) and $0.001R_E$ for (b)(d)).

The region with open field lines and near the open/closed boundary is difficult to resolve numerically since the field lines are congested spatially and a slight error in the direction of the 3D currents can lead to large errors in $\nabla\bullet\vec{J}_\perp$. For an example, we take a point in this region and do a grid-convergence test, the result is listed in table 4.1. This suggests the resolution of MHD codes should reach at least 0.01 R_E to properly resolve the divergence of the perpendicular currents. However this is only a one point test under one condition, higher resolution may be required at a different location or under different conditions.

Resolution (R_E)	J_x	J_y	J_z	$\nabla\bullet\vec{J}_\perp$
0.1	1.24	0.47	1.71	-6.41
0.01	1.86	0.28	1.77	-0.13
0.001	1.85	0.28	1.78	-0.15
0.0001	1.85	0.28	1.78	-0.15

Table 4.1 Grid-convergence test for a point in the polar cap at $z=4R_E$. Note the units for the currents are normalized.

For practical MHD runs, the highest resolution is in the order of 0.1 R_E which suggests that more resolution is needed to have the new method accurately compute for $\nabla\bullet\vec{J}_\perp$ inside and near the open/close boundary. In addition, for the case of 0.001 R_E resolution double precision should be used to reduce truncation error. The amount of computational resources required to run the MHD codes with this kind of resolution is quite demanding even on larger supercomputers, however simulation with this kind of resolution are certainly possible in the next few years.

4.5.3 Other possible errors

While $\frac{\nabla\bullet\vec{J}_{\perp}}{B}$ can be resolved given enough resolution, interpolation and tracing are also performed to obtain the Birkeland currents in the new method. These extra calculations could be other sources of errors.

Figure 4.10 shows Birkeland currents obtained using Ampere's law by taking the parallel component of the curl of the T96 magnetic field at 4 R_E (OpenGGCM usually takes the current at 4.5 R_E) using a $0.0001R_E$ uniform resolution grid. This current distribution can be assumed to resemble the theoretical Birkeland currents distribution in T96. If a coarser grid is used, the currents obtained using Ampere's law become more diffusive. Figure 4.11 and Figure 4.12 shows Birkeland currents obtained using Ampere's law using grid spacings of $0.3R_E$ and $0.8R_E$. This again shows the MHD's diffusive Birkeland currents are partly due to resolution issues.

Figure 4.13 is the Birkeland currents distribution obtained using the new method with a grid spacing of 0.1 R_E for the current divergence calculations. $\nabla\bullet\vec{J}_{\perp}$ is then stored onto the same OpenGGCM grid mentioned in 4.41. In section 4.5.2, we have stated that $\frac{\nabla \bullet \vec{J}_\perp}{B}$ cannot be well resolved at certain regions using this resolution (0.1 R_E). Noisy structures present in the region-1 currents but the region-2 currents are comparable to the ones in Figure 4.10.

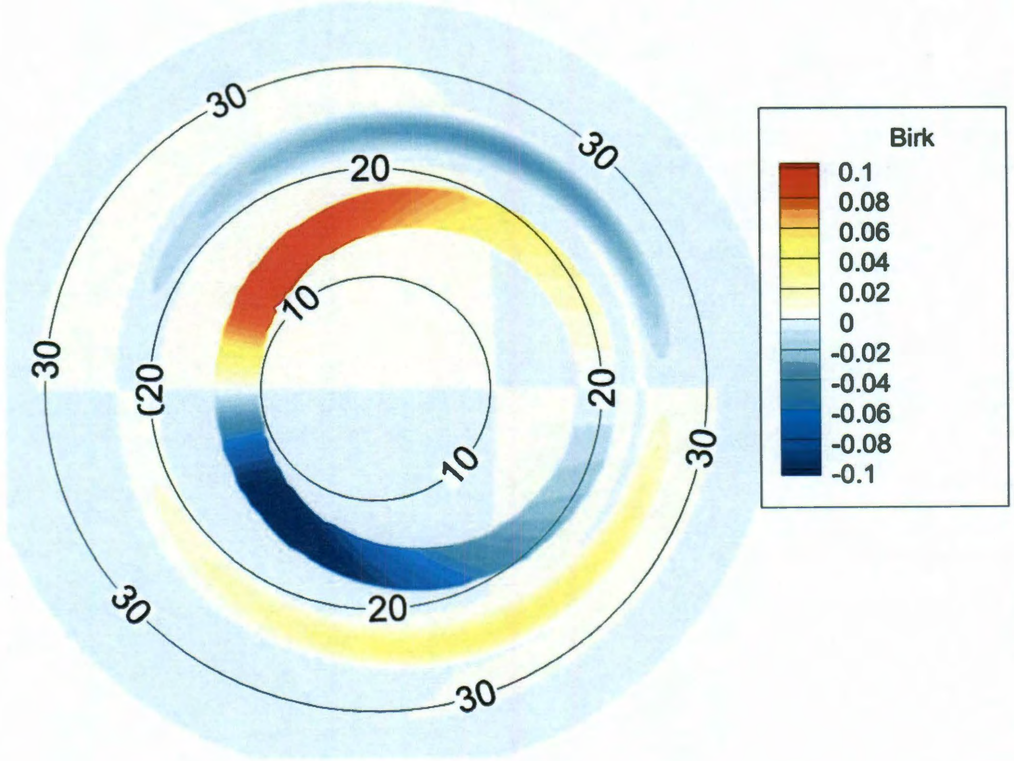

Figure 4.10 Birkeland currents obtained using the Ampere's law method for the T96 magnetic field (grid spacing 0.0001R_E).

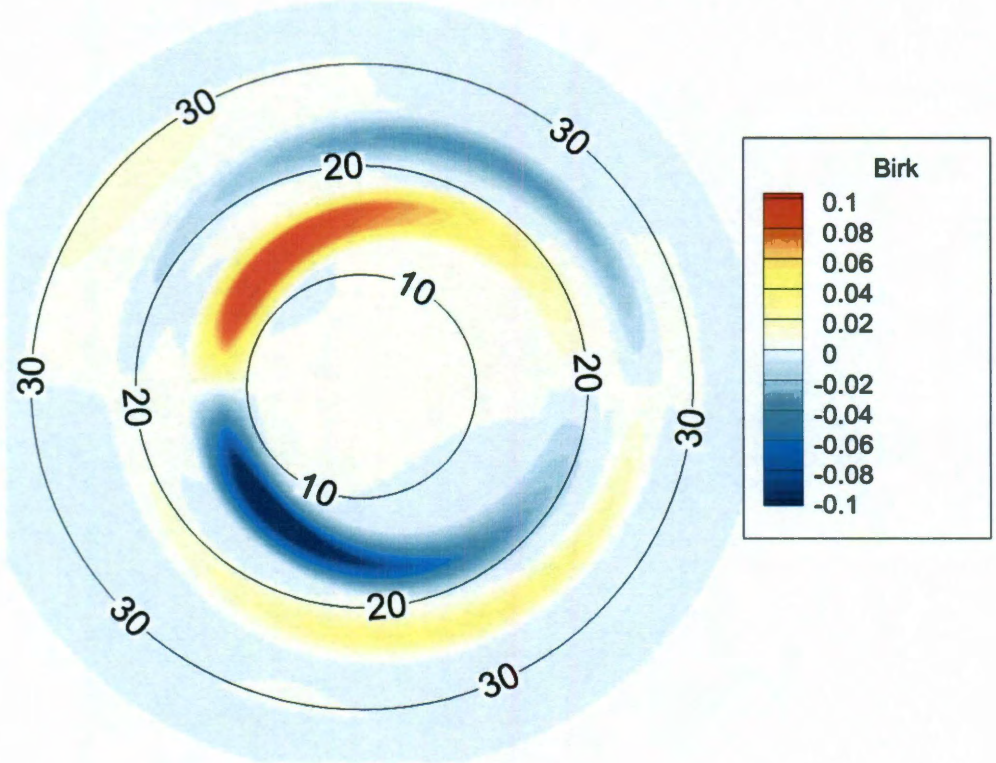

Figure 4.11 Birkeland currents obtained using the Ampere's law method for the T96 magnetic field (grid spacing $0.3R_E$).

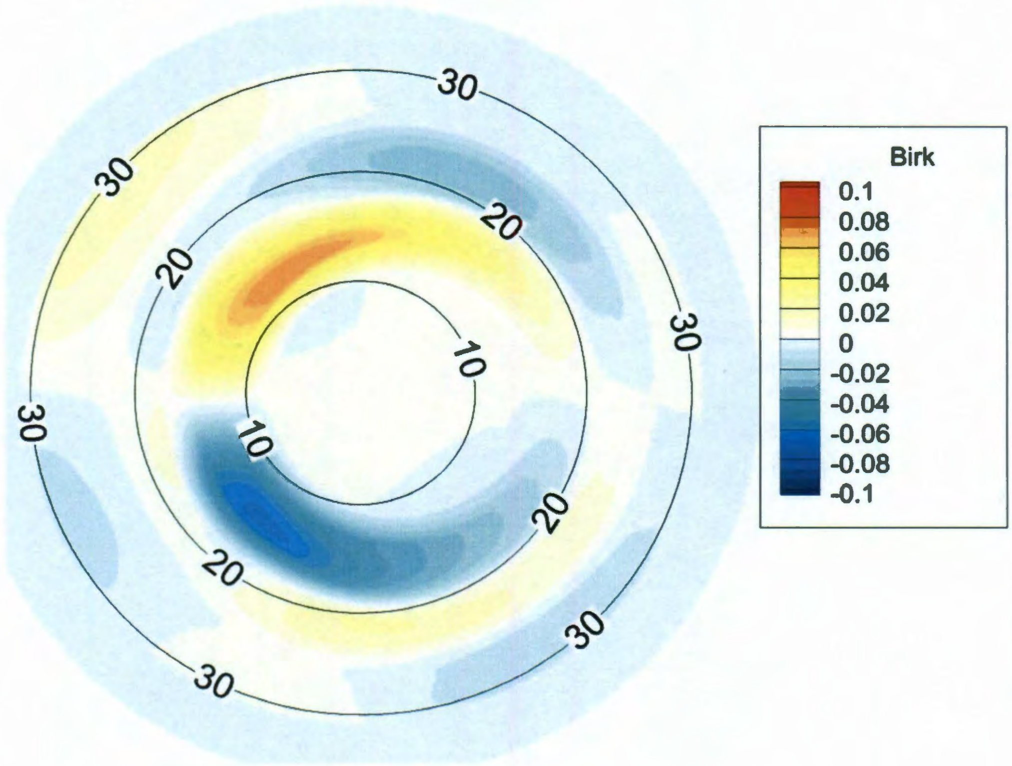

Figure 4.12 Birkeland currents obtained using the Ampere's law method for the T96 magnetic field (grid spacing $0.8R_E$).

Figure 4.14 represents the direct-integrated Birkeland currents using $0.0001R_E$ grid spacing. A lot of the numerical artifacts shown in Figure 4.13, which were due to insufficient resolution, are gone. However the region-1 currents shown in Figure 4.14 still do not match Figure 4.10. Errors in the field line tracing could introduce numerical artifacts. For example, the dayside ionospheric grid points that have the current anomalies are on closed field lines but have $\frac{\nabla \bullet \vec{J}_\perp}{B}$ contributions from grid points inside the magnetopause. The nightside current spots could also be corresponding to tracer picking up boundary currents in T96. *Zheng* [2011] argued that field line tracing is very sensitive to the tracing method and it is generally hard to accurately trace a long curved field line. Thus the accuracy of the new method also depends on the accuracy of the tracing. In addition, interpolation of $\frac{\nabla \bullet \vec{J}_\perp}{B}$ during the tracing could also introduce errors.

These T96 tests suggest the noise seen in Figure 4.2 and Figure 4.4 are introduced by insufficient resolution and tracing (e.g. mapped a ionospheric point through a boundary), which are hard to eliminate. However the low latitude currents are well resolved using the new method which produces a much stronger region-2 currents than MHD (Figure 4.6 and 4.7). One possible compromise is to use the Ampere's law for high latitude regions and only use the new method for low latitude regions.

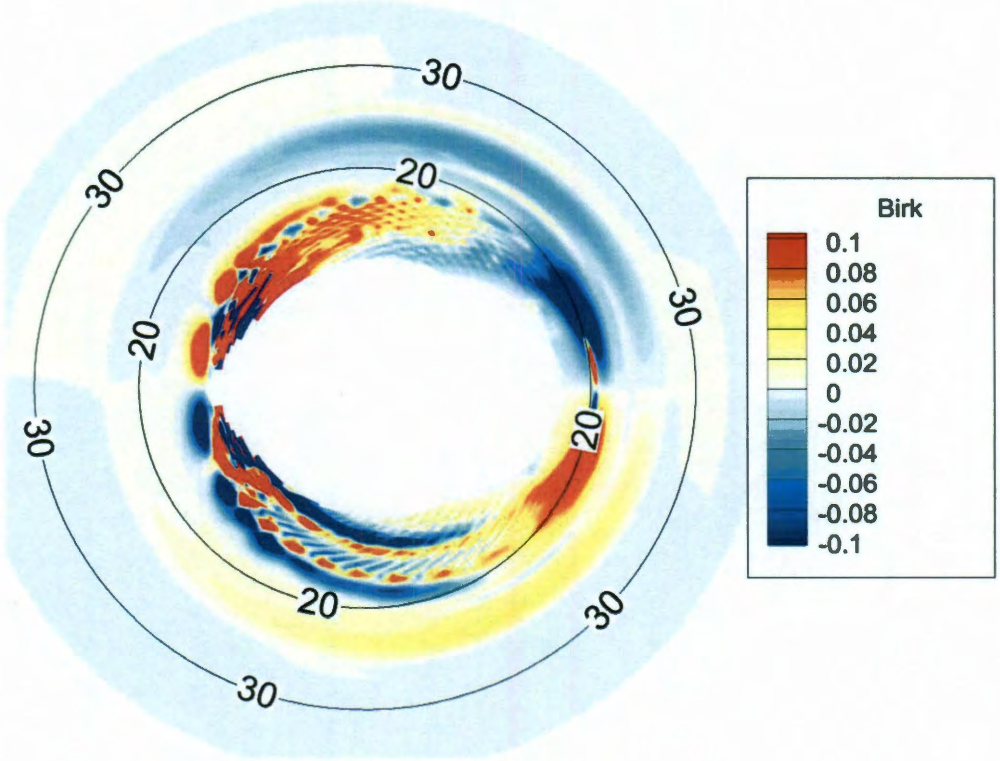

Figure 4.13 Birkeland currents obtained using the direct integration method for the T96 magnetic field (grid spacing $0.1R_E$).

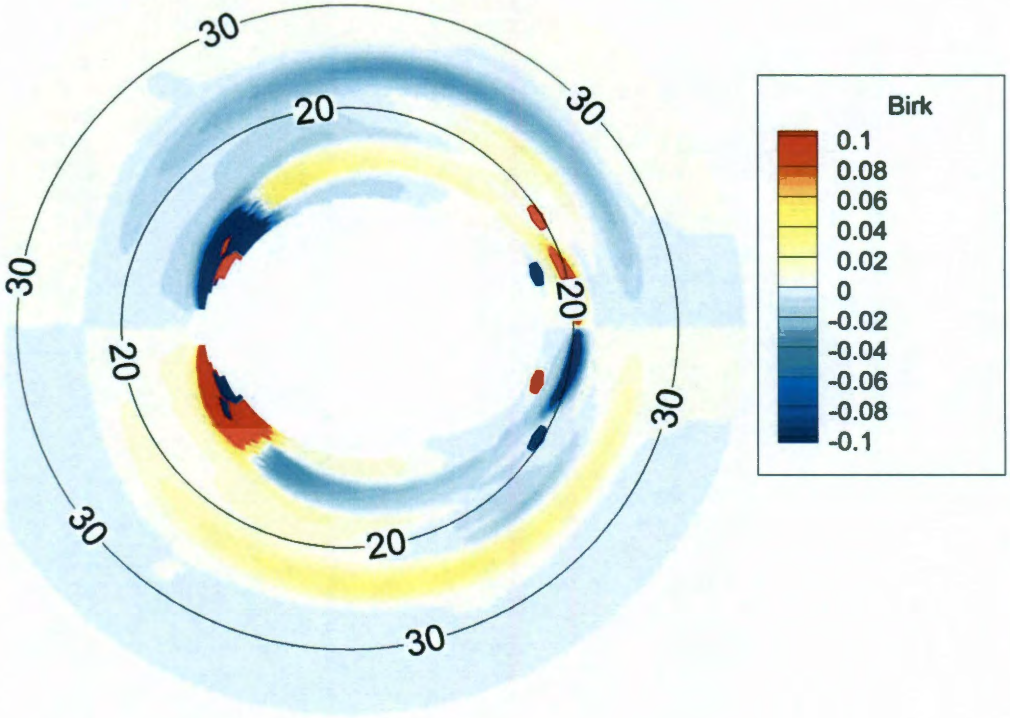

Figure 4.14 Birkeland currents obtained using the direct-integration method for the T96 magnetic field (grid spacing 0.0001R_E).

4.6 Summary

This chapter presented a proposed direct integration method to compute the Birkeland currents from MHD magnetic field as well as results from some preliminary tests. The direct-integration approach is promising and could be used in MHD codes to better resolve the region-2 currents and add inertial effects to the RCM, especially in coupled runs where the tracing of field lines is done on a frequent basis. However, the approach is limited by the grid resolution, inaccuracy in field line tracing and by the overall code precision of the MHD code. One practical compromise is to utilize this method for the lower latitude grid points (region-2 currents) but use the original Ampere's law method for higher latitude ones.

The T96 tests suggest the noise introduced by using the new method is due to insufficient resolution and tracing errors, which could be improved by using a more sophisticated tracing scheme. The Ampere's law method gives satisfactory results when the grid resolution is fine but the region-2 currents are diffuse when resolution is coarse. These tests are preliminary and more comprehensive tests should be carried out to determine the accuracy of the direct-integration method even for the low-latitude currents. Further comparisons of the three methods (direct integration, Vasyliunas equation, Ampere's law) could be carried out using better analytical magnetic fields with equilibrium pressure on a very high resolution grid.

Chapter 5

Consequences of violation of frozen-in-flux - evidence from OpenGGCM simulations

It is widely believed that, during a substorm, plasma instabilities occur before the onset of magnetic reconnection, signaling the end of the growth phase. Despite many years of effort, however, the details of how the instability and the onset of reconnection develop from closed field line configuration with finite normal magnetic field are not well understood. In this chapter, we study an idealized simulation of a substorm that occurred on March 23, 2007, motivated by the study in Chapter 2 and the paper by *Yang et al.*, [2011]. Our analysis emphasizes the time development of the distribution of the entropy parameter and its convective time derivative, which should be zero in ideal MHD. In the late growth phase, the simulation exhibits, over a range of local times, a systematic violation of conservation of entropy that corresponds to what is called "antidiffusion". Out of this background, a more localized disturbance develops in a region of high magnetic stretching, resulting in formation of a strong reduction of entropy (bubble) earthward of a local enhancement (blob). The process is accelerated when the current density exceeds a threshold for triggering an explicit resistivity in the code. The bubble moves earthward and the blob tailward, which leads to a reduction of the normal magnetic field and a thinning of the current sheet between them, making the magnetospheric configuration more conducive to tearing and other instabilities (We do not address specifically which instability has occurred). This positive feedback gives rise to increased violation of the perfect-conductivity relation and eventually reconnection.

5.1 Introduction

Many authors have suggested that instabilities occur before the onset of substorm expansion phase that may change the magnetotail to a more favorable configuration for magnetic reconnection (see reviews by *Lui* [2004], *Cheng* [2004], and *Pritchett.* [2007]). However, the details on how reconnection arises from an initial closed-field-line configuration with finite normal magnetic fields are a matter of longstanding controversy, as reviewed briefly by *Sitnov and Schindler* [2010]. (In this study, we use Vasyliunas' [1975] definition of reconnection in terms of plasma flow across a separatrix between field lines of different topology. However, as the separatrix may not be easily identifiable until lobe reconnection starts, we will say specifically that reconnection has occurred if and only if the magnetic field crosses the center of the cross-tail current sheet in both directions. Thus reconnection, in our definition, is required to produce the helical field lines that can occur in the plasma sheet in the presence of finite B_y.)

Recently *Yang et al.* [2011] shed light on initiation of reconnection starting from a closed-field-line plasma-sheet configuration by using the RCM-E (Rice Convection Model – Equilibrium) to simulate an idealized substorm growth phase in which they imposed up a local reduction of $pV^{5/3}$ (where p is the pressure and V is the flux tube volume $\int ds/B$) forming a bubble just earthward of a local enhancement of $pV^{5/3}$ (blob) at the end of a substorm growth phase [*Zhang et al.*, 2008; *Wolf et al.*, 2009]. The bubble and blob were assumed to be created by unspecified mechanisms that violated the local frozen-in-flux condition. *Yang et al.* [2011] found that the bubble moves earthward and the blob surges tailward. In the region between them, the current sheet thins and the normal magnetic field decreases. Because of that, *Yang et al.* suggested that the creation of a bubble/blob pair in the RCM-E simulation leads to a magnetospheric configuration that is more conducive to tearing. However, because of the slow-flow and quasi-static equilibria assumptions used in the RCM-E [*Wolf*, 1983], the simulations used by *Yang et al.* [2011] have two limitations: (1) the inertial term in the momentum equation is neglected and (2) the process of reconnection is not represented in the model. Here we present MHD simulations that have neither of these limitations and so add a useful additional computational test of the ideas presented by *Yang et al.* [2011].

As in the *Yang et al.* [2011] study, the MHD code does not specifically model any potential non-MHD micro-scale mechanisms that lead to the violation of frozen-in-flux.

In the OpenGGCM MHD code, the frozen-in-flux condition can be locally violated in one of two ways. The first is numerical diffusion, in which finite grid discretization inevitably gives rise to errors in the second-order derivatives of the magnetic field, creating numerical dissipation. The second mechanism that operates in the OpenGGCM takes the form of a built-in explicit anomalous resistivity which is triggered when the normalized current density exceeds a specified threshold [*Raeder et al.* 1998]. The anomalous diffusion caused by the anomalous resistivity is on the scale of grid cell and is usually large when it is activated; however observations suggest even stronger diffusion in the tail [e.g. *Cattell et al.* 1996]. In either case, either mechanism might be expected to produce field-line slippage in the region with numerical or anomalous resistivity, resulting in plasma transport from one flux tube to the other, violating the frozen-in-flux condition, and creating a bubble and a blob [Figure 1 in *Yang et al.* 2011].

In this chapter, we will present detailed results from an idealized OpenGGCM MHD simulation, based on a substorm event that occurred on March 23rd, 2007 – an event that has been studied by *Raeder et al.* [2008], *Zhu et al.* [2009], *Hu et al.* [2010] and *Raeder et al.* [2010] using realistic solar wind and IMF input. We show that a bubble-blob pair forms naturally in the simulation and discuss the reason for their formation. The results of this study, along with the RCM-E results [*Yang et al.*, 2011], further support the idea that the bubble-blob mechanism contributes importantly to the start of reconnection near the onset of the substorm expansion phase.

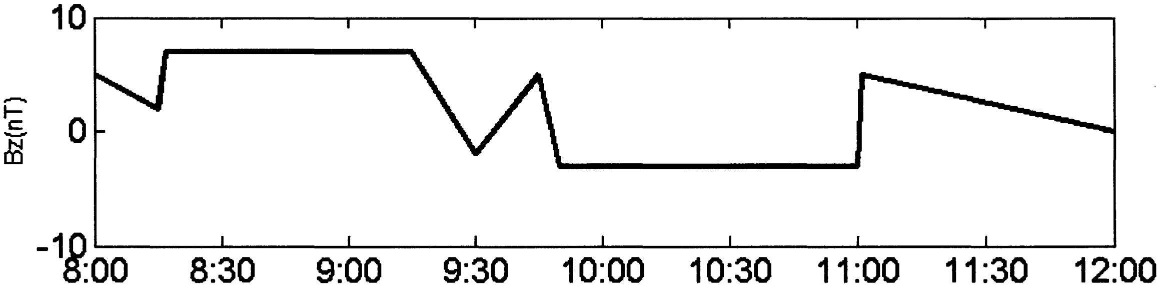

Figure 5.1 IMF *Bz* input for the OpenGGCM simulation (shifted to sunward simulation boundary).

5.2. The OpenGGCM simulation

OpenGGCM is a large-scale model of the Earth's magnetosphere which has been described in previous chapters ([*Raeder*, 2003] and [*Raeder et al.* 2008]). For the runs presented here, we used a grid resolution, in the *x*, *y* and *z* directions, of 630x300x200 with the smallest grid spacing at ~0.15 R_E. The CTIM module [*Fuller-Rowell et al.*, 1996] in OpenGGCM was used for ionospheric conductance calculations. The solar wind inputs for the OpenGGCM were smoothed and simplified versions of the actual data from the WIND satellite (at ~198 R_E sunward) but with *Bx, By Vy,* and *Vz* set to zero to make the results easier to visualize. The simplified time variation of the interplanetary magnetic field (IMF) *Bz* component at the sunward boundary is shown in Figure 5.1. The solar wind density is constant at 15 particles/cc, until it jumps to 20 particles/cc at 11:00. The solar wind velocity V_x is held constant at 300km/s. The dipole tilt is set to zero for simplicity.

This study focuses on analyzing MHD results using an entropy parameter similar to $pV^{5/3}$. Two technical points require discussion:

In simulations with the RCM-E, which assumes a series of configurations that are in force equilibrium, *Yang et al.* [2011] focused on the parameter $pV^{5/3}$, which is constant in adiabatic expansion or compression of an ideal monatomic gas. In full MHD, with inertial terms present, pressure is not constant along field lines, and the generalization of $pV^{5/3}$ is $S^{5/3}$, where

$$S = \int p^{3/5} ds / B = \int \left(\frac{p^{3/5}}{\rho} \right) \frac{\rho \, ds}{B} \tag{5.1}$$

[*Birn et al.*, 2009]. Under conditions of frozen-in flux, the quantity $\rho ds / B$, which is an element of mass along the flux tube, should be conserved as the element moves. The parameter $p^{3/5} / \rho$ is equal to $(1/C)\exp(\sigma / R)$, where C and R are constants, and σ is entropy per unit mass defined as $R \ln(Cp^{3/5} / \rho)$ [*Birn et al.*, 2009]. Thus $p^{3/5} / \rho$ is conserved as a mass element moves in ideal MHD, because entropy is conserved. Of course, $S^{5/3}$ is equal to $pV^{5/3}$ in the special case where pressure is constant along a field line, and we will focus on $S^{5/3}$ in our MHD-based study.

In ideal MHD,

$$\frac{DS^{5/3}}{Dt} = \frac{\partial S^{5/3}}{\partial t} + \mathbf{v} \cdot \nabla S^{5/3} = 0 \tag{5.2}$$

where **v** is the flow velocity. When the frozen-in-flux condition is violated, we will still use flow velocity to calculate $\frac{DS^{5/3}}{Dt}$ as a diagnostic parameter; in this case $\frac{DS^{5/3}}{Dt}$ would be non-zero. Since $S^{5/3}$ is constant along a field line we can display it or $DS^{5/3}/Dt$ on any surface that cuts all of the field lines considered. It is easiest to visualize equation (2) if the surface is defined such that the gradient is parallel to the surface, so that we can consider only the velocities on that surface. For the present runs, the dipole is untilted, and the boundary conditions have north-south symmetry, so the equatorial magnetic field should be exactly perpendicular to the equatorial plane, and $\nabla S^{5/3}$ should be in the plane. However, this symmetry condition is not built into the numerical procedure and is consequently not exactly satisfied, i.e. in certain regions the equatorial Vz is not exactly zero. To account for the non-zero Vz, in the calculation of $\frac{DS^{5/3}}{Dt}$, we made certain corrections to **v** in equation (5.2), as described in the Appendix. The effect of the correction is very small for regions of interest and is only visible for a limited region ($x <$ -16 R_E, $4 < y < 6$).

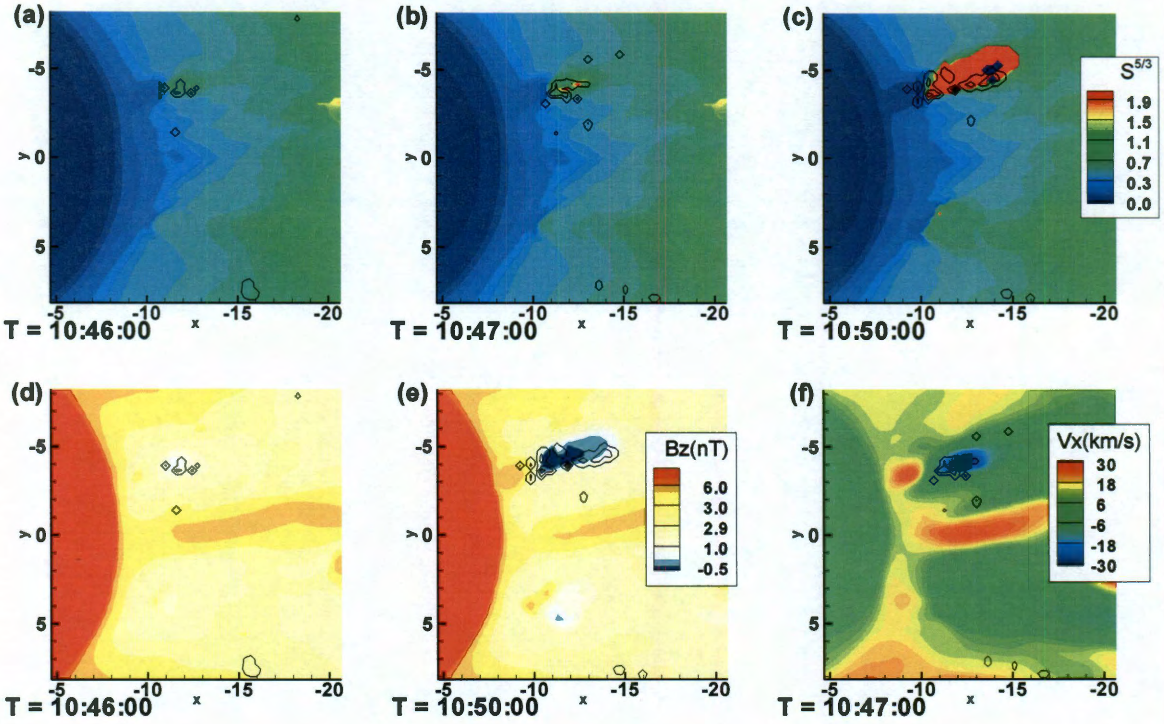

Figure 5.2 (a-c) Equatorial values of $S^{5/3}$ for times 10:46, 10:47 and 10:50. (d-e) B_z on the equatorial plane for 10:46 and 10:50. (f) flow velocity in x direction for 10:47. The black closed loops on the $S^{5/3}$ plots indicate where the anomalous resistivity is non-zero.

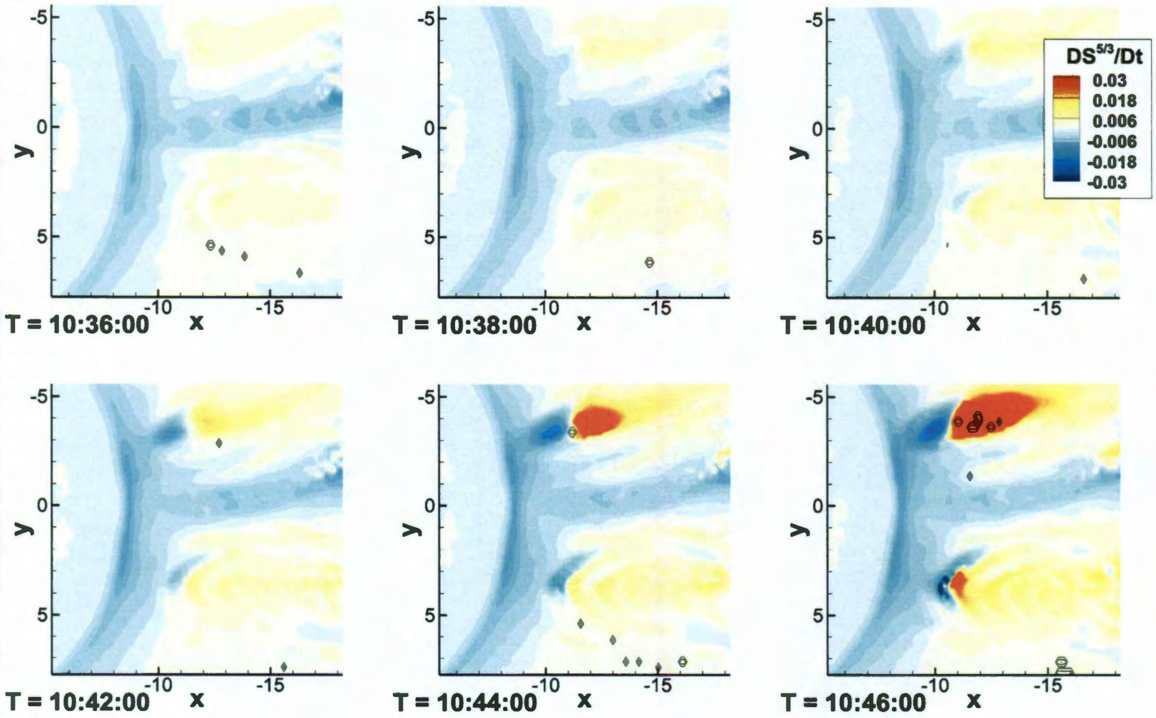

Figure 5.3 Equatorial $DS^{5/3}/Dt$ values for six different times 10:36, 10:38, 10:40, 10:42, 10:44 and 10:46.

5.2.1 Bubble-blob pair and numerical accuracy issues

In the simulation, the IMF turns southward at ~10:00UT and turns northward at ~ 11:00UT at the sunward simulation boundary. In this study, we focus on the period near the end the growth phase 10:35-10:50UT. Before 10:30UT, the MHD simulation shows a classic growth phase picture with field line stretching. Panels a-c of Figure 5.2 show plots of $S^{5/3}$ in the z=0 plane at times 10:46, 10:47, 10:50. Panels (d) and (e) show two snapshots of the z component of the equatorial magnetic field at 10:46 and 10:50. Note that the blue areas represent $B_z<0$, which indicates that reconnection has occurred. Areas with negative equatorial B_z but positive values for $S^{5/3}$ indicates presence of helical field lines. (f) shows the flow velocity in the x direction. The black closed loops on the $S^{5/3}$ plots indicate where the anomalous resistivity is non-zero.

One clear feature of Figures 5.2d and 5.2e is a channel of earthward flow near local midnight, and Figures 5.2a and 5.2b indicate a slight reduction of $S^{5/3}$ in that region. This feature is reminiscent of the flow channels suggested by *Sergeev and Lennartsson* [1988]. A more interesting feature is a bubble-blob pair that develops east of local midnight, which we will discuss in detail. (A similar feature develops before midnight a few minutes later, but our discussion will focus on the postmidnight feature.)

Figure 5.3 shows $DS^{5/3}/Dt$ for six times during the simulation. If the code were solving the ideal-MHD equations exactly, then $DS^{5/3}/Dt$ would be zero everywhere except inside the closed black curves, where the resistivity is explicitly set equal to positive values. Obviously, that is not the situation, and most of the nonzero values shown in Figure 5.3 are a result of numerical diffusion. To understand better what is happening in the code at 10:40, we display separately in Figure 5.4 (a-b) the $\partial S^{5/3}/\partial t$ and $\mathbf{v}\cdot\nabla S^{5/3}$ terms in equation (2), respectively. Figure 5.4(c) shows $S^{-5/3}\dfrac{DS^{5/3}}{Dt}$, which is the percentage change of $S^{5/3}$ per minute. In the injection channel near midnight,

$\left|\mathbf{v}\cdot\nabla S^{5/3}\right| >> \left|\partial S^{5/3}/\partial t\right|$, presumably because of the relatively large flow velocities and the tailward gradient of $S^{5/3}$. The two terms in (5) do not balance because of the tendency of MHD codes to numerically diffuse pressure from the high-pressure region in the inner plasma sheet toward the lower-pressure region further out. However, *Lee et al.* [1995] suggested the existence of a physical mechanism that acts in the same direction.

The most interesting feature in Figures 5.3 and 5.4 is in the region centered about (-11, -3), where Figure 5.2 indicates the formation of a bubble and a blob. In this feature, which is narrow in local time, there is a region where $\partial S^{5/3}/\partial t$ and $DS^{5/3}/Dt$ are both negative, indicating the creation of a bubble through violation of the adiabatic condition. Tailward of the bubble is a region where $\partial S^{5/3}/\partial t$ and $DS^{5/3}/Dt$ are both positive, indicating the creation of a blob. In the bubble/blob region the $\partial S^{5/3}/\partial t$ term dominates in $DS^{5/3}/Dt$, as shown in Figure 5.4.

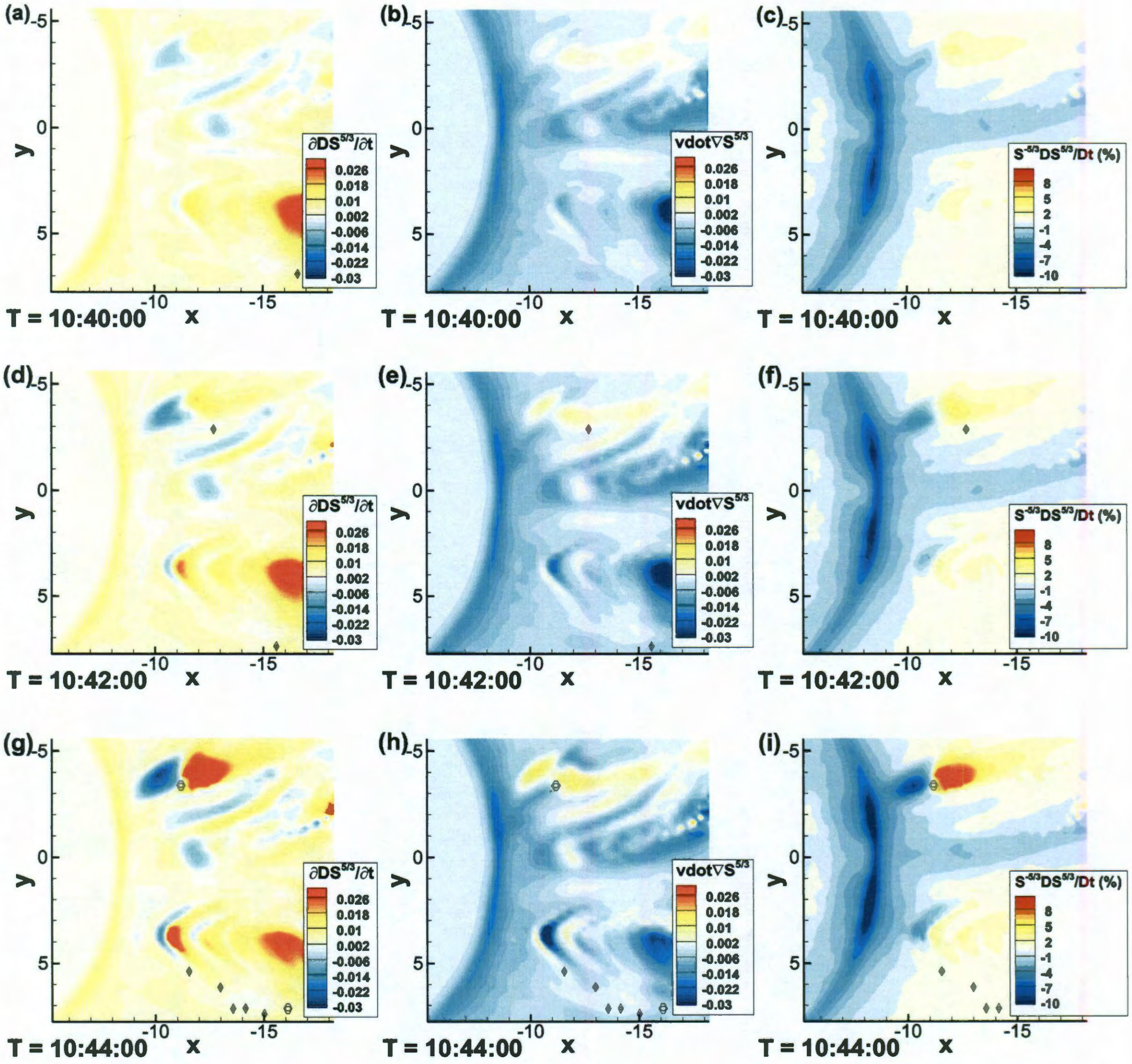

Figure 5.4 Equatorial values of $\partial S^{5/3}/\partial t$, $(\mathbf{v}_2\cdot\nabla)S^{5/3}$ and $S^{-5/3}\dfrac{DS^{5/3}}{Dt}$ (per minute) for 10:40, 10:42 and 10:44.

Figures 5.5 and 5.6 show the development of the bubble-blob pair in more quantitative detail. They show the variation of several physical parameters along the approximate centerline of the bubble/blob pair, which we estimate as

$$y = \frac{x}{3} - 0.24$$

The two interesting features are:

1. The situation before 10:37 is characterized by $DS^{5/3}/Dt<0$ centered at about x=-9 and $DS^{5/3}/Dt>0$ centered around x=-11 R_E. Those features, which cover a fairly wide range of local time in the postmidnight sector, are of numerical origin in the code and represent numerical antidiffusion in S. It is called "antidiffusion" because the gradient of S usually points tailward and this diffusion in pressure makes the gradient of S stronger. These features grow in time, slowly but steadily. Figure 5.6a indicates that an increasingly deep magnetic field minimum forms around x=-11 R_E. It represents essentially the antidiffusion behavior predicted by *Lee et al.* [1995]. The Dv_x/Dt plot in Figure 5.5 indicates that there is very little acceleration associated with this antidiffusion. At 10:46, although the bubble and blob pair is well formed, the earthward and tailward flow is not strong, with a peak x velocity at ~ 20 km/s. The diffusion in pressure is not noticeable until 10:46, as shown in Figure 5.5.

2. Beginning about 10:38, $DS^{5/3}/Dt$ begins to decrease at about x=-10.8 on the centerline, and that feature rapidly becomes sharp. $DS^{5/3}/Dt$ increases tailward of x=-11.2. Figure 5.3 indicates that this rapidly developing feature is quite narrow in local time. A bubble and blob form. Acceleration also builds up at approximately the same time – earthward in the bubble and tailward in the blob.

The physical mechanism by which the bubble and blob could form in nature is illustrated in Figure 5.7. In the 2D stretched-closed-field-line configuration shown in Figure 5.7a, suppose that the current density exceeds a threshold for generation of anomalous resistivity in the gray region. Then the electric field in the rest frame of the plasma is in the direction of the current (+y), and field line 2 slips earthward (x-direction) through the plasma, reaching the configuration shown in Figure 5.7b. The magnetic field between lines 2 and 3 consequently strengthens, and the field between 1 and 2 weakens. The net force per unit volume can be written

$$\mathbf{f} = -\nabla p_{tot} + \frac{(\mathbf{B}\cdot\nabla)\mathbf{B}}{\mu_o} \tag{5.3}$$

where p_{tot} is the total pressure (particle + magnetic). If the region of slippage is thin in the y-direction, as is the case in Figure 5.2, then p_{tot} in the slip region is approximately the same as in the adjacent background, which is assumed to be in equilibrium ($\mathbf{f}$=0). The magnetic field in the bubble is stronger than in the background, and the same is true of the earthward tension force in the bubble. Therefore, the bubble feels a net earthward force. By the same kind of argument, the blob feels a tailward force. Note that in Figure 5.6, the Bz component in the bubble region is increasing for 10:46 and 10:47, despite the overall decreasing trend in Bz.

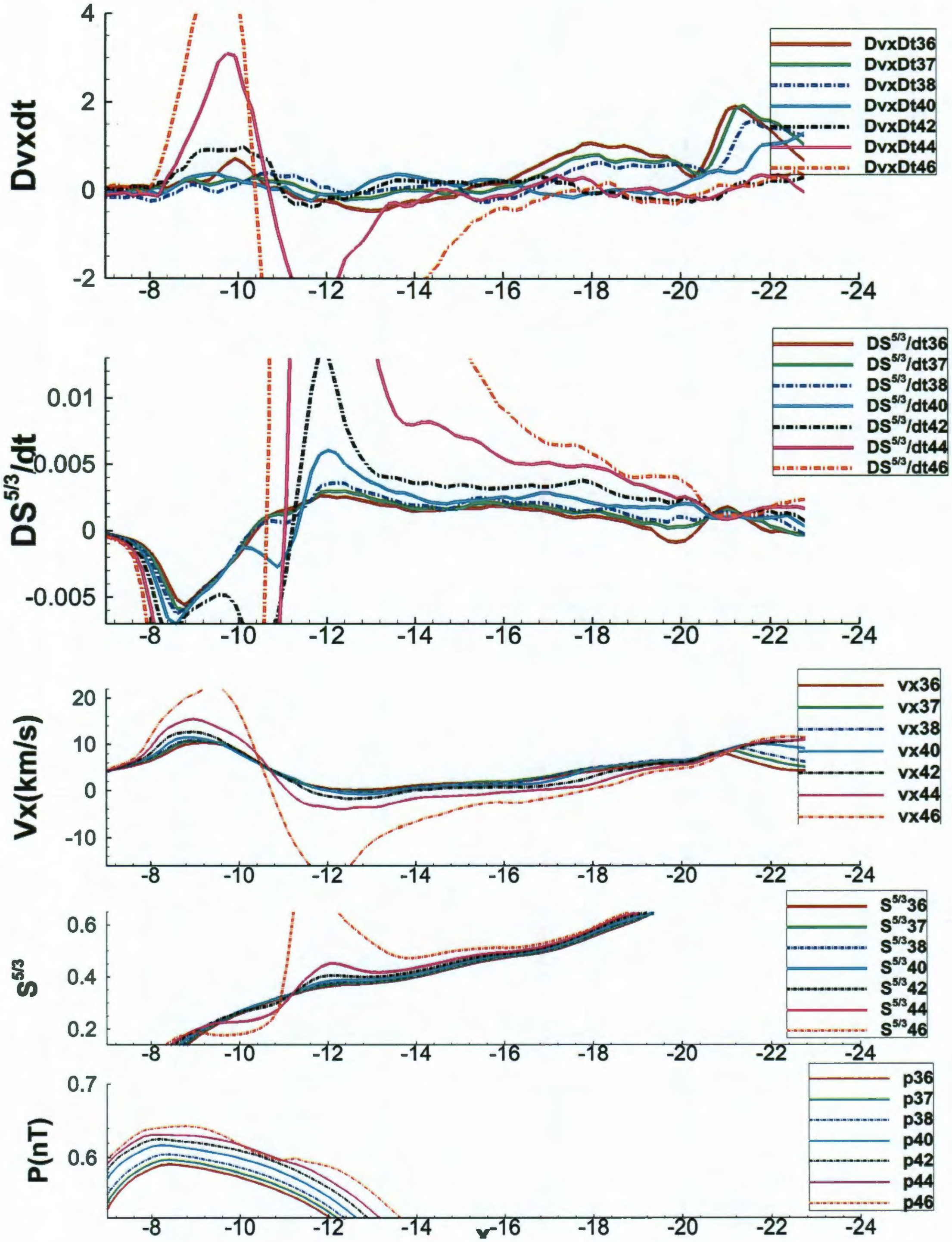

Figure 5.5 Dv_x/Dt, $DS^{5/3}/Dt$, v_x, $S^{5/3}$ and pressure along the centerline of the bubble-blob pair vs. x in the equatorial plane, for the times indicated.

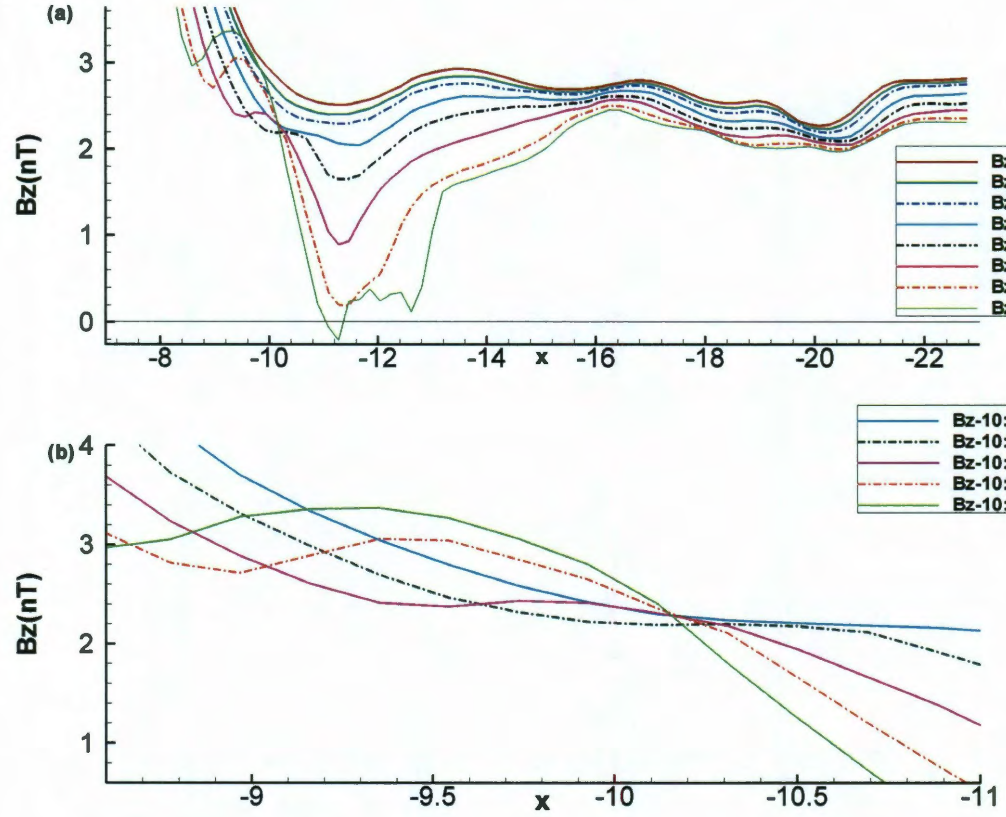

Figure 5.6 (a) B_z along the centerline of the bubble-blob pair vs. x in the equatorial plane, for the times indicated. (b) Zoomed in version of (a) to show the bubble.

One of the basic questions about how tearing can occur, starting from a configuration with finite magnetic field normal to the current sheet, is whether the same basic process that created a localized neutral-sheet region from the $B_z>0$ configuration is essentially the same as the mechanism that allows reconnection to proceed as in the classic reconnection geometry of Figure 5.7c. There is a resemblance between the situations in Figures 5.7b and 7c. In 7b, strengthened tension force pulls the bubble on the earthward side toward the earth, and weakened tension force on the tailward side pulls the blob tailward. In Figure 5.7c there is earthward tension force on the earthward side of the neutral point, and tailward tension force on the tailward side. Both processes result from changes in the magnetic tension force.

5.2.2 The role of anomalous resistivity

In order to investigate the role of the anomalous resistivity in the formation of the bubble-blob pair, we have done two further runs, one that has the explicit resistivity completely turned off (the first row of Figure 5.8) and the other in which the explicit resistivity turned on until 10:00 (and turned off afterwards) so that the system evolves to the exact same condition as in the original run at 10:00. This allows for easier comparison (the second row in Figure 5.4).

For the run without explicit resistivity, we still see the formation of the bubble and blob at the end of the growth phase, suggesting that numerical resistivity plays a role in their formation. These results suggest that a similar bubble/blob feature may also be reproduced by other global MHD models that have no explicit resistivity. However, the anomalous resistivity does play an important role in the process. In the run with explicit resistivity turned off, the formation of the bubble and blob occurs later than in the run with resistivity turned on, so that the growth of the instability is slower. For the run with explicit resistivity turned off at 10:00, the blob also appears later and more weakly than the original run. That is, the field-line slippage may begin due to numerical resistivity, creating a stretched configuration between a weak bubble and a weak blob, and this is followed by an increase in the current density within the stretched configuration, which in turn triggers the explicit resistivity, which helps the instability grow faster.

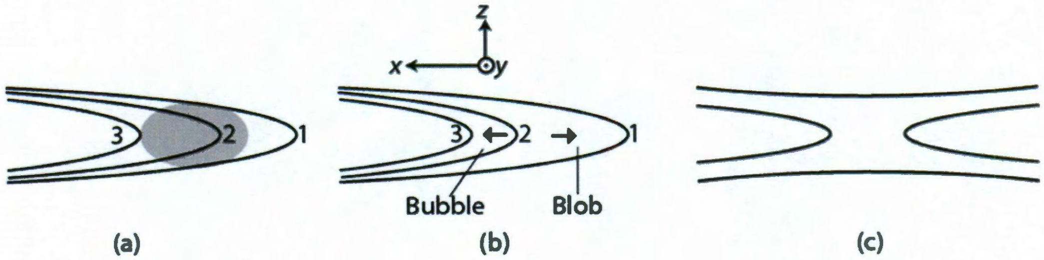

Figure 5.7 Illustration of the formation of bubble and blob due to region of anomalous resistivity and resulting acceleration (arrows).

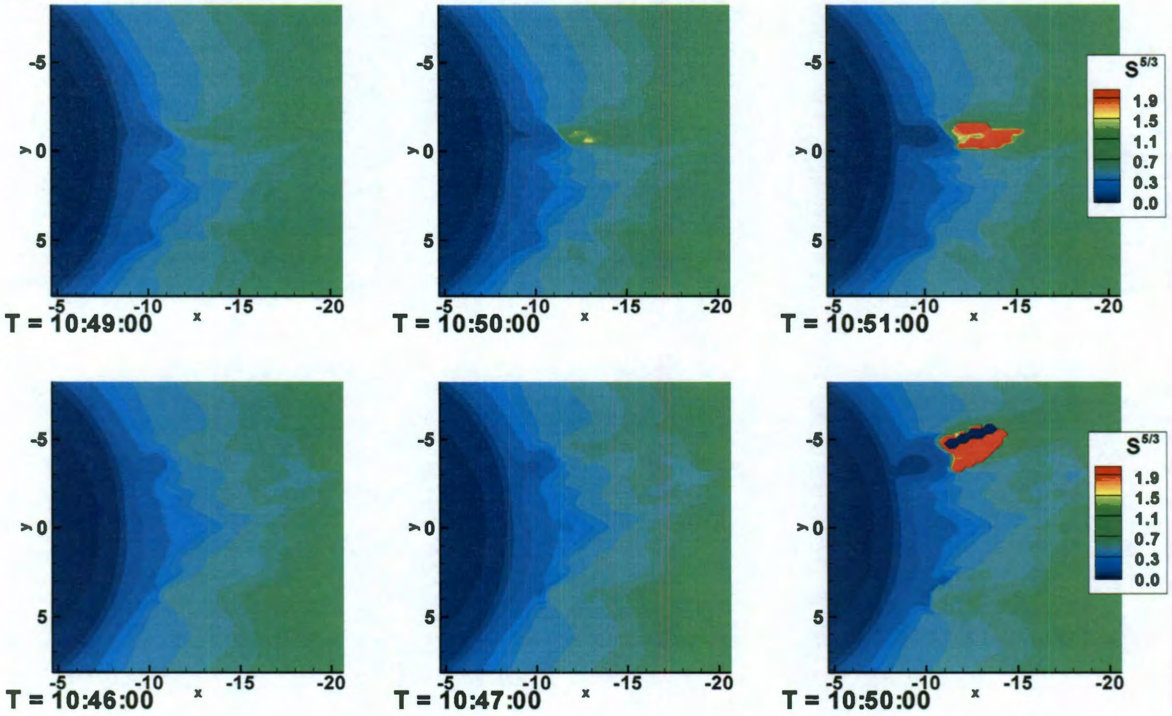

Figure 5.8 (first row) $S^{5/3}$ on the equatorial plane for the run with zero explicit resistivity. (second row) $S^{5/3}$ on the equatorial plane for the run with explicit resistivity on initially but turned off at 10:00.

5.3 Discussion and Summary

This chapter has centered on the verification, in terms of a global-MHD code, of the bubble-blob picture of how reconnection starts in a highly stretched inner plasma sheet, which is a central issue in the longstanding mystery of substorm onset. The physics of substorm onset has long been one of the leading questions of magnetospheric physics.

However, it is still not known exactly why stress gradually builds up in the tail and then gets released suddenly. *Siscoe et al.* [2009] pointed out that, if we could answer that magnetospheric-physics question, we might have an answer for the similar question for CMEs in the solar corona. *Yang et al.* [2011] proposed a partial answer to that question for the magnetosphere in terms of violation of frozen-in flux in a highly stretched inner plasma sheet and consequent formation of a bubble and a blob, leading to reconnection. In this work, we have demonstrated that it is easy to identify the development of a bubble-blob pair in a global MHD simulation. The demonstration simply requires plots of the time sequence of V_x and S or its 5/3 power in the center of the current sheet. *Birn et al.* 2011 showed entropy reduction in the near tail using a similar entropy analysis in an MHD simulation. The reduction is found to occur near the onset of reconnection and prior to the onset of fast reconnection and that leads to bubbles surging into the inner magnetosphere.

One significant aspect of this study is the demonstration that $S^{5/3}$ can be a useful diagnostic for global MHD simulations, particularly for the plasma sheet. One advantage of using the parameter $S^{5/3}$ is that it reduces to the thermodynamic quantity $pV^{5/3}$ in the limit of force equilibrium; that parameter plays a key role in interchange processes, which are crucial to plasma–sheet dynamics. The parameter $S^{5/3}$ is useful for assessing the accuracy with which the code solves its differential equations and for visualizing the regions where physical violation of $S^{5/3}$ conservation is most important. An additional advantage of $S^{5/3}$ as a diagnostic is that it is a characteristic of an entire field line and so can be represented as a contour plot on the equatorial plane, for example.

The *Yang et al.* [2011] paper confirmed the bubble-blob idea with the RCM-E, which has the limitations that it does not include inertial effects and cannot represent magnetic reconnection. The present study is based on a global MHD simulation, which does include inertia and represents reconnection, but it does not include effects of transport by gradient/curvature drift. More importantly, global MHD models have significant numerical-accuracy issues, particularly with regard to conservation of $S^{5/3}$ (Figure 5.4), which plays such an important role in plasma sheet dynamics. Conservation of the entropy parameter is violated in the MHD code largely because of numerical dissipation. Thus the simulation results cannot shed light on the small-scale processes involved in real entropy non-conservation or on whether the dissipation processes that operate before reconnection starts are the same as those that sustain it, once it starts. At t=10:47 and x=-11R_E, the full z-thickness half maximum for the y-component of the current density is about 1 R_E. In contrast, the ion gyro radius in this region is ~ 1100km and the ion inertia length ~ 100km; thus the current sheet thickness is not yet close to the ion gyro radius. We can only hope that the numerical dissipation that occurs in regions where sharp gradients occur in the code mimic the effects of micro-scale physical dissipation. There is no numerical code that we can confidently apply to the inner plasma sheet. The best we can do is to use different codes, with different strengths and weaknesses, which is what we have done in testing the bubble-blob idea with both RCM-E and OpenGGCM.

Comparison between OpenGGCM and the RCM-E simulations cannot easily separate the effects of inertia and gradient/curvature drifts, because it is very difficult to make the run setups the same in the two codes and because of the differences in numerical accuracy. We leave investigation of that to future work. Determination of the effects of different ionosphere conductances on the bubble/blob mechanism will also be left as future work.

Chapter 6

Summary and closing comments

In this thesis, several computational modeling efforts related to magnetohydrodynamics and their application to space science questions are described. Although there has been some progress in terms of building research tools and simulations, much more work needs to be done in the future to improve the models and our understanding of the magnetosphere physics.

One of the major efforts in this thesis is to couple the Global MHD model OpenGGCM to the RCM with the goal of building a comprehensive model capable of modeling both the inner and global magnetosphere. The one-way coupled model has been used to investigate the substorm injection event and bubbles are found to play an important role in the injection process. The detailed time history of the simulation is compared to available in situ satellite data with good agreement. This work also confirms the importance of the entropy parameter $pV^{5/3}$ for plasmasheet plasma transport. The two-way coupled OpenGGCM/RCM model has shown many encouraging features such as realistic ring current pressure and inner magnetosphere shielding. Future work on the two-way coupling should include testing of more feedback options and using newer versions both the RCM and the OpenGGCM. Newer versions of OpenGGCM are expected to have better code stability. The two-way-coupled OpenGGCM/RCM model can be also used to simulate storms which can test the code further. As two-way coupled MHD-RCM models are considered as one of the most self-consistent approaches to describe space plasma, I hope that this new model will provide more insights into many long-standing magnetosphere problems.

A new direct integration method to compute the field-aligned currents from the MHD magnetic field is described and partially tested. The method is a promising approach that could be used in MHD codes to better resolve the region-2 currents and to add inertial effects to the RCM, especially in coupled runs where the tracing of field lines is done on a frequent basis. However, the approach is limited by the grid resolution and code precision as well as the accuracy of the tracer. To obtain the currents in the entire ionosphere, a practical solution is to blend the direct-integrated currents at lower latitude with the original MHD currents at higher latitude. The detailed technique to blend the two is yet to be developed based on more tests of this method. When a suitable blending technique is obtained, these currents could be used to drive a standalone MHD simulation and the effect of them on M-I coupling can be studied.

Idealized substorm simulation using the OpenGGCM has been carried out to study how reconnection may start from initially closed field lines. This question of substorm initiation has been a controversial issue in substorm studies and this work presents a new way of initiating a substorm. The proposed bubble-blob mechanism naturally gives arise to a decrease of the normal magnetic field component, which would lead to reconnection. Although the creation of bubble and blob in the simulation is of numerical origin (diffusion), a similar dissipation mechanism may operate in nature. The study also showed the importance of analyzing MHD simulation results using the total derivative of the entropy parameter, which can be used as a diagnostic tool to access numerical errors in MHD simulations.

Continuing effort will be devoted to develop the new friction code for which the initial work has been described in Appendix C. Future work on the friction code and the friction code based regional-MHD code may help increase our understanding of inertial effects and improve the accuracy in storm simulations.

Appendix A: Exchange information between RCM and OpenGGCM

The OpenGGCM is a parallel code so that different parts of the computational domain are solved on different nodes; it uses the message passing interface (MPI) library to exchange information between computational nodes, while the current version of the RCM is serial so that all calculations are done on a single node. In order to communicate information from the OpenGGCM to the RCM, conversions have to be done to allow information exchange. The RCM works on a 2D ionosphere grid which usually has grid size around 200x100. The OpenGGCM provides the following quantities to RCM on the boundary: η_s, the flux tube content per unit magnetic flux for particles of invariant energy λ_s, V the flux tube volume, and the mapping point on the equatorial plane and the magnetic field at the mapping point. The OpenGGCM has magnetic field information and plasma density ρ and pressure P (or temperature T) on its 3D grid, in GSE coordinates. It thus traces from every grid point of the RCM ionospheric grid (in the northern hemisphere) to the southern ionosphere to get the x and y locations where the fieldlines cross the equatorial plane, and the magnitude of the magnetic field; here the equatorial crossing point is defined as the point where the field line crosses the center of the current sheet. During the trace procedure, we use a dipole magnetic field inside 4.5R$_E$, the MHD magnetic field outside 6.5R$_E$ and a smooth combination of the two fields in between. Interpolation is done to map the MHD ionospheric potential onto the RCM grid. To get the flux tube content per unit magnetic flux η for a particular chemical species(electron and proton) and particular energy invariant, from the single fluid MHD number density *n* and temperature *T*, one firstly has to assume a temperature ratio between electrons and protons. We take the observational plasma sheet ion and electron temperature ratio as $T_i/T_e = 7.8$ [*Baumjohann et al.*, 1989]. Then we need to assume a distribution function $f_s(\lambda)$ for each particle species; then flux tube content can be derived using the formula

$$\eta_s = \int_{\lambda_{\min}}^{\lambda_{\max}} \frac{2^{5/2}\pi}{m_s^{3/2}} f_s(\lambda)\sqrt{\lambda}d\lambda \tag{A.1}$$

where $\lambda_{\max}$ and $\lambda_{\min}$ are the minimum and maximum invariant energy values of channel s. One choice for the distribution function $f_s(\lambda)$ is a Maxwellian

$$f_s(\lambda_s) = n(\frac{m_s}{2\pi kT_s})^{3/2} e^{-(\lambda_s V^{-2/3}/kT)} \tag{A.2}$$

where *k* is the Boltzmann constant, *n* is particle number density, *T* is T_i for ions and T_e for electrons, and *s* denotes to different energy channels for particular particle species.

Integration gives the conversion formula for flux tube content as:

$$\eta_s = nV\{erf(X_{\max}) - erf(X_{\min}) - \frac{2}{\sqrt{\pi}}[X_{\max}e^{-X_{\max}^2} - X_{\min}e^{-X_{\min}^2}]\} \tag{A.3}$$

where $X = \sqrt{\frac{|\lambda|}{kTV^{2/3}}}$, $X_{\max}$ is the value of X when $\lambda = \lambda_{\max}$ and $erf(x)$ is the error function.

One can also assume a kappa distribution function as

$$f_s(\lambda) = n(\frac{m}{2\pi bkT})^{3/2} \frac{\Gamma(\kappa+1)}{\Gamma(\kappa-1/2)} \frac{1}{(1+\frac{\lambda V^{-2/3}}{bkT})^{\kappa+1}} \tag{A.4}$$

b is $\kappa - \frac{1}{2}$ and the other factors are defined in the same way as in equation (A.2). The integration gives

$$\eta_s = \frac{4nV}{\sqrt{\pi}} \frac{\Gamma(\kappa+1)}{\Gamma(\kappa-1/2)} \int_{X_{\min}}^{X_{\max}} \frac{x^2}{(1+x^2)^{\kappa+1}} dx$$

with $X = \sqrt{\frac{|\lambda|}{bkTV^{2/3}}}$

From RCM's multi-fluid information to MHD, one just needs to sum up all the energy channels and the formulas are

$$n = \sum_s \frac{\eta_s}{V} \tag{A.5}$$

$$P = \frac{2}{3} \sum_s \eta_s |\lambda_s| V^{-5/3} \tag{A.6}$$

Appendix B: Correction for non-zero *Vz*

To correct equatorial velocity plots for the situation where *Vz* is non-zero in the equatorial plane, consider two test particles frozen to the same magnetic field line. Particle 1 moves with a fluid element that is crossing the equatorial plane at time t, and particle 2 stays on the same field line as particle 1 but remains at z=0. Both particles are at the same point at time t. Since the two particles remain on the same field line,

$$\mathbf{v}_1 \times \mathbf{B} = \mathbf{v}_2 \times \mathbf{B} \tag{B.1}$$

Writing out the three components of (3) and setting $v_{2z}=0$ gives

$$\mathbf{v}_2 = \mathbf{v} - v_z \frac{\mathbf{B}_e}{B_{ez}} \tag{B.2}$$

where $\mathbf{B}_e$ is the magnetic field in the equatorial plane and B_{ez} is its z component. In the above equation, we have written **v** instead of $\mathbf{v}_1$, because particle 1 moves with the fluid.

Since $\mathbf{v}_2$ has only x and y components, it is easy to represent in terms of arrow plots in the equatorial plane.

Appendix C: A new numerical method for the magneto-friction code

This appendix describes work in progress on building a new version of the magneto-friction code using newer numerical methods. I put it in this appendix to document what has been changed in the MPI version of the friction code.

A.C.1 Introduction

The friction code solves a set of modified MHD equations to find a magnetospheric equilibrium condition so that $J \times B = \nabla p$, where B is the magnetic field, J is the current density and p is the plasma pressure. Finding magnetospheric equilibrium solutions of interest since during quiet times, the magnetosphere is in a quasi-equilibrium state, in other words, although the system is not static, if we take a snapshot at any given time, it is to a good approximation in force balance [*Voigt and Wolf*, 1988]. This is particularly true for the inner magnetosphere where the flow is slow compared to the thermal and wave speeds. For inner magnetosphere models such as the RCM, the plasma motion can be accurately computed but the magnetic field model that goes into the calculation is taken as an input and is not necessarily in force balance with the plasma. By coupling a magnetosphere equilibrium code, such as the friction code, to the RCM, the magnetic field can be self-consistently computed during the simulation.

The modified set of equations that the friction code uses is

$$\frac{\partial \rho}{\partial t} + \nabla \cdot (\rho \vec{v}) = 0$$

$$\frac{\partial \rho \vec{v}}{\partial t} = \vec{J} \times \vec{B} - \nabla p - \nabla \cdot [\rho \vec{v} \vec{v}] - \alpha \rho \vec{v} + \upsilon \nabla^2 \rho \vec{v}$$

$$\frac{\partial p}{\partial t} = -\nabla \cdot (p \vec{v}) - (\gamma - 1)(\nabla \cdot \vec{v}) p$$

$$\begin{aligned} &\frac{\partial \vec{B}}{\partial t} = -\nabla \times \vec{E} \\ &\vec{E} + \vec{v} \times \vec{B} = 0 \\ &\vec{J} = \frac{1}{\mu_o} \nabla \times \vec{B} \\ &\nabla \cdot \vec{B} = 0 \end{aligned} \tag{C.1}$$

Compared to the ideal MHD equations, only the momentum equation is different, where the $-\alpha \rho \vec{v}$ term represents the friction force and $\upsilon \nabla^2 \rho \vec{v}$ a viscosity term. With these extra terms, the system will dissipate energy until it gets to an energy minimum state. It has been shown that when the system is at its minimal energy state, the magnetic field is in force balance with the pressure distribution [*Hesse and Birn*, 1993]. Note that the time *t* shown in the above equations is not the real time but an artificial time. *Hesse and Birn*, [1993] argued the final equilibrium state does not depend on the path of the evolution, i.e. choosing a different friction parameter α in the simulation, in principle, won't change the final equilibrium state.

The friction code has been used at Rice for many years and forms an important part of the self-consistent model called the RCM-E. The code itself was based on Hesse and

Birn's magneto-friction code originally developed for the magnetotail and later modified to include the inner magnetosphere by Toffoletto and co-workers [*Toffoletto et al.* 2002, *Lemon et al.* 2003]. Other variants of the friction code have also been developed, for example, a version that allows pressure anisotropy was developed by Liang Wu [*Wu et al.*, 2009]. The original version of friction code also assumes north-south symmetry (no dipole tilt) and Liheng Zheng [*Zheng*, 2011] has developed a version that allows a non-zero dipole tilt angle. In other developments, Vinod Kumar developed a parallel version of the friction code using the Message Passing Interface (MPI). This appendix will describe work done on the parallel friction code following the MPI version. Our current effort is motivated in attempt to address some of the problems and issues with the original friction code and we will attempt to improve the code by using a new numerical method.

A.C.2 Friction code numerical method

A.C.2.1 Grid

The friction code uses a stretched Cartesian grid similar to the OpenGGCM grid described in Chapter 2, with all variables stored at the cell center (The OpenGGCM uses a staggered mesh, where the magnetic field is stored on the faces of the grid cells and the gasdynamic quantities at the center). The grid spacing of the friction code is generated from a non-linear function. For example, if we take the grid on the positive x axis, the coordinates of the grid locations are specified by the function $(ix-1)\Delta h - 0.8\frac{(n-1)\Delta h}{\pi}\sin((ix-1)\pi/(n-1))$, where *ix* is the index (here *ix*=1 at *x*=0), $\Delta h = \frac{L}{n-1}$ is the grid space if the grid is uniform. The first term describes a uniform linear grid and the second term describes the deformation of the uniform grid based on a sine function. The density of the grid (the reciprocal of the derivative of the grid function) decreases as *ix* increases (further away from the Earth) and we can adjust the grid parameters to allow higher resolution in the regions of interests.

A.C.2.2 Time and Spatial discretization

The equations in the friction code are written in their primitive form so that all the spatial derivatives can be easily approximated by finite differences. In the actual implementation, a simple second-order central difference method is used for the spatial derivatives. It is well known that numeric methods with even orders of accuracy introduce dispersion to the solution [*Harten et al.*, 1976]. This means the numerical method used in the friction code would introduce new extremas rather than smearing out the solution; this is problematic when there are steep gradients. Grid oscillations can also occur since the central derivative does not detect these sharp changes. In addition, for a second-order central finite difference scheme, the $\nabla \cdot \vec{B} = 0$ conservation is not built-in and a $\nabla \cdot \vec{B}$ cleaner is sometimes implemented. However, the $\nabla \cdot \vec{B}$ cleaner is costly and not often used.

The time integration is done using the third-order Adams-Bashforth (AB3) method. In solving MHD equations, the time integration scheme is not as critical and alternative methods such as the high order stability-preserving Runge-Kutta methods could also be used. The third order AB3 method requires storing 3 copies of the changes of all variables and this puts a significant memory constraint especially for high-resolution runs. However, the AB3 method is preferred because it has been found that the second order AB2 scheme is unstable for advection problems [*Canuto et al.*, 1988]. Other popular schemes like the leapfrog and Richtmyer methods also have exhibited stability issues when applied in the friction code [*Lemon et al.* 2003].

A.C.2.3 Boundaries and initial conditions

The simulation domain is a rectangular box. At the outer boundaries of the box, the normal derivatives of plasma density, pressure and the tangential magnetic field are set to zero (The normal component of the magnetic field is set to satisfy $\nabla \cdot \vec{B} = 0$). The flow velocity is set to zero at the boundary so no energy flows in or out of the simulation box.

As for the near Earth boundary, the friction code's boundary is similar to the OpenGGCM but it is located at 2 R_E from the Earth. However, there is no coupling between the ionosphere and the magnetosphere. The plasma is kept static inside the inner boundary and the magnetic field is uniform.

The initial pressure condition is often taken from empirical models or the RCM, on the 2D equatorial plane. For grid points away from the equatorial plane, tracing of field line is done to map the value on the equatorial plane to the starting grid point (since the pressure is constant along a field line for static equilibria). For field lines that cross the tailward boundary before reaching the equatorial plane, a one-dimensional integration in the vertical direction is done to compute the pressure value.

A.C.2.4 Parallelization

The original parallelization is done by dividing the simulation box into sub-domains assigned to different processors. For simplicity, every processor holds the entire global grid in the memory but only loops through the sub-domain that it is in charge of. This approach allows minimal code change during the parallelization but poses a problem for higher resolution because the memory does not scale. It also has performance issues (cache misses) since the data is not stored continuously.

A.C.3 New Numerics

To address the problems in the friction code, a new version of the parallel code has been developed that is supposed to handle steep gradient better and also can be used as an MHD code (by removing the friction and viscosity terms in equation C.1). I will describe the major changes to the code starting from the grid and later proceeding to the solver. This will also serve as documentation for the new code.

A.C.3.1 Staggered Yee Grid

As noted in section 1.2.2, the friction code does not conserve magnetic flux which could introduce serious errors in the solution. In the new code, we use the Constrained Transport (CT) method by staggering the magnetic field grid to the pressure grid, i.e., the magnetic field is now solved on the faces of the cells and the electric field is reconstructed on the edge. This should ensure the discrete version (the form chosen in the code) of $\nabla \cdot \vec{B}$ is maintained to round-off error. Note the initial state of $\nabla \cdot \vec{B}$ should be zero or the CT method would not remove the pre-existing $\nabla \cdot \vec{B}$.

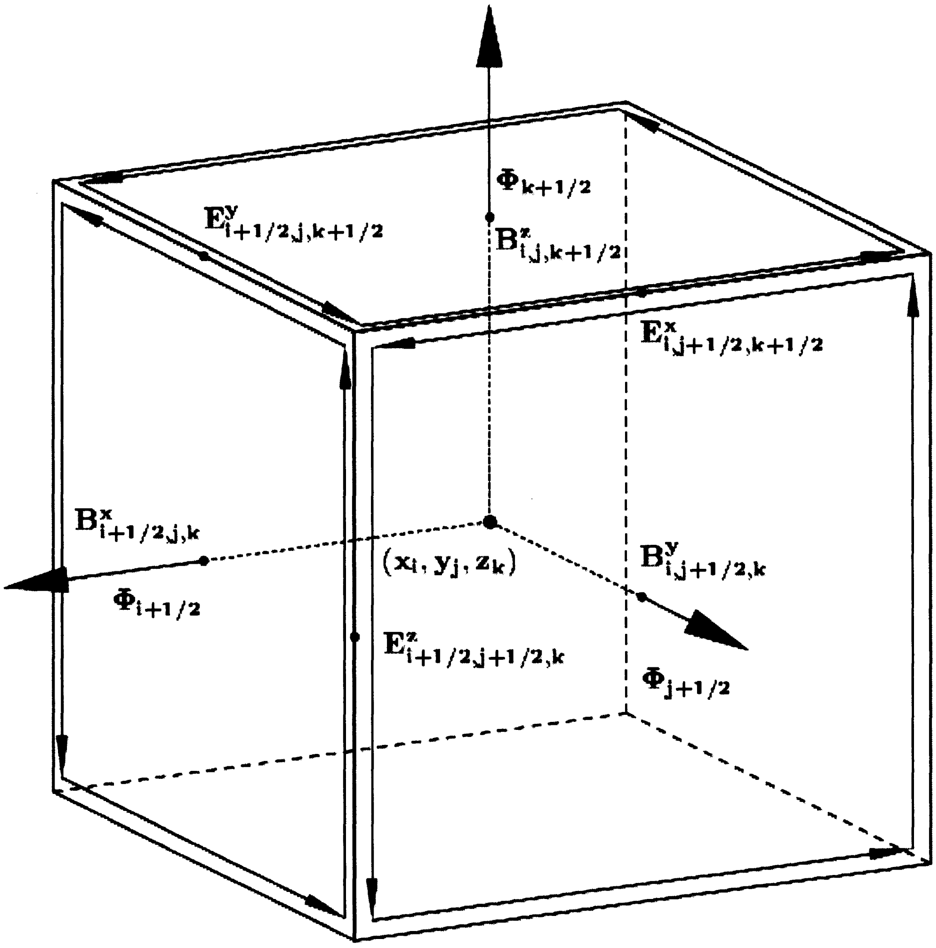

Figure A.C.1 The structure of a staggered grid cell with the center at x_i,y_j,z_k. The fluxes for cell centered conservative variable Φ and the magnetic field are on cell faces. The electric field and current are on the cell edges. Adapted from *Raeder et al*, [2001].

The structure of the cell is shown in Figure A.C.1. We define the cell face index *i* for the magnetic field at cell face *i*+1/2, thus the flux f_x (i, j, k) actually means the flux at (i+1/2, j, k) . To get the magnetic field grid, using the grid (ssx_bx) for *Bx* as an example, we use ssx_bx (ix) = 0.5*(ssx (ix)+ssx (ix+1)), where ssx is the cell-centered grid in x direction. To get back the magnetic field at the cell center, an average of two faces values is taken, for example, bx_center(ix) = 0.5*(bx(ix)+bx(ix-1)). The current density aj is now computed at the cell edges and is calculated from the magnetic field as

```
ajx (ix,iy,iz) =  (bdy4(iy)*(bzj(ix,iy+1,iz) - bzj(ix,iy,iz)) &
                 - bdz4(iz)*(byj(ix,iy,iz+1) - byj(ix,iy,iz)))
ajy (ix,iy,iz) = (-bdx4(ix)*(bzj(ix+1,iy,iz) - bzj(ix,iy,iz)) &
                 + bdz4(iz)*(bxj(ix,iy,iz+1) - bxj(ix,iy,iz)))
ajz (ix,iy,iz) =  (bdx4(ix)*(byj(ix+1,iy,iz) - byj(ix,iy,iz)) &
                 - bdy4(iy)*(bxj(ix,iy+1,iz) - bxj(ix,iy,iz)))
```

where bdx(y, z)4 is defined as the reciprocal of the cell spacing in the x(y, z) direction and bxj, byj and bzj are the magnetic field perturbations to the dipole magnetic field. A four-point average is used to get the currents back at center (ajxc,ajyc,ajzc), which would be used with the centered magnetic field to compute the forces. The average is done as:

```
ajxc (ix,iy,iz) = 0.25*(ajx(ix,iy,iz)+ajx(ix-1,iy,iz)   &

  +  ajx(ix,iy-1,iz)+ajx(ix,iy,iz-1))

ajyc (ix,iy,iz) = 0.25*(ajy(ix,iy,iz)+ajy(ix-1,iy,iz)   &

  +  ajy(ix,iy-1,iz)+ajy(ix,iy,iz-1))

ajzc (ix,iy,iz) = 0.25*(ajz(ix,iy,iz)+ajz(ix-1,iy,iz)   &

  +ajz(ix,iy-1,iz)+ajz(ix,iy,iz-1)).
```

Part of the success of CT methods for MHD models lies in the reconstruction of the numeric flux for the magnetic induction equation, i.e. the electric field. The reconstruction must be monotonic to allow stable magnetic flux convection. There are many interpolation methods that could be used in conjunction with CT. For our case, the electric field on the edge is upwind interpolated by a van Leer monotonicity method which is second order accurate in space.

To get the electric field, using the *Ex* in Figure A.C.1 as an example, first a four-point average similar to the current average is taken to obtain the velocities $Vy_{i,j+1/2,k+1/2}$ and $Vz_{i,j+1/2,k+1/2}$ on the edge. For Bz at the edge, we first compute a raw slope in y direction as in equation (C.2),

$$(dBz)_{j+1/2} = (Bz_{j+1} - Bz_j) / \Delta y_{j+1/2} \qquad \text{(C.2).}$$

This raw slope is used to compute a second-order monotonic distribution of slopes:

$$\begin{aligned}(dBz)_j &= \frac{(dBz)_{j+1/2}(dBz)_{j-1/2}}{(dBz)_{j+1/2}+(dBz)_{j-1/2}} && \text{if} \quad (dBz)_{j+1/2}(dBz)_{j-1/2}>0 \\ &= 0 && \text{if} \quad (dBz)_{j+1/2}(dBz)_{j-1/2} \le 0\end{aligned} \qquad \text{(C.3).}$$

The *Bz* at the edge is then calculated as (C.4)

$$\begin{aligned}Bz_{i,j+1/2,k+1/2} &= Bz_{i,j,k+1/2} + (dBz)_{i,j,k+1/2}[\Delta y_j - \Delta t Vy_{i,j+1/2,k+1/2}] && \text{if } Vy_{i,j+1/2,k+1/2} > 0 \\ Bz_{i,j+1/2,k+1/2} &= Bz_{i,j+1,k+1/2} - (dBz)_{i,j+1,k+1/2}[\Delta y_{j+1} + \Delta t Vy_{i,j+1/2,k+1/2}] && \text{if } Vy_{i,j+1/2,k+1/2} < 0\end{aligned} \qquad \text{(C.4).}$$

There are two reconstructions for each component of the electric field, so the code does 6 reconstructions to get the electric field on the edge. Other reconstruction methods such as the donor cell, piecewise parabolic (PPM) or the upwind biased WENO method could also be applied.

I should note here that the CT method only enforces $\nabla \cdot \vec{B} = 0$ in one particular form of discretization, in our case it is the difference from one face to another left and right of a given cell center. The initial condition should also have $\nabla \cdot \vec{B} = 0$ in the same form of discretization. MHD codes often use analytical vector potentials to setup initial field as it is easy to chose a discretization so that $\nabla \cdot (\nabla \times \vec{A}) = 0$. Direct assignment of divergence free analytical field to a grid won't guarantee discrete divergence free. The boundary condition should also be set so that the same form of discrete divergence is zero.

A.C.3.2 Memory allocation

To allow the friction code to run on higher resolution, we now use a distributed memory allocation scheme. Unlike the original friction code in which each processor holds the entire array, now each processor allocates local arrays for most of the variables except the magnetic field and other variables for the tracing. A Fortran feature that allows defining an array starting from arbitrary index is utilized to reduce memory use without changing the previous loop indexes used in the global array case. This also allows us to use legacy codes without much modification.

In the new version of the code, all large arrays now are dynamically allocated to reduce memory footprints at runtime. It is possible to use the dynamic allocation scheme with the restart function to change grid during a simulation in the future.

There are still ~10 global arrays present in the code so as to be compatible with the part of the code that has yet to be changed. These arrays such as the magnetic field are needed in the parallel tracing program. The goal would be to phase out these global arrays and implement a scalable parallel tracing scheme in the future.

Ghost cells that are at the boundaries of the simulation are used to set boundary conditions and also allow easier implementation of finite differences. The ghost number is currently 1 at each side, which could be updated to 2 or more to allow easier implementation of higher order methods in the future.

A.C.3.3 Numerical solver

While there has been considerable effort to compute 3D magnetospheric models using MHD [e.g. *Lyon et al.*, 2004, *Raeder et al.* 2001, *Powell et al*, 1999], the best way to solve the MHD equations numerically is still under considerable debate and there is no consensus in the community on how to accurately solve the MHD equations. It is not clear if any of the models solvers are grid converged [e.g. *Ridley et al.* 2010] which means the solution keeps changing as the grid is refined. One reason for this difficulty is that the MHD equations describe a complicated system in three dimensions and in a complicated geometry. There is no intrinsic scale length in MHD equations. Non-linearities in the equations lead to formations of shocks and contact discontinuities. Unlike the hyperbolic Euler equations, the eigenvalues of the MHD Jacobians shows that the equation is not strictly hyperbolic since the fast, slow mode wave and the Alfven waves coincide at the triple point [*Roe*, 1996], which makes it hard to analyze the MHD codes. Another particular difficulty is the divergence constraint on the magnetic field which, when not conserved, would cause spurious errors in the solution [Brackbill and Barnes, 1980].

In practice, the MHD equations are numerically solved using either finite volume or finite difference method. For a finite volume approach, the MHD equations are often written in conservative form

$$\frac{\partial U}{\partial t} = -\nabla \cdot F(U) \qquad \text{(C.5),}$$

where ***U*** is a vector of $(\rho, \rho\vec{v}, e, B)$, *e* is the total energy and *F(**U**)* is a vector of the corresponding fluxes for ***U***. Equation (C.4) can be written as a semi-discrete (discretized in space but not in time) form as,

$$\Delta U = -\Delta t[(\frac{F_{xR} - F_{xL}}{\Delta x}) + (\frac{F_{yR} - F_{yL}}{\Delta y}) + (\frac{F_{zR} - F_{zL}}{\Delta z})] \qquad (C.6).$$

Equation (C.5) can be easily time integrated using the AB3 methods mentioned before and other stability preserving method, once the fluxes across cell faces are specified. Generally, the choice of the flux at the cell faces has the most impact on MHD model results.

The fully conservative MHD equation has a numerical problem in calculating the fluid pressure from the total energy, since in low beta regions the pressure becomes the difference of two large numbers (the total energy and the magnetic energy) and sometimes the pressure can be less than zero. Thus a simpler approach which I choose to implement is to split the MHD equations to a separate fluid and magnetic parts, i.e. a semi-conservative form, for the friction code, written as

$$\frac{\partial \rho}{\partial t}+\nabla\cdot(\rho\vec{v})=0$$

$$\frac{\partial \rho\vec{v}}{\partial t}+\nabla\cdot(\rho\vec{v}\vec{v}+p\vec{I})=\vec{J}\times\vec{B}-\alpha\rho\vec{v}+\upsilon\nabla^2\rho\vec{v}$$

$$\frac{\partial e}{\partial t}+\nabla\cdot((e+p)\vec{v})=\vec{J}\cdot\vec{E}$$

$$\begin{aligned}
&\frac{\partial \vec{B}}{\partial t}=-\nabla\times\vec{E}\\
&\vec{E}+\vec{v}\times\vec{B}=0\\
&\vec{J}=\frac{1}{\mu_o}\nabla\times\vec{B}\\
&\nabla\cdot\vec{B}=0\\
&e=\frac{1}{2}\rho v^2+p/(\gamma-1)
\end{aligned}\qquad\text{(C.7).}$$

This form implies that the $\vec{J}\times\vec{B}-\alpha\rho\vec{v}+\upsilon\nabla^2\rho\vec{v}$ and $\vec{J}\cdot\vec{E}$ term act as source terms onto the gasdynamic equation. We could use well-established approximate Riemann solvers for the gasdynamic equations for the fluid part and then treat the magnetic field separately.

A.C.3.3.1 Numerical fluxes

To form a complete scheme for the gas dynamic part of the MHD equation using equation (C.5), the numeric fluxes have to be specified. The problem is to reconstruct numeric flux for $\rho, \rho\vec{v}, e$ at the cell faces from their information (U_L, U_R) stored on cell centers (Here we assume the magnetic field is known everywhere for this step). If one take a simple average of the cell-centered flux adjacent to the cell interface (in one-dimension for simplicity)

$$f_{i+1/2} = \frac{1}{2}(f_i + f_{i+1}) \qquad \text{(C.8),}$$

then mathematically this is identical to the original second-order central method. Similarly, there are other choices such as the fourth-order central (a function of $f_i, f_{i+1}, f_{i+2}, f_{i-1}$) and the Lax scheme (a function of f_i, f_{i+1}). The Lax-Friedrichs flux, in addition of the cell-centered flux, takes account of the wave propagation velocities and is written as,

$$f_{i+1/2} = \frac{1}{2}(f_i + f_{i+1}) - \frac{1}{2}\max(v_i, v_{i+1})(U_{i+1} - U_i) \qquad \text{(C.9).}$$

However, the Lax-Friedrichs flux is quite diffusive.

Another class of fluxes is constructed using a method proposed by Godunov. If the information on the left and right of the interface (U_L, U_R) is known, one could solve a Riemann problem to obtain the numeric flux [Godunov, 1959]. However, for MHD equations, the exact Riemann solution is very complicated so an approximate Riemann solution is often used. There are two classes of approximate Riemann solvers: one is called the linear (Roe) solver [*Roe*, 1981] which is based on linear average across the cell interface; the other class is non-linear solvers such as HLL (Harten, Lax, van Leer) [*Harten et al.*, 1983] and HLLC (C stands for contact wave) [*Toro et al.*, 1994]. They usually approximate fewer waves in the Riemann fan than the Roe type solve but they usually guarantee positive pressure [*LeVeque*, 2002].

For a HLL-type two-wave solver [*Fuchs et al.*, 2009], which has been implemented in the friction code, the numeric flux at the interface is defined as

$$f = \{ \begin{array}{ll} f_L & \text{if } S_L > 0 \\ f_{middle} & \text{if } S_L < 0 < S_R \\ f_R & \text{if } S_R < 0 \end{array} \qquad \text{(C.10)},$$

in which f_L and f_R are the flux left and right of the interface, S_L and S_R are perpendicular propagating velocity for one left-going wave and one right-going wave. The middle flux is

$$f_{middle} = \frac{S_R f_L - S_L f_R + S_L S_R (U_R - U_L)}{S_R - S_L} \qquad \text{(C.11)}.$$

The wave speed S_L and S_R are defined as

$$\begin{aligned} S_L &= \min\{v_L - s_L, \bar{v} - \bar{s}\} \\ S_R &= \max\{v_R + s_R, \bar{v} + \bar{s}\} \end{aligned} \qquad \text{(C.12)}.$$

v_L and v_R are the left and right velocity at the interface. s_L and s_R are the extended sound speed at the left and right of the cell interface; the extended sound speed is defined as,

$$s = \frac{1}{\sqrt{\rho}} \sqrt{\gamma p + (\gamma - 1)(B_{perp1}^2 + B_{perp2}^2)} \qquad \text{(C.13)}$$

where B_{perp1} and B_{perp2} represent the magnetic field components perpendicular to the flux direction.

The two averaged speeds in equation (C.10) are given by

$$\bar{v} = \frac{v_L + v_R}{2} \quad \bar{s} = \sqrt{\frac{1}{2}(\frac{1}{\rho_L} + \frac{1}{\rho_R})} \cdot \sqrt{\frac{\gamma}{2}(\rho_L + \rho_R) + (\gamma - 1) B_{perp}^2} \qquad \text{(C.14)}.$$

The average sound speed in equation (C.12) is actually from the eigenvalue of the arithmetic averaged Jacobian of the right and left states.

The friction code now has an option to specify the choice of numerical flux so that a user can test the same problem with different solvers. It is also very easy to add on additional solvers such as the HLLC or Roe solver to the code.

A.C.3.3.2 WENO (Weighted essentially non-oscillatory) reconstruction

The Godunov methods introduced in the last section are believed to be diffusive, however people have found that a good interpolation method can help greatly offset this problem and improve the numerical results. In this approach, U_R and U_L are no longer the cell centered values adjacent to the cell faces but are reconstructed values just at the left and right of the cell interface. The recently introduced WENO reconstruction [*Shu*, 1998] method is probably the most modern scheme that is widely used in higher-order convection methods to increase the order of accuracy and stability [*Smit et al.* 2005]. A *k*th order WENO reconstruction scheme provides a uniform high order ((2*k*-1)th) of accuracy in smooth regions and *k*th order of accuracy in non-smooth regions. It is shown in Shu, [1998] that when used with a high order WENO reconstruction, even the most diffusive Lax-Friedrichs flux scheme gives similar results compared to the less diffusive Godunov flux. Thus we implemented the WENO reconstruction routine to use with our numerical solvers.

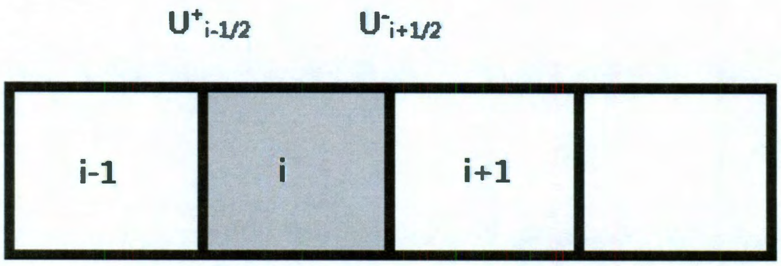

Figure A.C.2 WENO23 reconstruction scheme for cell i (grey area). The values at cell face i-1/2 and i+1/2 are reconstructed from cells i-1, i and i+1.

I will use a one-dimensional second-order WENO scheme (WENO23) as an example to describe the reconstruction process. As shown in Figure A.C.2, we want to construct $U^+_{i-1/2}$ and $U^-_{1+1/2}$ at the cell faces of cell i. The plus and minus sign represents the values are from the reconstruction for cell i since if one do another reconstruction for cell i+1, another reconstruction value $U^+_{i+1/2}$ can be obtained at cell interface i+1/2.

A traditional higher order interpolation method would use a fixed number of stencils to reconstruct the fluxes. In this case, a steep gradient is often not well represented and oscillations are introduced into the solution. One approach is to switch to a first order scheme near discontinuities or apply a limiter to limit the new extremas created by the interpolation. The ENO (Essentially Non-Oscillatory) scheme [*Harten et al*, 1987] computes a set of interpolations using different stencils and then determine the best stencil to use depending on the smoothness of the solution. The WENO method goes one step further. Instead of just using one stencil as the best stencil in the ENO scheme, interpolations from all the candidate stencils are weighted summed to achieve uniformly high order accuracy.

For our example to construct $U^{-}_{1+1/2}$, the first step is to obtain second order interpolations for values at interface i+1/2 using the stencil (i, i+1) and (i, i-1), assuming the grid is uniform

$$\begin{aligned} u_{i+1/2,0} &= \frac{1}{2}u_i + \frac{1}{2}u_{i+1} \\ u_{i+1/2,1} &= -\frac{1}{2}u_{i-1} + \frac{3}{2}u_i \end{aligned} \qquad \text{(C.15).}$$

Then the WENO23 reconstructed $U^{-}_{1+1/2}$ is given by

$$U^{-}_{1+1/2} = w_{i+1/2,0}u_{i+1/2,0} + w_{i+1/2,1}u_{i+1/2,1} \qquad \text{(C.16)}$$

$w_{i+1/2,0}$ and $w_{i+1/2,1}$ are weight factors and defined as

$$\begin{aligned} w_{i+1/2,0} &= \frac{\alpha_0}{\alpha_1 + \alpha_0} \\ w_{i+1/2,1} &= \frac{\alpha_1}{\alpha_1 + \alpha_0} \end{aligned} \qquad \text{(C.17)}$$

where

$$\begin{aligned} \alpha_0 &= \frac{2}{3(\varepsilon + \beta_0)^2} \\ \alpha_1 &= \frac{1}{3(\varepsilon + \beta_1)^2} \end{aligned} \qquad \text{(C.18).}$$

In equation (C.16), β is usually called the smoothness indicator and is defined as

$$\begin{aligned}\beta_0 &= (u_{i+1} - u_i)^2 \\ \beta_1 &= (u_i - u_{i-1})^2\end{aligned} \qquad \text{(C.19).}$$

For non-uniform grids, the constant coefficients are calculated based on the grid distribution and then a similar reconstruction from (C.13) to (C.17) can be carried out. Higher order (up to seven) WENO construction schemes are complicated but are available in *Shu*, [1998].

Bibliography

Akasofu, S.-I. (1964), The development of the auroral substorm, *Planet. Space Sci.,* 12(4), 273.

Apatenkov, S. V., Sergeev, V. A., Kubyshkina, M. V., Nakamura, R., Baumjohann, W., Runov, A., Alexeev, I., Fazakerley, A., Frey, H., Mühlbachler, S., Daly, P. W., Sauvaud, J.-A., Ganushkina, N., Pulkkinen, T., Reeves, G. D., Khotyaintsev, Y. (2007), Multi-spacecraft observation of plasma dipolarization/injection in the inner magnetosphere, *Ann. Geophys.,* 24, 801-814.

Angelopoulos, V., C. F. Kennel, F. V. Coroniti, R. Pellat, M. G. Kivelson, R. J. Walker, C. T. Russell, W. Baumjohann, W. C. Feldman, and J. T.Gosling (1994), Statistical characteristics of bursty bulk flow events, *J. Geophys. Res.,* 99, 21257-21280.

Angelopoulos, V., Sibeck, D., Carlson, C. W., McFadden, J. P., Larson, D., Lin, R. P., Bonnell, J. W., Mozer, F. S., Ergun, R., Cully, C., Glassmeier, K. H., Auster, U., Roux, A., Lecontel, O., Frey, S., Phan, T., Mende, S., Frey, H., Donovan, E., Russell, C. T., Strangeway, R., Liu, J., Mann, I., Rae, J., Raeder, J., Li, X., Liu, W., Singer, H. J., Sergeev, V. A., Apatenkov, S., Parks, G., Fillingim, M., Sigwarth, J. (2008), First results from the THEMIS mission, *Space Sci. Rev.* ,141, 1-4, 453-476.

Axford, W. I., C. O. Hines, A unifying theory of high-latitude geophysical phenomena and geomagnetic storms, *Can. J. Phys*., 39, 1433, 1961.

Baumjohann, W., G. Paschmann, and C. Cattell (1989), Average Plasma Properties in the Central Plasma Sheet, *J. Geophys. Res.*, 94(A6), 6597–6606.

Belian, R. D., D. N. Baker, P. R. Higbie, and E. W. Hones Jr. (1978), High-Resolution Energetic Particle Measurements at 6.6 RE, 2, High-Energy Proton Drift Echoes, *J. Geophys. Res.*, 83(A10), 4857–4862.

Birn, J., M. F. Thomsen, J. E. Borovsky, G. D. Reeves, D. J. McComas, R. D. Belian, and M. Hesse (1997), Substorm ion injections: Geosynchronous observations and test particle orbits in three-dimensional dynamic MHD fields, *J. Geophys. Res.*, 102(A2), 2325–2341.

Birn, J., M. F. Thomsen, J. E. Borovsky, G. D. Reeves, D. J. McComas, R. D. Belian, and M. Hesse (1998), Substorm electron injections: Geosynchronous observations and test particle simulations, *J. Geophys. Res.*, 103(A5), 9235–9248.

Birn, J., J. Raeder, Y.L. Wang, R. A. Wolf, and M. Hesse (2004), On the propagation of bubbles in the geomagnetic tail, *Ann, Geophys.*, 22(5), 1773-1786.

Birn, J., M. Hesse, and K. Schindler (2006), Entropy conservation in simulations of magnetic reconnection, *Phys. Plasmas,* 13, 092117, doi:10.1063/1.2349440.

Birn, J., M. Hesse, K. Schindler, and S. Zaharia (2009), Role of entropy in magnetotail dynamics, *J. Geophys. Res., 114,* A00D03, doi:10.1029/2008JA014015.

Birn, J., R. Nakamura, E. V. Panov, and M. Hesse (2011), Bursty bulk flows and dipolarization in MHD simulations of magnetotail reconnection, *J. Geophys. Res.*, *116*, A01210, doi:10.1029/2010JA016083.

Buzulukova, N., M.-C. Fok, A. Pulkkinen, M. Kuznetsova, T.E. Moore, A. Glocer, P. C. Brandt, G. Toth, and L. Rastaetter (2010), Dynamics of ring current and electric fields in the inner magnetosphere during disturbed periods: CRCM--BATS-R-US coupled model, *J. Geophys. Res.*, doi:10.1029/2009JA014621.

Brackbill, J. U. and Barnes D. C., (1980), The Effect of Nonzero divB on the Numerical Solution of the Magnetohydrodynamic Equations, *J. Comput. Phys.*, 87:171–200.

Bret, A. and M. E. Dieckmann (2010), How large can the electron to proton mass ratio be in particle-in cell simulations of unstable system?, *Phys. Plasma*, 17, 032109, doi:10.1063/1.3357336.

Buchner, J. M. Scholer and C. T. Dum (2003), Hybrid simulation codes: Past, Present and Future – A turorial, *Lecture notes in Phys.*, Vol. 615/2003, 136-165.

Canuto, C., M. Y. Hussaini, A. Quarteroni, and T. A. Zang, Spectral Methods in Fluid Dynamics, Springer-Verlag, New York, 1988.

Cattell, C. (1996), Experimental evaluation of the Lundquist number for the Earth's magnetopause and magnetotail, *J. Geophys. Res.*, 101(A12), 27,309–27,316.

Cheng, C. Z. (2004), Physics of substorm growth phase, onset and dipolarization, *Space Sci. Rev.*, *113*, 207-2370.

Christon, S. P., D. G. Mitchell, D. J. Williams, L. A. Frank, C. Y. Huang, and T. E. Eastman (1988), Energy Spectra of Plasma Sheet Ions and Electrons From ~50 eV/e to ~1 MeV During Plasma Temperature Transitions, *J. Geophys. Res.*, 93(A4), 2562–2572.

De Zeeuw, D. L., S. Sazykin, R. A Wolf, T. I. Gombosi, A. J. Ridley, and G. Toth (2004), Coupling of a global MHD code and an inner magnetospheric model: Initial results, *J. Geophys. Res.*, 109, A12219, doi:10.1029/2003JA010366.

Evans, C. R., and J. F. Hawley (1988), Simulation of magnetohydrodynamic flows: A constrained transport method, *Astrophys. J.*, 332, 659.

Fok, M.-C., T. E. Moore, and D. C. Delcourt (1999), Modeling of inner plasma sheet and ring current during substorms, *J. Geophys. Res.*, 104, 14,557 -- 14,569.

Fok, M.-C., R. A. Wolf, R. W. Spiro, and T. E. Moore (2001), Comprehensive computational model of Earth's ring current, *J. Geophys. Res.*, 106(A5), 8417–8424.

Fok, M.-C., T. E. Moore, P. C. Brandt, D. C. Delcourt, S. P. Slinker, and J. A. Fedder (2006), Impulsive enhancements of oxygen ions during substorms, *J. Geophys. Res.*, 111, A10222, doi:10.1029/2006JA011839.

Fuchs, F. G., S. Mishra, N. H. Risebro (2009), Splitting based finite volume schemes for ideal MHD equations, *J. Comp. Phys.*, 228, 641-660.

Fuller-Rowell, T. J., D. Rees, S. Quegan, R. J. Moffett, M. V. Codrescu, and G. H. Millward (1996), A coupled thermosphere-ionosphere model (CTIM), in *STEP Handbook on Ionospheric Models*, Ed. R. W. Schunk, 217.

Gallagher, D. L., P. D. Craven, and R. H. Comfort (2000), Global core plasma model, *J.*

Geophys. Res., 105(A8), 18,819–18,833.

Garner, T. W. (2003), Numerical experiments on the inner magnetospheric electric field, *J. Geophys. Res.*, 108, 1373, doi:10.1029/2003JA010039.

Godunov, S. K (1959), Finite difference method for numerical computation of discontinuous solutions of the equations of fluid dynamics, *Matematicheskii Sbornik 47*, pp271-306.

Goldstein, J., J. L. Burch, and B. R. Sandel (2005), Magnetospheric model of subauroral polarization stream, *J. Geophys. Res.*, *110*, A09222, doi:10.1029/2005JA011135.

Gombosi, T. I., K. G. Powell, and B. van Leer (2000), Comment on "Modeling the magnetosphere for northward interplanetary magnetic field: Effects of electrical resistivity" by Joachim Raeder, *J. Geophys. Res.*, 105(A6), 13,141–13,147, doi:10.1029/1999JA000342.

Harel, M., R. Wolf, P. Reiff, R. Spiro, W. Burke, F. Rich, and M. Smiddy (1981), Quantitative Simulation of A Magnetospheric Substorm, 1. Model Logic and Overview, *J. Geophys. Res.*, 86(A4), 2217-2241.

Harten, A., A. Hyman, and P. D. Lax (1976), On finite difference approximations and entropy conditions for shocks, *Comm. Pure and Appl. Math.*, 29:297.

Harten, A., P. D. Lax and V. Leer (1983), On upstream differencing and Godnunov-type schemes for hyperbolic conservation laws, *SIAM Review* 25, 35-61.

Hesse, M., and J. Birn (1993), Three-Dimensional Magnetotail Equilibria by Numerical Relaxation Techniques, *J. Geophys. Res.*, 98(A3), 3973-3982.

Huang, C.-L., H. E. Spence, J. G. Lyon, F. R. Toffoletto, H. J. Singer, and S. Sazykin (2006), Storm-time configuration of the inner magnetosphere: Lyon-Fedder-Mobarry MHD code, Tsyganenko model, and GOES observations, *J. Geophys. Res.*, 111, A11S16, doi:10.1029/2006JA011626.

Hu, B., F. Toffoletto, R. Wolf, S. Sazykin, J. Raeder, D. Larson, and A. Vapirev (2010), Oneway coupled OpenGGCM/RCM simulation of the 23 March 2007 substorm event, *J.Geophys. Res.*, 115, doi:10.1029/2010JA015360.

Hu, B., R. A. Wolf, F. R. Toffoletto, J. Yang, and J. Raeder (2011), Consequences of violation of frozen ‑ in ‑ flux: Evidence from OpenGGCM simulations, *J. Geophys. Res.*, 116, A06223, doi:10.1029/2011JA016667.

Iijima, T., and T. Potemra (1976), The Amplitude Distribution of Field-Aligned Currents at Northern High Latitudes Observed by Triad, *J. Geophys. Res.*, 81(13), 2165-2174.

Jaggi, R., and R. Wolf (1973), Self-Consistent Calculation of the Motion of a Sheet of Ions in the Magnetosphere, *J. Geophys. Res.*, 78(16), 2852-2866.

Janhunen, P., K. E. J. Koskinen, and T. I. Pulkinen (1996), A new global ionosphere magnetosphere coupling simulation utilizing locally varying time step, in *International Conference on Substorms, ESA Special Publication*, vol. 389, edited by E. J. Rolfe & B. Kaldeich, pp. 205.

Jordanova, V., L. Kistler, C. Farrugia, and R. Torbert (2001), Effects of inner magnetospheric convection on ring current dynamics: March 10–12, 1998, *J. Geophys. Res.*, 106(A12), 29705-29720.

Keiling, A., et al. (2008a), Correlation of substorm injections, auroral modulations, and ground Pi2, *Geophys. Res. Lett.*, 35, L17S22, doi:10.1029/2008GL033969.

Keiling, A., et al. (2008b), Multiple intensifications inside the auroral bulge and their association with plasma sheet activities, *J. Geophys. Res.*, 113, A12216, doi:10.1029/2008JA013383.

Kivelson, M. G. (1995), Physics of space plasmas, *Introduction to Space Physics*, edited by M. G. Kivelson and C. T. Russell, Cambridge Univ. Press, 27-28.

Lee, L. C., L. Zhang, G. S. Choe, and H. J. Cai (1995), Formation of a very thin current sheet in the near-Earth magnetotail and the explosive growth phase of substorms, *Geophys. Res. Lett., 22(9),* 1137-1140.

Lemon C., F. Toffoletto, M. Hesse, J. Birn (2003), Computing magnetospheric force equilibria, *J. Geophys. Res.*, 108 (A6), 1237, doi:10.1029/2002JA009702.

Lemon, C., R. A. Wolf, T. W. Hill, S. Sazykin, R. W. Spiro, F. R. Toffoletto, J. Birn, and M. Hesse (2004), Magnetic storm ring current injection modeled with the Rice Convection Model and a self-consistent magnetic field. *Geophys. Res. Lett.,* 31, L21801, doi:10.1029/2004GL020914.

LeVeque (2002), ***Finite volume methods for hyperbolic problems***, Cambridge University

Press.

Liemohn, M. W., J. U. Kozyra, V. K. Jordanova, G. V. Khazanov, M. F. Thomsen, and T. E. Cayton (1999), Analysis of early phase ring current recovery mechanisms during geomagnetic storms, *Geophys. Res. Lett.*, 26(18), 2845-2848.

Liu, W. L., X. Li, T. Sarris, C. Cully, R. Ergun, V. Angelopoulos, D. Larson, A. Keiling, K. H. Glassmeier, and H. U Auster (2009), Observation and modeling of the injection observed by THEMIS and LANL satellites during the 23 March 2007 substorm event, *J. Geophys. Res.,* 114, A00C18, doi:10.1029/2008JA013498.

Li, X, D. N. Baker, M. Temerin, G. D. Reeves, and R. D. Belian (1998), Simulation of dispersionless injections and drift echoes of energetic electrons associated with substorms, *Geophys. Res. Lett.,* 25(20), 3763-3766.

Li, X., T.E. Sarris, D. N. Baker, W. K. Peterson, and H. J. Singer (2003), Simulation of energetic particle injections associated with a substorm on August 27, 2001, *Geophys. Res. Lett.*, 30(1), 1004, doi:10.1029/2002GL015967.

Lui, A. T. Y., R. E. Lopez, B. J. Anderson, K. Takahashi, L. J. Zanetti, R. W. McEntire, T. A. Potemra, D. M. Klumpar, E. M. Greene, and R. Strangeway (1992), Current disruptions in the near-Earth neutral sheet region, *J. Geophys. Res.*, *97*(A2), 1461–1480, doi:10.1029/91JA02401.

Lui, A. T. Y (2004), Potential plasma instabilities for substorm expansion onsets, *Space Sci. Rev.*, *113*, 127-206.

Lyons, L. R., C.-P. Wang, T. Nagai, T. Mukai, Y. Saito, and J. C. Samson (2003), Substorm inner plasma sheet particle reduction, *J. Geophys. Res.*, 108(A12), 1426, doi:10.1029/2003JA010177.

Lyon, J. G. (2000), The solar wind-magnetosphere-ionosphere system, Science, Vol. 288, no. 5473 pp. 1987-1991,doi: 10.1126/science.288.5473.1987.

Lyon, J. G., J. A. Fedder, and C. M. Mobarry (2004) J.G. Lyon, J.A. Fedder and C.M. Mobarry, The Lyon-Fedder-Mobarry (LFM) global MHD magnetospheric simulation code, *J. Atmos. Terr. Physics*, 66 (15-16) (2004), pp. 1333-1350.

Mauk, B. H., and C. -I. Meng (1987), Plasma Injection During Substorms, *Physics Scripta., Vol. T18.* 128-139.

Moore, T. E., M. - C. Fok, D. C. Delcourt, S. P. Slinker, and J. A. Fedder (2008), Plasma plume circulation and impact in an MHD substorm, *J. Geophys. Res.*, 113, A06219, doi:10.1029/2008JA013050.

Pembroke, A., F. R. Toffoletto, S. Sazykin, M. Wiltberger, J. Lyon, V. Merkin, P. Schmitt (2011), Initial results from a dynamic coupled magnetosphere-ionosphere-ring current model, under review *J. Geophys. Res.*

Pierrard, V., J. Goldstein, N. André, V. K. Jordanova, G. A. Kotova, J. F. Lemaire, M. W. Liemohn, and H. Matsui (2009), Recent Progress in Physics-Based Models of the Plasmasphere, *Space Sci. Rev.*, 145: 193–229.

Pontius, D. H., Jr., and R. A. Wolf (1990), Transient flux tubes in the terrestrial magnetosphere, *Geophys. Res. Lett.,* 17, 49-52.

Parker, E. N. (1958), Dynamics of the Interplanetary Gas and Magnetic Fields, *The Astrophysical Journal,* Vol. 128, 664.

Powell, K. G., P. L. Roe, T. J. Linde, T. I. Gombosi, and D. L. De Zeeuw (1999), A solution-adaptive upwind scheme for ideal magnetohydrodynamics, *J. Comput. Phys.,* 154, 284-309.

Pritchett, P. L. (2007), Onset of magnetic reconnection, in *Reconnection of Magnetic Fields*, edited by J. Birn and E. Priest, pp. 121–132, Cambridge Univ. Press., Cambridge, U. K., 113(1), 207-270, doi: 10.1023/B:SPAC.0000042943.59976.0e.

Raeder, J., J. Berchem, and M. Ashour-Abdalla, (1998) The Geospace Environment Modeling Grand Challenge: Results from a Global Geospace Circulation Model, *J. Geophys. Res.*, 103(A7), 14787-14797.

Raeder, J. (1999), Modeling the magnetosphere for northward interplanetary magnetic field: Effects of electrical resistivity, *J. Geophys. Res.*, 104(A8), 17,357–17,367, doi:10.1029/1999JA900159.

Raeder, J. (2000), Reply, *J. Geophys. Res.*, 105(A6), 13,149-13,153.

Raeder, J., R. L. McPherron, L. A. Frank, S. Kokubun, G. Lu, T. Mukai, W. R. Paterson, J. B. Sigwarth, H. J. Singer, and J. A. Slavin (2001), Global simulation of the Geospace Environment Modeling substorm challenge event, *J. Geophys. Res.*, 106, 381.

Raeder, J. (2003)., *Global Magnetohydrodynamics — A Tutorial*, in: Space Plasma Simulation, J. Buechner, C. T. Dum and M. Scholer, eds., Lecture Notes in Physics, vol. 615, Springer Verlag, Heidelberg, ISBN 3-540-00698-2.

Raeder, J., J. Dorelli, D. Larson, and B. Loring (2006), Physical, Numerical, and Computational Challenges in Modeling the Geospace Environment, *ASP Conference Series*, vol. 359, 202.

Raeder, J., D. Larson, W. Li, E. L. Kepko, and T. Fuller-Rowell (2008), OpenGGCM Simulations for the THEMIS Mission, *Space Science Reviews,* doi: 10.1007/s11214-0421-5.

Raeder, J., P. Zhu, Y. Ge, and G. Siscoe (2010), Open Geospace General Circulation Model simulation of a substorm: Axial tail instability and ballooning mode preceding substorm onset, *J. Geophys. Res.*, *115*, A00I16, doi:10.1029/2010JA015876.

Roe, P. L (1981), Approximate Riemann solvers, parameter vectors and difference schemes, *J. Comp. Phys.*, 43, 357-372.

Roe, P. L. and D. S. Balsara (1996), Notes on the eigensystem of magnetohydrodynamics, *SIAM. J. Appl. Math*, 57-67.

Sazykin, S (2000), *Theoretical studies of penetration of magnetospheric electric fields to the ionosphere*, PhD Dissertation, University of Utah.

Sergeev, V.A. and W. Lennartsson (1988), Plasma sheet at X $\cong -20$ RE during steady magnetospheric convection, *Planet. Space Sci. 36*, p. 353.

Sergeev, V.A., R. J. Pellinen, and T. I. Pulkkinen (1996a), Steady magnetospheric convection: A review of recent results, *Space Sci. Rev.*, 75, 551-604, doi: 10.1007/BF00833344.

Sergeev, V. A, V. Angelopoulos, J. Gosling, C. Cattell, and C. Russell (1996b), Detection of localized, plasma-depleted flux tubes or bubbles in the midtail plasma sheet, *J. Geophys. Res.,* 101, 10817-10826.

Shu, C-W. (1998), Essentially Non-Oscillatory and Weighted Essentially Non-Oscillatory Schemes for hyperbolic conservation Laws, *NASA ICASE report*, No. 97-65.

Siscoe, G. L., M. M. Kuznetsova, and J. Raeder (2009), Search for an onset mechanism that operates for both CMEs and substorms, *Ann. Geophys., 27(8)*, 3141-3146.

Sitnov, M. I., P. N. Guzdar, and M. Swisdak (2007), Atypical current sheets and plasma bubbles: A self-consistent kinetic model, *Geophys. Res. Lett.*, 34, L15101, doi:10.1029/2007GL029693.

Sitnov, M. I., N. A. Tsyganenko, A. Y. Ukhorskiy, B. J. Anderson, H. Korth, A. T. Y. Lui, and P. C. Brandt (2010), Empirical modeling of a CIR-driven magnetic storm, *J. Geophys. Res.*, doi:10.1029/2009JA015169

Sitnov, M. I. and K. Schindler (2010), Tearing stability of a multiscale magnetotail current sheet, *Geophys. Res. Lett., 37*, L08102, doi:10.1029/2010GL042961.

Smit, J., M. van Sint Annaland, J. A. M. Kuipers (2005), Grid adaptation with WENO schemes for non-uniform grids to solve convection-dominated partial differential equations, *Chem. Eng. Sci.*, 60, 2609-2619.

Southwood, D. J., and R. A. Wolf (1978), An Assessment of the Role of Precipitation in Magnetospheric Convection, *J. Geophys. Res.*, *83*(A11), 5227–5232.

Spiro, R. W., R. A. Heelis, and W. B. Hanson (1979), Rapid subauroral ion drifts observed by Atmosphere Explorer C, *Geophys. Res. Lett.*, 6(8), 657-660.

Spiro, R. W., Wolf, R. A., and B. G. Fejer (1988), 'Penetration of High-latitude-electric-field Effects to Low Latitudes During SUNDIAL 1984', *Ann. Geophys*. 6, 39–50.

Spence, H. E., and M. G. Kivelson (1993), Contributions of the Low-Latitude Boundary Layer to the Finite Width Magnetotail Convection Model, *J. Geophys. Res.*, 98(A9), 15,487–15,496.

Taktakishvili, A., M. Kuznetosova, M. Hesse, L. Rastatter, A. Chulaki, and A. Pulkkinnen (2007), Metrics analysis of the coupled Block Adaptive-Tree Solar Wind Roe-Type Upwind Scheme and Fork ring current model performance, *Space Weather*, 5, S11004.

Toffoletto, F. R., J. Birn, M. Hesse, R.W. Spiro, and R.A. Wolf (2001), Modeling inner magnetospheric electrodynamics, in *Proceedings of the Chapman Conference on Space Weather*, edited by P. Song, G.L. Siscoe, and H.J. Singer, Am. Geophys. Un., Washington, D. C., pp. 265-272.

Toffoletto, F. R., S. Sazykin, R. W. Sprio, and R. A. Wolf (2003), Inner magnetospheric modeling with the Rice Convection Model, *Space Sci. Rev., 107*, 175.

Toffoletto, F., S. Sazykin, R. W. Spiro, R. A. Wolf, J. G. Lyon (2004), RCM meets LFM: initial results of on-way coupling, *J. Atmos. Terr. Physics*, 66, 1361-1370.

Thomsen, M. F., J. Birn, J. E. Borovsky, K. Morzinski, D. J. McComas, and G. D. Reeves (2001), Two-satellite observations of substorm injections at geosynchronous orbit, *J. Geophys. Res.*, 106(A5), 8405–8416.

Toro, E. F., M. Spruce and W. Speares (1994), Restoration of the contact surface in the HLL-Riemann solver, *Shock Waves*, 4, 25-34.

Tóth, G., et al. (2005), Space Weather Modeling Framework: A new tool for the space science community, *J. Geophys. Res.,* 110, A12226, doi:10.1029/2005JA011126.

Tóth, G., D. L. De Zeeuw, T. I. Gombosi, W. B. Manchester, A. J. Ridley, I. V. Sokolov, and I. I. Roussev (2007), Sun-to-thermosphere simulation of the 28 - 30 October 2003 storm with the Space Weather Modeling Framework, *Space Weather*, 5, S06003, doi:10.1029/2006SW000272.

Tsyganenko, N.A. and D.P. Stern (1996), Modeling the global magnetic field of the large-scale Birkeland current systems, *J.Geophys.Res.*, v.101, 27187-27198.

Umeda, T. (2011), Simulation of collisionless plasma with the Vlasov method, In: *Computer Physics*, edited by B. S. Doherty and A. N. Molloy, Nova Science-New

York.

Vasyliunas, V. M. (1970), 'Mathematical Models of Magnetospheric Convection and its Coupling to the Ionosphere', in B. m. McCormac (ed.), *Particles and Fields in the Magnetosphere*, D. Reidel, Hingham, MA, Hingham, MA, pp. 60–71.

Vasyliunas, V. M. (1975), Theoretical models of magnetic field line merging, *Rev. Geophys.*, *13(1)*, 303-336.

Voigt, G.-H., and R. A. Wolf (1988), Quasi-static magnetospheric MHD processes and the ''ground state'' of the magnetosphere, *Rev. Geophys.*, 26, 823.

Walsh, A. P., A. N. Fazakerley, A. D. Lahiff, M. Volwerk, A. Grocott, M. W. Dunlop, A. T. Y. Lui, L. M. Kistler, M. Lester, C. Mouikis, Z. Pu, C. Shen, J. Shi, M. G. G. T. Taylor, E. Lucek, T. L. Zhang, and I. Dandouras (2009) Cluster and Double Star multipoint observations of a plasma bubble, *Ann. Geophys.*, 27, 725-743.

Wild, J. A., E. E. Woodfield and S. K. Morley (2009), On the triggering of auroral substorms by northward turnings of the interplanetary magnetic field, *Ann. Geophys.*, 27, 3559-3570.

Wolf, R. A. (1970), Effects of Ionospheric Conductivity on Convective Flow of Plasma in the Magnetosphere, *J. Geophys. Res.*, 75(25), 4677-4698.

Wolf, R. A. (1983), The Quasi-static (Slow-flow) Region of the Magnetosphere', in R. L. Car*ovillano* and J. M. Forbes (eds.), *Solar Terrestrial Physics*, Series, D. Reidel, Hingham, MA, pp. 303-368.

Wolf, R. A., Y. Wan, X. Xing, J.-C. Zhang, and S. Sazykin (2009), Entropy and plasma sheet transport, *J. Geophys. Res.*, 114, A00D05, doi:10.1029/2009JA014044.

Wu, L., F. Toffoletto, R. A. Wolf, and C. Lemon (2009), Computing magnetospheric equilibria with anisotropic pressures, *J. Geophys. Res.*, 114, A05213, doi:10.1029/2008JA013556.

Yang, J., F. R. Toffoletto, R. A. Wolf, S. Sazykin, R. W. Spiro, P. C. Brandt, M. G. Henderson, and H. U. Frey (2008), Rice convection Model simulation of the 18 April 2002 sawtooth event and evidence for interchange instability, *J. Geophys. Res.*, 113, A11214.

Yang, J. (2010), *Inner magnetospheric modeling during geomagnetic active times*, PhD Dissertation, Rice Univerisity.

Yang, J., R. A. Wolf, and F. R. Toffoletto (2011), Accelerated thinning of the near-Earth plasma sheet caused by a bubble-blob pair, *Geophys. Res. Lett.*, *38*, L01107, doi:10.1029/2010GL045993.

Yee, K. (1996), Numerical solution of initial boundary value problems involving maxwell's equations in isotropic media, *Antennas and Propagation, IEEE Transactions*, 14 (3), 302-307, doi:10.1109/TAP.1966.1138693.

Zaharia, S., C. Z. Cheng, and J. R. Johnson (2000), Particle transport and energization associated with substorms, *J. Geophys. Res.*, 105(A8), 18,741–18,752.

Zaharia, S., J. Birn, R. H. W. Friedel, G. D. Reeves, M. F. Thomsen, and C. Z. Cheng

(2004), Substorm injection modeling with nondipolar, time-dependent background field, *J. Geophys. Res.,* 109, A10211.

Zaharia, S., J. Birn, and C. Z. Cheng (2005), Toward a global magnetospheric equilibrium model, *J. Geophys. Res.*, 110, A09228, doi:10.1029/2005JA011101.

Zhang, J., et al. (2007), Understanding storm-time ring current development through data-model comparisons of a moderate storm, *J. Geophys. Res.*, *112*, A04208, doi:10.1029/2006JA011846.

Zhang, J.-C., R. A. Wolf, S. Sazykin, and F. R. Toffoletto (2008), Injection of a bubble into the inner magnetosphere, *Geophys. Res. Lett.,* 35, L02110, doi:10.1029/2007GL032048.

Zhang, J.-C., R. A. Wolf, G. M. Erickson, R. W. Spiro, F. R. Toffoletto, and J. Yang (2009), Rice Convection Model simulation of the injection of an observed bubble into the inner magnetosphere: 1. Magnetic-field and other inputs, *J. Geophys. Res.*, A08218, doi:10.1029/2009JA014130.

Zheng, L. (2011), *A method to compute three dimensional magnetospheric equilibria with dipole tilt and its application to estimating magnetic flux tube volume*, MS Dissertation, Rice University.

Zwan, B. J., and R. A. Wolf (1976), Depletion of Solar Wind Plasma Near a Planetary Boundary, *J. Geophys. Res.*, 81(10), 1636–1648, doi:10.1029/JA081i010p01636.

Zhu, P., J. Raeder, K. Germaschewski, and C. C. Hegna (2009), Initiation of ballooning instability in the near-Earth plasma sheet prior to the 23 March 2007 THEMIS substorm expansion onset, *Ann. Geophys.,* 27, 1129 - 1138.